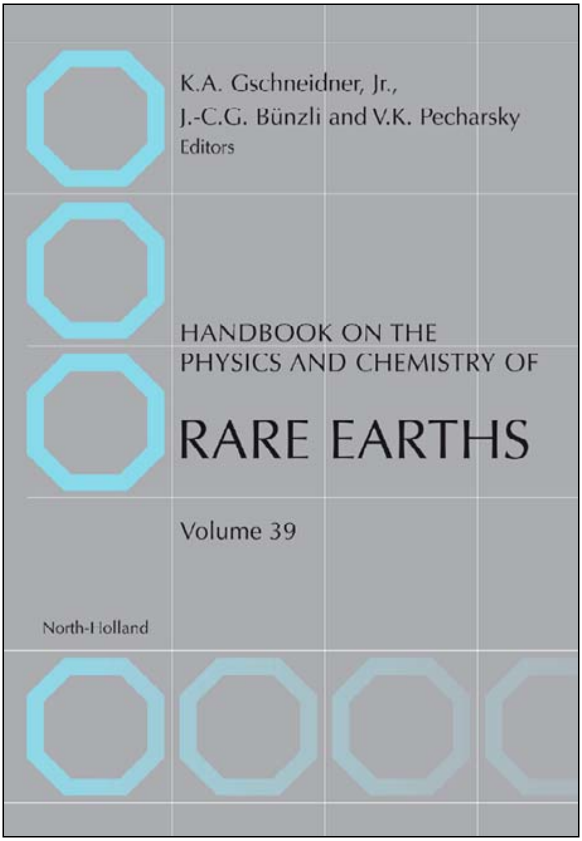

From: W.M. Temmerman, L. Petit, A. Svane, Z. Szotek, M. Lüders, P. Strange,
J.B. Staunton, I.D. Hughes, and B.L. Gyorffy, The Dual, Localized or Band-Like,
Character of the 4f-States. In K.A. Gschneidner, Jr., J.-C.G. Bünzli and
V.K. Pecharsky, editors: Handbook on the Physics and Chemistry of Rare Earths,
Vol. 39, Netherlands: North-Holland, 2009, pp. 1-112.
ISBN: 978-0-444-53221-3

North-Holland

CHAPTER 241

The Dual, Localized or Band-Like, Character of the 4f-States

W.M. Temmerman*, **L. Petit**[†], **A. Svane**[†], **Z. Szotek***, **M. Lüders***, **P. Strange**[‡], **J.B. Staunton**[§], **I.D. Hughes**[§], and **B.L. Gyorffy**[¶]

Contents

* Daresbury Laboratory, Daresbury, Warrington WA4 4AD, United Kingdom
[†] Department of Physics and Astronomy, University of Aarhus, DK-8000 Aarhus C, Denmark
[‡] School of Physical Sciences, University of Kent, Canterbury, Kent, CT2 7NH, United Kingdom
[§] Department of Physics, University of Warwick, Gibbet Hill Road, Coventry, CV4 7AL, United Kingdom
[¶] H.H. Wills Physics Laboratory, University of Bristol, Bristol BS8 1TL, United Kingdom

---

Handbook on the Physics and Chemistry of Rare Earths, Volume 39
ISSN 0168-1273, DOI: 10.1016/S0168-1273(08)00001-9

List of Symbols and Acronyms

a	lattice parameter
a_0	Bohr radius
$A_{n\mathbf{k}}(\omega)$, $A_\mathrm{B}(\mathbf{k}, E)$	Bloch spectral function, n is band index and $\mathbf{k}$ is the wave vector
$\mathbf{B}$	magnetic field
e	electron charge
E	(total) energy
g_J	Landé g-factor
$f_{\mathbf{q}\lambda,\mathbf{q}'\lambda'}(\omega)$	scattering amplitude
F^l	Slater integrals
G	Green's function
GW	approximation for the self-energy based on the product of the Green's function (G) and the screened Coulomb interaction (W)
$\hbar$	Planck's constant
k_B	Boltzmann constant
$\hat{L}$	angular momentum operator
l	angular momentum quantum number
m	electron mass
n, $n(\mathbf{r})$	electron density
p	pressure
R	rare earth
$\hat{S}$	spin operator
S	Wigner Seitz (atomic sphere) radius
S_x	entropy, where x denotes the specific entropy contribution
$S^{(2)}$	direct correlation function of local moments
T	temperature
U	(Hubbard U), on-site Coulomb interaction
$U[n]$	Hartree (classical electrostatic) energy functional

V	volume
$V(\mathbf{r})$	potential
xc	exchange and correlation
Z	atomic number
β	inverse temperature $1/(k_B T)$
$\chi(\mathbf{q})$	magnetic susceptibility
μ_B	Bohr magneton
λ	Spin-orbit coupling parameter
Ω	(generalised) grand potential
$\Psi(\mathbf{r}_1, \mathbf{r}_2, \ldots)$	electronic many body wave function
$\Psi(\mathbf{r})$	Electronic single particle wave function
Σ	self-energy
ω	frequency
ASA	atomic sphere approximation
BSF	Bloch spectral function
BZ	Brillouin zone
CPA	coherent potential approximation
DCA	dynamical cluster approximation
dhcp	double hexagonal closed packed
DFT	density functional theory
DLM	disordered local moment
DMFT	dynamical mean-field theory
DOS	density of states
ESRF	European Synchrotron Radiation Facility
fcc	face centered cubic
GGA	generalized gradient approximation
hcp	hexagonal closed packed
KKR	Korringa, Kohn, and Rostoker
LDA	local density approximation
LMTO	linear muffin-tin orbitals
LSDA	local spin density approximation
LS	spin-orbit
LSD	local spin density
LSIC	local self-interaction correction
MXRS	magnetic X-Ray Scattering
OP	orbital polarization
PAW	Projector augmented wave
RKKY	Ruderman-Kittel-Kasuya-Yoshida
SCF	self-consistent field
SI	self-interaction
SIC	self-interaction correction
SIC-LSD	self-interaction-corrected local spin density
SIC-LSDA	self-interaction-corrected local spin density approximation
WS	Wigner Seitz
XMaS	X-ray magnetic scattering

1. INTRODUCTION

Ab initio calculations for lanthanide solids were performed from the early days of band theory (Dimmock and Freeman, 1964). These pioneering calculations established that physical properties of the lanthanides could be described with the f-states being inert and treated as core states. For example, the crystal structures of the early lanthanides could be determined without consideration of the 4f-states (Duthie and Pettifor, 1977). Also the magnetic structures of the late lanthanides could be evaluated that way (Nordström and Mavromaras, 2000). Of course, one needed to postulate the number of s, p, and d valence electrons that is three in the case of a trivalent lanthanide solid or two in the case of a divalent lanthanide solid. Even this valence could be calculated in a semi-phenomenological way without taking the 4f-electrons explicitly into account (Delin et al., 1997).

However, in some lanthanides, in particular the Ce compounds, and CeB_6 (Langford et al., 1990) is an example, the 4f-level could either be part of the valence states or be inert and form part of the core. Fermiology measurements could determine how many electrons participated in the Fermi surface and hence could deduce the nature of the 4f-state as either part of the core or part of the valence states. These measurements were complemented by band structure calculations of the type '4f-core' or '4f-band', respectively treating the 4f-states as part of the core or as valence states.

Treating the 4f-electrons in Gd as valence states, in the '4f-band' approach, allowed for an accurate description of the Fermi surface (Temmerman and Sterne, 1990) but failed in obtaining the correct magnetic structure (Heinemann and Temmerman, 1994). What these and numerous other calculations demonstrated was that some properties of the lanthanides could be explained by a '4f-band' framework and some by a '4f-core' framework. This obviously implied a dual character of the 4f electron in lanthanides: some of the 4f-electrons are inert and are part of the core, some of the 4f-electrons are part of the valence and contribute to the Fermi surface.

The correct treatment of the 4f electrons in lanthanides is a great challenge of any modern theory. On the one hand, when considering the spatial extent of their atomic orbitals, the 4f electrons are confined to the region close to the nuclei, that is, they are very core-like. On the other hand, with respect to their position in energy, which is often in the vicinity of the Fermi level, they should rather be classified as valence electrons. Some of the most widely used theoretical methods for the description of lanthanide systems are based on DFT (Hohenberg and Kohn, 1964). Its basic concept is the energy functional of the total charge density of the electrons in the solid that, when minimized for given nuclear positions, provides the energy as well as the charge density of the ground state. However, for solids, the exact DFT energy functional is not known, and one is forced to use approximations, of which the most successful is the LSDA, where electron correlations are treated at the level of the homogeneous electron gas, and the f electrons are described by extended Bloch states, as all the other, s, p, and d, electrons are. But even in this approach, one can try to differentiate between the f and other electrons, by including them into the core ('f-core' approach). One step beyond the local approximation, there are various flavours of the so-called GGAs, which, in addition to the dependence on a homogeneous charge distribution, include also some gradient corrections. Unfortunately, neither LDA nor GGA have proved very successful for systems where f electrons have a truly localized nature. Here, the SIC-LSD approaches have shown to be most useful, in particular as far as the cohesive properties are concerned.

The SIC-LSDA (Perdew and Zunger, 1981) provides an *ab initio* computational scheme that allows the differentiation between band-like and core-like f-electron (Temmerman et al., 1998). This is a consequence of the SIC being only substantial for localized states, which the 4f-states are. From this, one would expect to apply the SIC to all 4f-states since the delocalized s, p, and d electrons are not experiencing any self-interaction. But we do not know how many localized 4f-states there are. For a divalent lanthanide, there is one more localized 4f electron than for a trivalent lanthanide. To determine how many localized 4f electrons there are in a particular 4f-solid, we can be guided by minimizing the SIC-LSD total energy over all possible configurations of localized (SIC) and itinerant 4f-states. This chapter elaborates on the consequences of this, naturally leading to the dual character of the 4f electron: either localized after applying the SIC or LSD band-like and contributing to the Fermi surface. The SIC-LSD method forms the basis of most of the work reviewed in this chapter, and its focus will be on the total energy aspect and, as we will show, provides a quite accurate description of the cohesive properties throughout the lanthanide series.

Other known methods that have been used in the study of lanthanides include the OP scheme, the LDA + U approach, where U is the on-site Hubbard repulsion, and the DMFT, being the most recent and also the most advanced development. In particular, when combined with LDA + U, the so-called LDA + DMFT scheme, it has been rather successful for many complex systems. We note here that both DMFT and LDA + U focus mostly on spectroscopies and excited states (quasi-particles), expressed via the spectral DOS. In a recent review article (Held, 2007), the application of the LDA + DMFT to volume collapse in Ce was discussed. Finally, the GW approximation and method, based on an electron self-energy obtained by calculating the lowest order diagram in the dynamically screened Coulomb interaction, aims mainly at an improved description of excitations, and its most successful applications have been for weakly correlated systems. However, recently, there have been applications of the quasi-particle self-consistent GW method to localized 4f systems (Chantis et al., 2007).

The outline of the present chapter is as follows. Section 2 deals with the relevant physical, electronic, and magnetic properties of the lanthanides. Section 3 reviews briefly the above-mentioned theoretical methods, with the focus on the SIC-LSDA method, and, in particular, the full implementation of SIC, involving repeated transformations between Bloch and Wannier representations (Temmerman et al., 1998). This is then compared with the local-SIC, implemented in the multiple scattering theory (Lüders et al., 2005). Section 4 deals with the valence (Strange et al., 1999) and valence transitions of the lanthanides. Section 5 discusses the local magnetic moments of the lanthanides. Section 6 discusses two spectroscopies applied to lanthanides and some of their compounds. Section 7 outlines a methodology of calculating the finite temperature (T) properties of the lanthanides and their compounds, and illustrates it on the study of finite T magnetism of the heavy lanthanides and the finite T diagram of the Ce α–γ phase transition. The *ab initio* theory of the finite T magnetism is based on the calculations of the paramagnetic susceptibility within the DLM picture (Gyorffy et al., 1985). This combined DLM and SIC approach (Hughes et al., 2007) for localized states provides an *ab initio* description of the magnetic properties of ionic systems, without the need of mapping onto the Heisenberg Hamiltonian. Finally, Section 8 addresses some remaining issues such as how to include dynamical fluctuations, and Section 9 concludes this chapter.

2. SALIENT PHYSICAL PROPERTIES

The physical properties of the lanthanides are rather unique among all metals. This is the consequence of the interaction of delocalized conduction electrons with the localized f-states. The physical properties are characterized by the continuously decreasing lattice parameter upon traversing the lanthanide series, the so-called lanthanide contraction. Their physical properties can be described very efficiently, and also catalogued, by the valence of the lanthanide. Most of the lanthanides and their compounds are trivalent, but towards the middle and the end of the lanthanide series, divalence (Sm, Eu, Tm, Yb) can occur. At the very beginning of the lanthanide series, in Ce and Pr and their compounds, also tetravalence is sometimes observed. For tetravalent Ce and Pr and their compounds, strong quasi-particle renormalization occurs and some Ce compounds exhibit heavy fermion behaviour. For lanthanides with higher atomic number than Pr, trivalence establishes itself, however, switching to divalence in Eu and some of the Sm and Eu compounds. For Gd, the f-shell is half-filled and the valence starts again, as in the beginning of the lanthanide series, as strongly trivalent and gradually reducing to divalence as seen in Yb and Tm compounds. Fingerprints of the valencies can be seen in the value of the spin and orbital magnetic moments and of the lattice parameter: divalent lattice parameters can be 10% larger than trivalent ones. Also the nature of the multiplet structure tells us about the valence, as do Fermiology measurements, by providing information on the number of f-states contributing to the Fermi surface. Finally, MXRS has the potential to determine the valence as well as to provide information on the symmetry of the localized states (Arola et al., 2004).

2.1 Lattice parameters

The experimental lattice parameters as a function of lanthanide atomic number show the famous lanthanide contraction, the decrease of the lattice parameter across the lanthanide series, with the exception of the two anomalies for Eu and Yb, as seen in Figure 1 (top panel). What is plotted there is actually the atomic sphere radius S (in atomic units) as a function of the lanthanide element. A similar behaviour is also observed, for example, for lanthanide monochalcogenides and monopnictides, whose lattice parameters are also shown in Figure 1 (middle and bottom panels).

This lanthanide contraction is associated with the filling of the 4f shell across the lanthanide series. The effect is mainly due to an incomplete shielding of the nuclear charge by the 4f electrons and yields a contraction of the radii of outer electron shells.

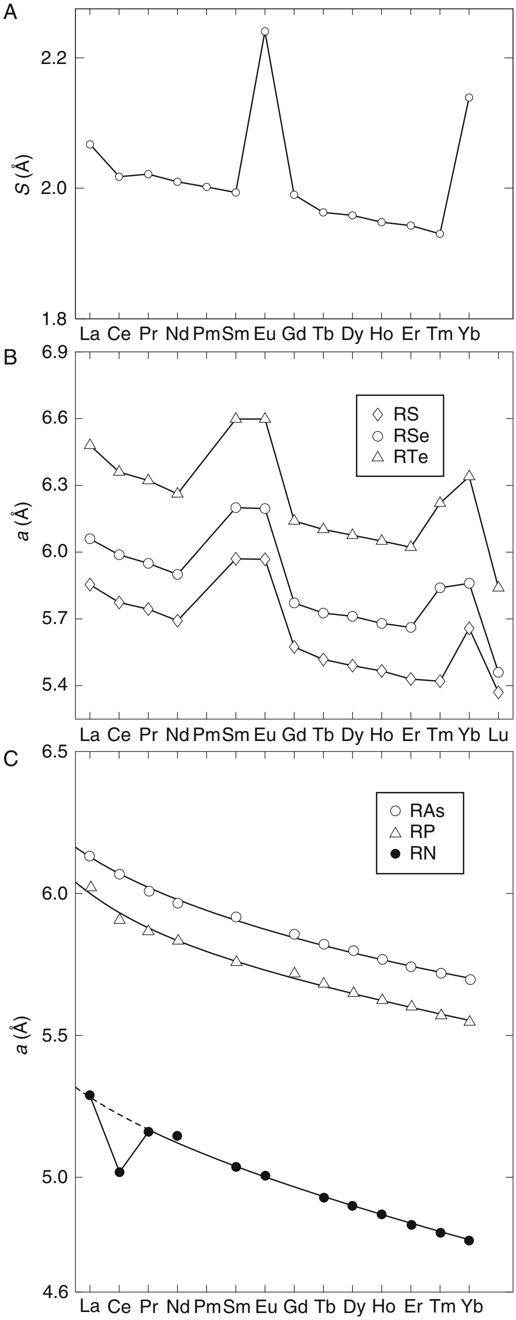

FIGURE 1 Lattice constants of the elemental lanthanides (top), their chalcogenides (middle) (after Jayaraman, 1979), and pnictides (bottom). For the elemental lanthanides, it is the atomic sphere radius, *S*, that is shown instead of the lattice parameter, where *S* is defined as $V = 4/3\pi S^3$ with *V* the unit cell volume.

The jumps in the lattice constants in Figure 1, seen for the elemental Eu and Yb, as well as at the chalcogenides of Sm, Eu, Tm, and Yb, are due to the change in valence from trivalent to divalent. If a transition to the trivalent state were to occur, the lattice constant would also follow the monotonous behaviour of the other lanthanides, as seen in Figure 2, where the ionic radii of trivalent lanthanide ions are displayed. For the pnictides, only CeN shows an anomaly, indicating a tetravalent state, whereas all the other compounds show a smooth, decreasing behaviour as a function of the lanthanide atomic number.

Pressure studies have been able to unravel a lot of the physics of the rare earths. Not only have pressure experiments seen changes of valence from divalent to trivalent, but also changes in the structural properties. In the case of Ce and Ce compounds, the valence changes under pressure from trivalent to tetravalent or from one localized f-state to a delocalized state have been observed. This will be discussed in greater detail in Section 4 of this chapter.

2.2 Magnetic properties and magnetic order

The lanthanides are characterized by local magnetic moments coming from their highly localized 4f electron states. These moments polarize the conduction electrons which then mediate the long range magnetic interaction among them. The RKKY interaction is the simplest example of this mechanism. These long range magnetic interactions in lanthanide solids lead to the formation of a wide variety of magnetic structures, the periodicities of which are often incommensurate with the underlying crystal lattice. These are helical structures that have been studied in detail with neutron scattering (Sinha, 1978; Jensen and Mackintosh, 1991). In the later sections of this chapter, we shall elaborate on our *ab initio* study of the finite temperature magnetism of the heavy lanthanides and elucidate the role of the conduction electrons in establishing the complex helical structures in these systems. This *ab initio* theory and calculations go beyond the 'standard model' of lanthanide magnetism (Jensen and Mackintosh, 1991).

The standard approach to describing the magnetism of lanthanides, and in particular their magnetic moments, is to assume the picture of electrons in an

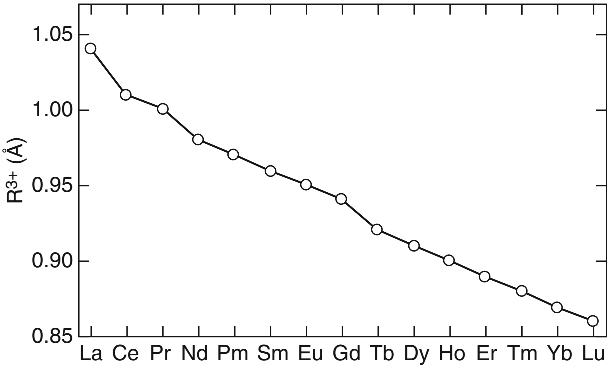

FIGURE 2 Ionic radii of trivalent lanthanides.

isolated atom. In the absence of spin-orbit coupling, the angular momenta of the electrons in an atom combine according to Russel-Saunders coupling to give a total orbital angular momentum $\hat{L}$ and a total spin angular momentum $\hat{S}$, with the respective eigenvalues of $L(L+1)\hbar^2$ and $S(S+1)\hbar^2$ (Gasiorowicz, 1974). In the lanthanides, however, spin-orbit coupling $\lambda\ \hat{L} \cdot \hat{S}$ cannot be ignored (Strange, 1998) and therefore one has to introduce the total angular momentum $\hat{J} = \hat{L} + \hat{S}$. The wavefunctions describing the electrons then obey the eigenvalue relations:

$$\begin{aligned}\hat{J}^2\psi_{J,m_j,L,S} &= J(J+1)\hbar^2\psi_{J,m_j,L,S}\\ \hat{J}_z\psi_{J,m_j,L,S} &= m_j\hbar\psi_{J,m_j,L,S}\\ \hat{L}^2\psi_{J,m_j,L,S} &= L(L+1)\hbar^2\psi_{J,m_j,L,S}\\ \hat{S}^2\psi_{J,m_j,L,S} &= S(S+1)\hbar^2\psi_{J,m_j,L,S},\end{aligned} \tag{1}$$

where $\psi_{J,m_j,L,S}$ are normalized atomic wavefunctions, which are assumed to be located on a single atom nucleus.

The energy associated with a magnetic field in the lanthanide is small in comparison to electronic energies and it is usual to treat it applying perturbation theory. The perturbing potential is simply the scalar product of the magnetic moment, $\hat{\mu}$, and the magnetic field, **B**, experienced by the atom:

$$\delta V = -\hat{\mu}\cdot\mathrm{B}, \tag{2}$$

where $\hat{\mu}$ is given as

$$\hat{\mu} = -\mu_{\mathrm{B}} g_J \hat{J}. \tag{3}$$

Here, g_J is the Landé g-factor:

$$g_J = 1 + \frac{J(J+1) - L(L+1) + S(S+1)}{2J(J+1)}. \tag{4}$$

If this model is correct, then it is only necessary to know the values of the quantum numbers J, L, and S to calculate the magnetic moment of the lanthanides. These are determined by Hund's rules:

(1) S will be a maximum subject to the Pauli exclusion principle
(2) L will be a maximum subject to rule 1 and to the Pauli exclusion principle
(3) If the shell is less than half-full, then the spin-orbit coupling coefficient λ is positive and $J = |L-S|$ is the ground state. For a shell that is greater than or equal to half-full λ is negative and $J = L + S$ is the ground state.

In Table 1, we show the quantum numbers for the trivalent lanthanide ions, the Landé g-factor, and the high-temperature paramagnetic moment given as:

$$\mu_{\mathrm{t}} = \sqrt{\langle\hat{\mu}^2\rangle} = \mu_{\mathrm{B}} g_J \sqrt{J(J+1)}, \tag{5}$$

assuming that only the f-electrons contribute to the magnetic moment. If we know the energy levels of the lanthanide ions in a magnetic field, we can use standard statistical mechanics to calculate the susceptibility of the ions. For most of the ions,

TABLE 1 Quantum numbers and total f-electron magnetic moments of the trivalent lanthanide ions. μ_t is the magnetic moment calculated from Eq. (5). μ_e is the measured magnetic moment. All magnetic moments are expressed in Bohr magnetons

	S	L	J	Ground state	g_j	μ_t	μ_e[a]
La	0.00	0.00	0.00	$^1S_0$			
Ce	0.50	3.00	2.50	$^2F_{5/2}$	6/7	2.54	2.4
Pr	1.00	5.00	4.00	$^3H_4$	4/5	3.58	3.5
Nd	1.50	6.00	4.50	$^4I_{9/2}$	8/11	3.62	3.5
Pm	2.00	6.00	4.00	$^5I_4$	3/5	2.68	
Sm	2.50	5.00	2.50	$^6H_{5/2}$	2/7	0.85	1.5[b]
Eu	3.00	3.00	0.00	$^7F_0$		0.0	3.4[b,c]
Gd	3.50	0.00	3.50	$^8S_{7/2}$	2	7.94	7.95
Tb	3.00	3.00	6.00	$^7F_6$	3/2	9.72	9.5
Dy	2.50	5.00	7.50	$^6H_{15/2}$	4/3	10.65	10.6
Ho	2.00	6.00	8.00	$^5I_8$	5/4	10.61	10.4
Er	1.50	6.00	7.50	$^4I_{15/2}$	6/5	9.58	9.5
Tm	1.00	5.00	6.00	$^3H_6$	7/6	7.56	7.3
Yb	0.50	3.00	3.50	$^2F_{7/2}$	8/7	4.54	4.5
Lu	0.00	0.00	0.00	$^1S_0$			

[a] All experimental values taken from Kittel (1986).
[b] See text.
[c] Eu usually exists in the divalent form.

the difference in energy between the first excited state and the ground state is much greater than k_BT at room temperature, where k_B is the Boltzmann constant, and essentially only the ground state is populated. This enables us to derive the Curie formula

$$\chi = \frac{N\langle\hat{\mu}^2\rangle}{3k_BT} \tag{6}$$

for the susceptibility of a system of N non-interacting ions. More realistically, this formula should be replaced by the Curie-Weiss law, where the T in the denominator in Eq. (6) is replaced by $T-T_c$, where T_c is the magnetic ordering temperature. The Curie-Weiss formula was employed to determine the experimental magnetic moments, μ_e, in Table 1. For Sm^{3+} and Eu^{2+}, the first excited level is within k_BT of the ground state and so is appreciably populated. To describe these two ions with numerical accuracy, it is necessary to sum over the allowed values of J and recall that each J contains $2J + 1$ states. The susceptibility then becomes considerably more complicated but does give a good description of Sm^{3+} and Eu^{2+}.

The theoretical magnetic moments in Table 1 are for single trivalent ions assuming no inter-ionic interactions. However, the experiments are performed on metallic elements where each individual ion is embedded in a crystal and feels the crystalline electric field, which arises from charges on neighbouring ions. The excellent agreement between the magnetic moment measured experimentally and that obtained from Eq. (5) implies that the 4f-electrons are so well shielded that the effect of the crystalline environment can be neglected and the agreement with Eq. (6) supports this view. With the agreement between theory and experiment displayed in Table 1, it might reasonably be assumed that the magnetic moments of the lanthanide metals are well understood. While this is probably true qualitatively, it is certainly not true quantitatively. Questions about this model that may be raised are:

(1) In the solid state, the interaction with the sea of conduction electrons distorts the pure atomic picture, and multiplets other than the Hund's rule ground state mix into the full wave function. In view of the success of the atomic approximation, it is likely that this mixing of different J quantum numbers is at the few percent level, nonetheless this is an assumption that should be tested.

(2) The eigenfunctions $\Psi_{J,m_j,L,S}$ in Eq. (1) are generally quantum mechanically entangled, given as sums of Slater determinants constructed from atomic single-electron orbitals. The description of entangled quantum states in a solid state environment is extremely difficult. With the recent introduction of the DMFT (Section 3.8), one might have developed a scheme for this, however, more investigations are needed. Usually, one resorts to the independent particle approximation thus ignoring the 'many-body' nature of the wavefunction and the localized f-manifold is represented by a single 'best choice' Slater determinant. This is the approach taken in the various DFT schemes, including the SIC-LSD theory to be described in Section 3.5. How could such a picture arise from a more sophisticated and realistic description of the electronic structure of the lanthanides?

(3) The picture of lanthanide magnetism described above is for independent trivalent lanthanide ions. Thus, it does not explain cooperative magnetism, that is ordered magnetic structures which are the most common low-temperature ground states of lanthanide solids. Our view of a lanthanide crystal is of a regular array of such ions in a sea of conduction electrons to which each ion has donated three electrons. For cooperative magnetism to exist, those ions must communicate with one another somehow. It is generally accepted that this occurs through indirect exchange in the lanthanide metals, the simplest example of this being the RKKY interaction (Ruderman and Kittel, 1954; Kasuya, 1956; Yosida, 1957). However, for this to occur, the conduction sd-electrons themselves must be polarized. This conduction electron polarization has been calculated using DFT many times and is found to be substantial. There have been many successes in descriptions of magnetic structures, some of which will be discussed in Section 7.2. However, in terms of the size of magnetic moments, the agreement between theory and experiment shown in Table 1 is considerably worsened (see discussion in Section 5). Why is this?

(4) If the atomic model were rigorously correct, a lanthanide element would have the same magnetic moment in every material and crystalline environment. Of course, this is not the case, and more advanced methods have to be employed to determine the effect of the crystalline and chemical environment on magnetic moments with numerical precision. Examples of materials where the theory described above fails to give an accurate value for the lanthanide ion magnetic moment are ubiquitous. They include $NdCo_5$ (Alameda et al., 1982), fullerene encapsulated lanthanide ions (Mirone, 2005), and lanthanide pyrochlores (Hassan et al., 2003).

In conclusion, it is clear that the standard model makes an excellent first approximation to the magnetic properties of lanthanide materials, but to understand lanthanide materials on a detailed individual basis, a more sophisticated approach is required.

2.3 Fermi surfaces

The simple view of the lanthanide electronic structure as discussed previously is shown in Figure 3. The f-electrons are very localized, core-like, and responsible for magnetism, as described above, whereas the sd-electrons are responsible for other electronic properties, such as cohesive energy, transport properties, Fermi surfaces. This model, we call the standard model, is a good first approximation and a number of lanthanide properties can be explained in terms of it. The traditional DFT approach to the lanthanide electronic structure has involved a self-consistent calculation of the s, p, and d-bands with the filled f-states being treated as part of the core and the empty f-states essentially ignored. Again this approach works well and gives good agreement with experiment for structural and crystalline properties as well as de Haas van Alphen experiments and some spectroscopies. It has been used by a number of authors (Jackson, 1969; Skriver, 1983a, 1983b; Eriksson et al., 1990a) and yields band structures that look remarkable similar to hexagonal transition metals such as yttrium and scandium. A major advantage of this approach is the stability of the calculation due to the absence of the localized

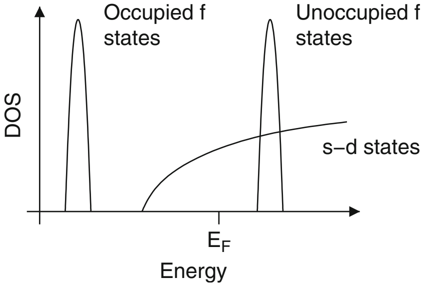

FIGURE 3 Model DOS for a lanthanide metal. The low-energy narrow peak represents the occupied f-band, the high-energy narrow peak just above the Fermi energy is the unoccupied f-states. These are superimposed on the sd-band which is free-electron like to a first approximation.

4fs. Both Skriver (1983b) and Eriksson et al. (1990a) have performed a successful calculation of the cohesive properties and the work of Skriver reproduces well the crystal structures which are sensitively dependent on the details of the valence band. For example, the partial 5d occupation numbers decrease across the series with a corresponding increase in the 6s occupation. The increase in 5d occupation is what causes the structural sequence hcp → Sm structure → dhcp → fcc as the atomic number decreases or the pressure increases (Duthie and Pettifor, 1977). A detailed analysis of Jackson's work (Jackson, 1969) on Tb yields a Fermi surface that shows features with wave vector separations corresponding to the characteristic wave vector describing the spiral phase of Tb.

One of the successes of this approach is the comparison of calculated electronic structures with de Haas van Alphen measurements. The investigations of the Fermi surface of Gd using this technique among others were pioneered by Young and co-workers (Young et al., 1973; Mattocks and Young, 1977) and extended by Schirber and co-workers (Schirber et al., 1976). These studies found four frequencies along the *c*-direction and three in the basal plane and later work found a number of small frequencies (Sondhelm and Young, 1977). All these frequencies could be accounted for on the basis of the band structure calculations of the time. Sondhelm and Young also measured cyclotron masses and mass enhancements in Gd and found values in the region of 1.2–2.1 which were in agreement with the band structure calculations, but were rather smaller than those derived from low-temperature heat capacity measurements. More recently, angle-resolved photoemission have been used for Fermi surface studies of Tb (Döbrich et al., 2007) and also Dy and Ho metals were studied (Schüßler-Langeheine et al., 2000). Fermi surfaces of Gd-Y alloys were studied with positron annihilation (Fretwell et al., 1999; Crowe et al., 2004). In particular, the changes to the Fermi surface topology upon the transition from ferromagnetism to helical anti-ferromagnetism could be followed. Concerning the light lanthanides, the Fermi surface areas and cyclotron masses in Pr were measured (Wulff et al., 1988) with the de Haas van Alphen technique. Large mass enhancements, especially for an elemental metal, were measured and the understanding of the Fermi surface needed an approach well beyond the standard model (Temmerman et al., 1993).

This standard model does have several major drawbacks:

(1) It can never get the magnetic properties correct.
(2) It cannot describe systems with large mass enhancements.
(3) There is one overarching shortcoming of the standard model, which is slightly more philosophical. It treats the f-electrons as localized and the sd-electrons as itinerant, that is, it treats electrons within the same material on a completely different basis. This is aesthetically unsatisfactory and furthermore makes it impossible to define a reference energy. In principle, one has to know, *a priori*, which electrons to treat as band electrons and which to treat as core electrons. It would be infinitely better if the theory itself contained the possibility of both localized and itinerant behaviour and it chose for itself how to describe the electrons.

For two elements, it is possible to perform LDA calculations including the f-electrons in the self-consistency cycle. The first is cerium where the f-electrons are not necessarily localized. Cerium and its compounds are right on the border between localized and itinerant behaviour of the 4f electrons. There has been much controversy over the nature of the f-state in materials containing cerium. The key issue is the γ–α phase transition where the localized magnetic moment associated with a $4f^1$ configuration disappears with an associated volume collapse of around 14–17%, but no change in crystal symmetry. The f electron count is thought to be around one in both phases of Ce. What appears to be happening here is a transition from a localized to a delocalized f-state (Pickett et al., 1981; Fujimori, 1983). Both Pickett et al. (1981) and Fujimori (1983) highlight the limitations of the band theory picture for cerium. In particular, Fujimori discusses the calculation of photoemission spectra and the reasons why band theory does not describe such spectroscopies well. The α-phase can be described satisfactorily using the standard band theory, while there is more difficulty in describing the γ-phase and the energy difference between the two phases (which is very small on the electronic scale) is not calculated correctly. The second lanthanide element where band theory may hope to shed some light on its properties is gadolinium. Here the f-levels are spilt into seven filled majority spin and seven unfilled minority spin bands, neither of which are close to the Fermi energy. It is feasible to perform a DFT calculation and converge to a reasonable result. This has been done by a number of authors (Jackson, 1969; Ahuja et al., 1994; Temmerman and Sterne, 1990) with mixed results. Temmerman and Sterne were among the first to indicate that the semi-band nature of the 5p levels could significantly influence predicted properties. Sandratsakii and Kübler (1993) took this work a bit further by investigating the stability of the conduction band moment with respect to disorder in the localized 4f-moment.

The experimentally determined Fermi surface of Gd (Schirber et al., 1976; Mattocks and Young, 1977) has been used by several band structure calculations to determine whether the f-states have to be treated as core-like or band-like. Gd metal is the most thoroughly studied of all the lanthanides and one of the few lanthanides that have been studied by the de Haas van Alphen technique (Schirber et al., 1976; Mattocks and Young, 1977). Being trivalent, it has, through the exchange splitting, a half-filled f-shell. The Gd f-states are well separated from the Fermi level, and therefore f-states are not contributing to the Fermi surface. This was seen in the Fermiology measurements (Schirber et al., 1976; Mattocks and Young, 1977). Both f-core (Richter and Eschrig, 1989; Ahuja et al., 1994) and f-band (Sticht and Kübler, 1985; Krutzen and Springelkamp, 1989; Temmerman and Sterne, 1990; Singh, 1991) calculations claim to be able to describe this Fermi surface.

While these methods provide some useful insight into Gd and Ce, they yield unrealistic results for any other lanthanide material as the f-bands bunch at the Fermi level leading to unphysically large densities of states at the Fermi energy and disagreement with the de Haas van Alphen measurements. It is clear that a satisfactory theory of lanthanide electronic structures requires a method that treats all electrons on an equal footing and from which both localized and itinerant behaviour of electrons may be derived. SIC to the LSDA provide one such theory.

This method is based on DFT and the free electron liquid, but corrects it for electrons where self-interactions are significant and takes the theory towards a more localized description.

3. BAND STRUCTURE METHODS

As described in Section 1, there exist many theoretical approaches to calculating electronic structure of solids, and most of them have also been applied to lanthanides. In this section, we shall briefly overview some of the most widely used, focusing however on the SIC-LSD, in both full and local implementations, as this is the method of choice for most of the calculations reported in this chapter. The simplest approach to deal with the f electrons is to treat them like any other electron, that is, as itinerant band states. Hence, we start our review of modern methods with a brief account of the standard LDA and its spin-polarized version, namely the LSD approximation. We also comment on the use of LSD in the cases, where one restricts the variational space by fixing the assumed number of f electrons to be in the (chemically inert) core ('f-core' approach). Following this, we then briefly overview the basics of other, more advanced, electronic structure methods mentioned in Section 1, as opposed to a more elaborate description of the SIC-LSD method.

3.1 Local spin density approximation

DFT relies on the proof (Hohenberg and Kohn, 1964; Kohn and Sham, 1965; Dreizler and Gross, 1990; Martin, 2004) that for any non-degenerate many-electron system, there exists an energy functional $E[n]$, where $n(\mathbf{r})$ is the electron charge density in space-point $\mathbf{r}$, which when minimized (with respect to $n(\mathbf{r})$) provides the correct ground state energy as well as ground state electron charge density. Hence, the charge density $n(\mathbf{r})$, rather than the full many-electron wave-function $\Psi(\mathbf{r}_1, \mathbf{r}_2, \ldots, \mathbf{r}_N)$, becomes the basic variable, which constitutes a simplification from a complex-valued function depending on N sets of space coordinates to a non-negative function of only one set of space coordinates. The price paid is that the exact functional form of $E[n]$ is unknown, and presumably of such complexity that it will never be known. However, approximations of high accuracy for a diversity of applications exist and allow predictive investigations of many novel functional materials in condensed matter physics and materials science. The great advance in the field was facilitated by the observation (Kohn and Sham, 1965) that if one separates out from the total energy functional, $E[n]$, the kinetic energy, $T_0[n]$, of a non-interacting electron gas with charge density $n(\mathbf{r})$ (which does not coincide with the true kinetic energy of the system), and the classical electrostatic energy terms, then simple, yet accurate, functionals may be found to approximate the remainder, called the exchange-correlation (xc) energy functional $E_{\mathrm{xc}}[n]$. Thus, the total energy functional can be written as

$$E[n] = T_0[n] + U[n] + V_{\mathrm{ext}}[n] + E_{\mathrm{xc}}[n], \tag{7}$$

where the electron–electron interaction (Hartree term) is given by

$$U[n] = \int\int \frac{n(\mathbf{r})n(\mathbf{r}')}{|\mathbf{r}-\mathbf{r}'|}\mathrm{d}^3r\mathrm{d}^3r', \tag{8}$$

and the external potential energy, $V_{\mathrm{ext}}[n]$, due to electron–ion and ion–ion interactions, respectively, is

$$V_{\mathrm{ext}}[n] = \int n(\mathbf{r})V_{\mathrm{ion}}(\mathbf{r})\mathrm{d}^3r + E_{\mathrm{ion,ion}}. \tag{9}$$

Here $V_{\mathrm{ion}}(\mathbf{r})$ is the potential from the ions, and the atomic Rydberg units $\left(e^2/2 = 2m = \hbar = 1\right)$ have been used in all the formulas. Since Eqs. (8) and (9) are explicitly defined in terms of the electron charge density, all approximations are applied to the last term in Eq. (7), the exchange and correlation energy.

In the LDA, it is assumed that each point in space contributes additively to E_{xc}:

$$E_{\mathrm{xc}}^{\mathrm{LDA}}[n] = \int n(\mathbf{r})\varepsilon_{\mathrm{hom}}(n(\mathbf{r}))\mathrm{d}^3r, \tag{10}$$

where $\varepsilon_{\mathrm{hom}}(n)$ is the exchange and correlation energy of a homogeneous electron gas with charge density n. In the simplest case, when only exchange is considered, one has (Hohenberg and Kohn, 1964)

$$\varepsilon_{\mathrm{hom}}(n) = -Cn^{1/3} \text{ with } C = \frac{3}{2}\left(\frac{3}{\pi}\right)^{1/3}. \tag{11}$$

Modern functionals include more elaborate expressions for $\varepsilon_{\mathrm{hom}}(n)$ (Vosko et al., 1980; Perdew and Zunger, 1981) relying on accurate Quantum Monte Carlo data for the homogeneous electron gas (Ceperley and Alder, 1980). Generalizing to magnetic solids, which is highly relevant for lanthanide materials, is straightforward as one merely has to consider two densities, one for spin-up and one for spin-down electrons, which corresponds to the LSD functional (von Barth and Hedin, 1972), E^{LSD}. Even more accurate calculations may be obtained by including corrections for the spatial variation of the electron charge density, which is accomplished by letting $\varepsilon_{\mathrm{hom}}$ also be dependent on gradients of the charge density, which constitutes the GGA (Perdew and Wang, 1992). Yet more accurate functionals may be composed by mixing some non-local exchange interaction into the E_{xc} (Becke, 1993), often named hybrid functionals.

The minimization of $E[n]$, with these approximate functionals, is accomplished by solving a one-particle Schrödinger equation for an effective potential, which includes an exchange-correlation part given by the functional derivative of $E_{\mathrm{xc}}[n]$ with respect to $n(\mathbf{r})$. The non-interacting electron gas system with the charge density $n(\mathbf{r})$ is generated by populating the appropriate number of lowest energy solutions (the aufbau principle). Self-consistency must be reached between the charge density put into the effective potential and the charge density composed from the occupied eigenstates. This is usually accomplished by iterating the procedure until this condition is fulfilled.

Spin-orbit interaction is only included in the density functional framework if the proper fully relativistic formalism is invoked (Strange, 1998). Often an approximate treatment of relativistic effects is implemented, by solving for the kinetic energy in the scalar-relativistic approximation (Skriver, 1983a), and adding to the total energy functional the spin-orbit term as a perturbation of the form

$$E_{\text{so}} = \sum_{\alpha}^{\text{occ.}} \langle \psi_\alpha | \xi(\vec{r})\, \vec{l} \cdot \vec{s}\, | \psi_\alpha \rangle, \tag{12}$$

where the sum extends over all occupied states $|\psi_\alpha\rangle$ and ξ is the spin-orbit parameter. Here $\vec{l}$ and $\vec{s}$ denote the one-particle operators for angular and spin moments. The method presupposes, which usually does not pose problems, that an appropriate region around each atom may be defined inside which the angular momentum operator acts.

The LDA and LSD, as well as their gradient corrected improvements, have been extremely successful in providing accurate, material specific, electronic, magnetic, and structural properties of a variety of weakly to moderately correlated solids, in terms of their ground state charge density (Jones and Gunnarsson, 1989; Kübler, 2000), However, these approaches often fail for systems containing both itinerant and localized electrons, and in particular d- and f-electron materials. For all lanthanides, and similarly the actinide elements beyond neptunium, the electron correlations are not adequately represented by LDA. In d-electron materials, for example, transition metal oxides, this inadequate description of localized electrons leads commonly to the prediction of wrong magnetic ground states and/or too small or non-existent band gaps and magnetic moments.

When applied to lanthanide systems, LSD (and GGA as well) leads to the formation of narrow bands which tend to fix and straddle the Fermi level. Due to their spatially confined nature, the f-orbitals hybridize only weakly and barely feel the crystal fields. Furthermore, on occupying the f-band states, the repulsive potential on the lanthanide increases due to the strong f–f Coulomb repulsion, so the f-bands fill up to the point where the total effective potential pins the f-states at the Fermi level. Generally, the band scenario leads to distinct overbinding (when compared to experimental data), since the occupation of the most advantageous f-band states favours crystal contraction (leading to increase in hybridization). Hence, the partially filled f-bands provide a negative pressure, which in most cases is unphysical. The same effect is well known to cause the characteristic parabolic behaviour of the specific volumes of the transition metals, and would lead to a similar parabolic behaviour for the specific volumes of the lanthanides, which is in variance with the observation seen in Figure 1 in Section 2.1. This will be discussed further in Section 4.2. Even if narrow, the f-bands in the vicinity of the Fermi level alone cannot describe the heavy fermion behaviour seen in many cerium and ytterbium compounds. Zwicknagl (1992) and co-workers applied a renormalization scheme to LDA band structures to describe the heavy fermion properties with successful application in particular to the understanding of Fermi surfaces.

3.2 'f Core' approach

To remedy the failure of LSD, it was early realized that one could remove the spurious bonding due to f-bands by simply projecting out the f-degrees of freedom from variational space and instead include the appropriate number of f electrons in the core. This approach was used to study the crystal structures of the lanthanide elements (Duthie and Pettifor, 1977; Delin et al., 1998), which are determined by the number of occupied d-states. In this approach, the lanthanide contraction neatly follows as an effect of the incomplete screening of the increasing nuclear charge by added f electrons, as one moves through the lanthanide series (Johansson and Rosengren, 1975). In a recent application, the 'f core' approach proved useful in the study of complex magnetic structures (Nordström and Mavromaras, 2000).

Johansson and co-workers have extended the 'f core' approach to compute energies of lanthanide solids, with different valencies assumed for the lanthanide ion, by combining the calculated LSD total energy for the corresponding 'f core' configurations with experimental spectroscopic data for the free atom (Delin et al., 1997). This scheme correctly describes the trends in cohesive energies of the lanthanide metals, including the valence jumps at Eu and Yb, as well as the intricate valencies of Sm and Tm compounds.

3.3 OP scheme

The OP scheme was introduced by Eriksson et al. (1990b) to reduce the bonding of f-electrons without totally removing them from the active variational space. The idea copies the way spin polarization leads to reduced bonding if the exchange parameter is large enough (Kübler and Eyert, 1993). An extra term is added to the LSD functional (7):

$$E^{\mathrm{OP}}[n] = E^{\mathrm{LSD}}[n] - \sum_i E_i^3 L_{zi}^2, \tag{13}$$

where i numbers the atomic sites, L_{zi} is the total z-component of the orbital moment, and E_i^3 is a parameter (the Racah parameter), which can be calculated from an appropriate combination of Slater integrals (Eriksson et al., 1990b). The added term favours the formation of an orbital moment and adds a potential shift $-E_i^3 L_{zi} m_l$ to each f orbital, where m_l is the azimuthal quantum number of the f electron considered. The effect is to partially split the f-band into 14 distinct bands (if the E^3 parameter exceeds hybridization and crystal fields). Since compression enhances the latter two effects, the OP scheme could successfully describe the γ–α transition of cerium as a transition from large to low orbital moment (Eriksson et al., 1990b). This is then to be interpreted as a Mott-type transition in the f-manifold from a localized to a band-like behaviour. The OP scheme has also been applied to the pressure-induced volume collapse in Pr (Svane et al., 1997). Generally, the OP term is too small in magnitude to fully describe the inertness of the f electrons in the lanthanide series beyond Pr. The OP scheme has been most successful in describing the orbital moment contribution to itinerant systems, for example 3d-transition metal and actinide compounds (Eriksson et al., 1991; Trygg et al., 1995). The LSD (with spin-orbit interaction included) grossly underestimates orbital moments since there is no energy term describing the energetics of the Hund's second rule. The OP term in Eq. (13) remedies this as it largely describes the extra energy gain of an f-manifold by attaining its ground state configuration (compared to the average, 'grand bary centre' energy of the f-manifold). Eschrig et al. (2005), by analysing the formal relativistic DFT framework, showed that the functional form chosen by Eriksson et al. (1990b) is in fact quite accurate.

3.4 Local density approximation + Hubbard U

Similarly to the OP scheme, the LDA + U method (Anisimov et al., 1991) adds a quadratic term to the LSD Hamiltonian to improve the description of the correlated f-manifold, namely

$$E^{\mathrm{LDA+U}}[n] = E^{\mathrm{LSD}}[n] + \sum_i E^{\mathrm{corr}}(\underline{N}_i), \tag{14}$$

where for each site i, the correlation energy term depends on the orbital occupation numbers $\underline{N} = \{N_k\}$. These are obtained by projecting the occupied eigenstates $|\psi_\alpha\rangle$ onto the f orbitals, $|f_k\rangle$, as

$$N_k = \sum_{\alpha}^{\mathrm{occ.}} |\langle\psi_\alpha|f_k\rangle|^2. \tag{15}$$

In its simplest form (Anisimov et al., 1991), the correlation energy term includes a Hubbard repulsion term (Hubbard, 1963) and the so-called double-counting term E_{dc}

$$E^{\mathrm{corr}}(\underline{N}) = \frac{1}{2}U\sum_{k\neq l} N_k N_l + E_{\mathrm{dc}}. \tag{16}$$

Here, indices k and l run over the 14 f orbitals on the site considered, and U is the f–f Coulomb interaction. The double-counting term E_{dc} is needed to correct for the fact that $E^{\mathrm{LSD}}[n]$ already includes some Coulomb correlation contribution. A major deficiency of the LDA + U method is that E_{dc} is not easily estimated, and therefore several forms of this correction have been introduced (Anisimov et al., 1991, 1993; Lichtenstein et al., 1995), each leading to some differences in results (Mohn et al., 2001; Petukhov et al., 2003). The appropriate value to use for U is somewhat uncertain, since it necessarily must include screening from the conduction electrons, which reduces the Coulomb interaction by a factor of 3–4 compared to the bare f–f Coulomb interaction energy. Its value may be deduced from constrained LDA calculations (Anisimov and Gunnarsson, 1991), by which the energy change due to an enforced increase of f occupancy is calculated, including effects of screening. However, this is an approximate procedure due to the intractable correlation effects inherent in the LDA.

The physical idea behind the LDA + U correction is like for the OP scheme (section 3.3) to facilitate an orbital imbalance within the f-manifold with ensuing loss in f contribution to bonding. However, the U parameter is significantly larger, usually in the range of 6–10 eV for lanthanides, compared to the E^3 parameter used in Eq. (13), which is of the order 0.1 eV in lanthanides. Therefore, LDA + U strongly favours OP and for lanthanides, generally pushes the f-bands either far below or far above the Fermi level (lower and upper Hubbard bands), that is the occupation numbers N_k attain values of either ~1 or ~0. For this reason, the LDA + U scheme has not been applied to describe valence transitions. Improved descriptions include an exchange interaction parameter in the f-manifold with spin-polarization of the conduction electrons (LSD + U), and/or a rotationally invariant formulation (Lichtenstein et al., 1995), by which the dependence on representation (e.g., spherical versus cubic harmonics) is avoided. In full implementation, this latter scheme introduces band shifts reminiscent of multiplet splittings (Gotsis and Mazin, 2003; Duan et al., 2007).

The LDA + U has been extensively used in studies of lanthanides, but a comprehensive review will not be given here. Some significant applications and reviews are reported in Antonov et al. (1998), Gotsis and Mazin (2003), Duan et al. (2007), Larson et al. (2007), and Torumba et al. (2006). The method is almost as fast as a conventional band structure method, and when comparisons to experimental photoemission experiments are made, the LDA + U method provides a much improved energy position of localized bands over the LDA/LSD. In addition, often, the precise position of occupied f-states is not essential to describe bonding properties, rather the crucial effect is that the f-states are moved away from the Fermi level.

3.5 Self-interaction-corrected local spin density approximation

In solids containing localized electrons, the failure of LDA, LSD, as well as their gradient improvements can to a large extent be traced to the self-interaction error inherent in these approaches. The self-interaction problem of effective one-electron theories of solids has been realized for a long time (Cowan, 1967; Lindgren, 1971). The favoured formulation within the DFT framework is due to Perdew and Zunger (Zunger et al., 1980; Perdew and Zunger, 1981).

Consider first a system of a single electron moving in an arbitrary external potential $V_{\text{ext}}(\mathbf{r})$. The wavefunction, Ψ_1, is the solution to the Schrödinger equation

$$\left(-\nabla^2 + V_{\text{ext}}\right)\psi_1 = \varepsilon_1\psi_1. \tag{17}$$

From this, the energy may easily be calculated as:

$$\varepsilon_1 = \langle\psi_1|-\nabla^2 + V_{\text{ext}}|\psi_1\rangle = T_0[n_1] + V_{\text{ext}}[n_1], \tag{18}$$

where the density is simply $n_1(r) = |\psi_1(r)|^2$, and T_0 is the kinetic energy and V_{ext} given by Eq. (9). When the same system is treated within DFT, the energy is written as in Eq. (7), that is, the two additional terms must cancel:

$$U[n_1] + E_{\text{xc}}[n_1] = 0. \tag{19}$$

This is a fundamental property of the true exchange-correlation functional, E_{xc}, valid for any one-electron density. In the LSD, E_{xc} is approximated, and the self-Coulomb and self-exchange do not cancel anymore. One speaks of spurious self-interactions that are introduced by the approximations in the local functionals (Dreizler and Gross, 1990).

Next we consider a many-electron system. When the electron density is decomposed into one-electron orbital densities, $n = \sum_{\alpha} n_{\alpha}$, it is straightforward to see that the Hartree term, Eq. (8), contains a contribution, $U[n_{\alpha}]$, that describes the electrostatic energy of orbital α interacting with itself. In the exact DFT, this self-interaction term is cancelled exactly by the self-exchange contribution to E_{xc} in the sense of Eq. (19) for orbital α, but not when approximate functionals are used for E_{xc}. The remedy to the self-interaction problem proposed by Perdew and Zunger (1981) was simply to subtract the spurious self-interactions from the LSD functional for each occupied orbital. Their SIC-LSD functional has the form

$$\begin{aligned} E^{\mathrm{SIC-LSD}} &= E^{\mathrm{LSD}} - \sum_{\alpha}^{\mathrm{occ.}} \delta_{\alpha}^{\mathrm{SIC}} \\ &= \sum_{\alpha}^{\mathrm{occ.}} \langle \psi_{\alpha} | -\nabla^2 | \psi_{\alpha} \rangle + V_{\mathrm{ext}}[n] + U[n] + E_{\mathrm{xc}}^{\mathrm{LSD}}[n_{\uparrow}, n_{\downarrow}] - \sum_{\alpha}^{\mathrm{occ.}} \delta_{\alpha}^{\mathrm{SIC}}. \end{aligned} \tag{20}$$

Here the sums run over all the occupied orbitals ψ_{α}, with the SIC given by

$$\delta_{\alpha}^{\mathrm{SIC}} = U[n_{\alpha}] + E_{\mathrm{xc}}^{\mathrm{LSD}}[n_{\alpha}], \tag{21}$$

where

$$n_{\alpha} = |\psi_{\alpha}|^2 \tag{22}$$

and α is a combined index comprising all the relevant quantum numbers of the electrons. The spurious self-interactions are negligible for extended orbitals, but are substantial for spatially localized orbitals.

When applied to atoms, the most extreme case where all electrons occupy localized orbitals, the SIC-LSD functional drastically improves the description of the electronic structure (Perdew and Zunger, 1981). In solids, where not all electrons occupy localized orbitals, one has to deal with an *orbital-dependent* SIC-LSD functional [Eq. (20)]. In addition, since the LSD exchange-correlation functional depends non-linearly on the density, the SIC [Eq. (21)] and hence the SIC-LSD functional [Eq. (20)] are *not* invariant under unitary transformations of the occupied states, and therefore one is faced with a daunting functional minimization problem (Temmerman et al., 1998).

The minimization condition for the SIC-LSD functional in Eq. (20) gives rise to a generalized eigenvalue problem with an orbital dependent potential as

$$H_{\alpha}\psi_{\alpha}(\mathbf{r}) \equiv \left[-\nabla^2 + V^{\mathrm{LSD}}(\mathbf{r}) + V_{\alpha}^{\mathrm{SIC}}(\mathbf{r})\right]\psi_{\alpha}(\mathbf{r}) = \sum_{\alpha'}^{\mathrm{occ.}} \varepsilon_{\alpha\alpha'}\psi_{\alpha'}(\mathbf{r}), \tag{23}$$

with the Lagrange multipliers matrix, $\varepsilon_{\alpha\alpha'}$, ensuring the orthonormality of the orbitals. Since the SIC is only non-zero for localized electrons (Perdew and Zunger, 1981), the localized and delocalized electrons experience different potentials. The latter move in the LSD potentials, defined by the ground state charge density of all the occupied states (including the localized, SIC, states), whereas the former experience a potential from which the self-interaction term has been subtracted. Hence, in this formulation, one distinguishes between localized and itinerant states but treats them on equal footing. The decision whether a state is to be treated as localized or extended is based on a delicate energy balance between band formation and localization. As a result, one has to explore a variety of configurations consisting of different distributions of localized and itinerant states. The minimization of the SIC-LSD total energy functional with respect to those configurations defines the global energy minimum and thus the ground state energy and configuration. In addition, to ensure that the localized orbitals are indeed the most optimally localized ones, delivering the absolute energy minimum, a localization criterion (Pederson et al., 1984, 1985)

$$\langle \psi_\alpha | V_\alpha^{\mathrm{SIC}} - V_{\alpha'}^{\mathrm{SIC}} | \psi_{\alpha'} \rangle = 0 \tag{24}$$

is checked at every iteration of the charge self-consistency process. The fulfilment of the above criterion is equivalent to ensuring that the Lagrange multiplier matrix in Eq. (23) is Hermitian, and the energy functional is minimal with respect to the unitary rotations among the occupied orbitals. The resulting SIC-LSD method is a first-principles theory for the ground state with no adjustable parameters. It is important to realize that the SIC-LSD functional subsumes the LSD functional, as in this case all electrons (besides the core electrons) are itinerant, which corresponds to the configuration where SIC is not applied to any orbitals, and thus the solution of the SIC-LSD functional is identical to that of the LSD.

The SIC constitutes a negative energy contribution gained by an f-electron when localizing, which competes with the band formation energy gained by the f-electron if allowed to delocalize and hybridize with the available conduction states. The volume dependence of δ_α is much weaker than the volume dependence of the band formation energy of lanthanide's 4f (or actinide's 5f) electrons, hence the overbinding of the LSD approximation for narrow f-band states is reduced when localization is realized.

One major advantage of the SIC-LSD energy functional is that it allows one to determine valencies of the constituent elements in the solid. This is accomplished by realizing different valence scenarios, consisting of atomic configurations with different total numbers of localized and itinerant states. The nominal valence is defined as the integer number of electrons available for band formation, namely

$$N_{\mathrm{val}} = Z - N_{\mathrm{core}} - N_{\mathrm{SIC}}, \tag{25}$$

where Z is the atomic number, N_{core} is the total number of core (and semi-core) electrons, and N_{SIC} is the number of localized, SIC, states. The self-consistent minimization of the total energy with different configurations gives rise to different local minima of the same functional, $E^{\mathrm{SIC-LSD}}$ in Eq. (20), and hence their total energies may be compared. The configuration with the lowest energy defines the ground state configuration and the ensuing valence, according to Eq. (25). As already mentioned, if no localized states are realized, $E^{\mathrm{SIC-LSD}}$ coincides with the conventional LSD functional, that is, the Kohn-Sham minimum of the E^{LSD} functional is also a local minimum of $E^{\mathrm{SIC-LSD}}$. A second advantage of the SIC-LSD scheme is that one may consider localized f-states of different symmetry. In particular, the various crystal field eigenstates, either magnetic or paramagnetic may be investigated.

The SIC-LSD still considers the electronic structure of the solid to be built from individual one-electron states, but offers an alternative description to the Bloch picture, namely in terms of periodic arrays of localized atom-centred states (i.e., the Heitler-London picture in terms of the exponentially decaying Wannier orbitals). Nevertheless, there still exist states that will never benefit from the SIC. These states retain their itinerant character of the Bloch form and move in the effective LSD potential. This is the case for the non-f conduction electron states in the lanthanides. In the SIC-LSD method, the eigenvalue problem, Eq. (23), is solved in the space of Bloch states, but a transformation to the Wannier representation is made at every step of the self-consistency process to calculate the localized orbitals and the corresponding charges that give rise to the SIC potentials of the states that are truly localized. These repeated transformations between Bloch and Wannier representations constitute the major difference between the LSD and SIC-LSD methods.

It is easy to show that although the SIC-LSD energy functional in Eq. (20) appears to be a functional of all the one-electron orbitals, it can in fact be rewritten as a functional of the total (spin) density alone, as discussed by Svane (1995). The difference with respect to the LSD energy functional lies solely in the exchange-correlation functional, which is now defined to be self-interaction free. Since, however, it is rather impractical to evaluate this SIC exchange-correlation functional, one has to resort to the orbital-dependent minimization of Eq. (20).

Since the main effect of the SIC is to reduce the hybridization of localized electrons with the valence band, the technical difficulties of minimizing the SIC-LSD functional in solids can often be circumvented by introducing an empirical Coulomb interaction parameter U on the orbitals that are meant to be localized, which leads to the LDA + U approach, discussed in Section 3.4. The original derivation of the LDA + U approach (Anisimov et al., 1991) was based on the conjecture that LDA can be viewed as a homogeneous solution of the Hartree-Fock equations with equal, averaged, occupations of localized d- and/or f-orbitals in a solid. Therefore, as such, it can be modified to take into account the on-site Coulomb interaction, U, for those orbitals to provide a better description of their localization. The on-site Hubbard U is usually treated as an adjustable parameter, chosen to optimize agreement with spectroscopy experiments, and thus the method looses some of its predictive power. In contrast, SIC-LSD has no adjustable parameters and is not designed to agree with spectroscopy experiments. The LDA-based band structure is often compared to photoemission experiments. This is because the effective Kohn-Sham potentials can be viewed as an energy-independent self-energy and hence the Kohn-Sham energy bands correspond to the mean field approximation for the spectral function. In the SIC-LSD, this argument only applies to the itinerant states that are not SI-corrected. The localized states that have been SI-corrected respond to a different potential, and the solution of the generalized SIC-LSD eigenvalue problem, which is different from the solution to the Kohn-Sham equations in the LDA, no longer corresponds to a mean field approximation of the spectral function. Nevertheless, one can make contact with spectroscopies by performing the so-called Δ_{SCF} calculations (Freeman et al., 1987), or utilize the transition state concept of Slater (1951). The most advanced procedure, however, would be to combine the SIC-LSD with the GW approach (see Section 3.7) to obtain both the real and imaginary part of an energy-dependent self-energy and the excitation spectrum for both localized and itinerant states.

Finally, given the above SIC-LSD total energy functional, the computational procedure is similar to the LSD case, that is minimization is accomplished by iteration until self-consistency. In the present work, the electron wavefunctions are expanded in LMTO basis functions (Andersen, 1975; Andersen et al., 1989), and the energy minimization problem becomes a non-linear optimization problem in the expansion coefficients, which is only slightly more complicated for the SIC-LSD functional than for the LDA/LSD functionals. Further technical details of the present numerical implementation can be found in Temmerman et al. (1998).

3.6 Local self-interaction-corrected local spin density approximation

A local formulation of the self-interaction-corrected (LSIC) energy functionals has been proposed and tested by Lüders et al. (2005). This local formulation has increased the functionality of the SIC methodology as presented in Section 3.5. The LSIC method relies on the observation that a localized state may be recognized by the phase shift, η_l, defined by the logarithmic derivative:

$$D_\ell = \frac{S\phi'_\ell(S)}{\phi_\ell(S)}, \tag{26}$$

passing through a resonance. Here, S denotes the atomic radius, and $\phi_\ell(S)$ and $\phi'_\ell(S)$ are, respectively, the partial wave and its derivative at radius S with angular character ℓ. Specifically, the phase shift is given as

$$\tan(\eta_\ell(E)) = \frac{D_\ell - D^-_{0\ell}}{D_\ell - D^+_{0\ell}}. \tag{27}$$

D^-_0 and D^+_0 denote the corresponding logarithmic derivatives for the regular and irregular radial waves in zero potential, respectively (Martin, 2004). For a quasi-localized (resonant) state, the phase shift increases rapidly around the energy of that state and goes through a resonance, that is jumps from 0 to π passing rapidly through $\pi/2$. The energy derivative of the phase shift is related to the Wigner delay-time (Taylor, 1972). If this is large, which is the case for a resonance, the electron spends a long time in the corresponding atomic orbital. Such 'slow' electron will be much more affected by the relaxations of other electrons in response to its presence, and therefore should see a SIC potential.

The phase shift carries all necessary information about the local potential and is the fundamental quantity in the multiple scattering formalism of the electronic structure problem (Martin, 2004). In this approach, the solid state Green's function is formulated in terms of the scattering matrix (t-matrix), which is calculated from the phase shifts for constituent atoms at different angular momentum quantum numbers and a purely geometrical part expressed by the so-called structure constants. For the LSIC formulation, one merely replaces the scattering potential at a given resonant channel with the SIC potential. The local aspect of the approach is due to the SI-corrected potential being confined to the atomic sphere of the correlated atom.

Because of the multiple scattering aspect of the LSIC approach, we can easily calculate the Green's functions and various observables from them for making contact with experiments, most notably the total energy given by Eq. (21) and, as for the full SIC of Section 3.5, also valencies. The great potential of the Green's function formulation of the SIC-LSD method is that it can be easily generalized to study different types of disorder such as chemical, charge, and spin disorder. This is accomplished by combining LSIC with the CPA (Soven, 1967; Gyorffy and Stocks, 1978; Stocks et al., 1978; Faulkner and Stocks, 1981; Stocks and Winter, 1984). The CPA is the best possible single-site mean field theory of random disorder. In conjunction with the DLM formalism for spin fluctuations (Gyorffy et al., 1985; Staunton et al., 1986), the method allows also for different orientations of the local moments of the constituents involved, which will be demonstrated in Section 7.2 on the study of the finite temperature magnetism of the heavy lanthanide elements. The CPA used with the LSIC allows to study chemical disorder by investigating alloys of lanthanides, and to treat valence fluctuations by implementing an alloy analogy for a variety of phases, whose constituents are composed of, for example, two different configurations of a system, say f^n and f^{n+1} of a given lanthanide ion. In the latter application, thermal fluctuations are mapped onto a disordered system. If the total energies of these configurations are sufficiently close, one can envisage dynamical effects playing an important role as a consequence of tunnelling between these states. Such quantum fluctuations become important at low temperatures. In Section 7.3, we explore the thermal fluctuations for the study of the Ce $\alpha \rightarrow \gamma$ phase transition at finite temperatures, and in Section 8, we outline how to evaluate the quantum fluctuations. To fully take into account the finite temperature effects, one has to calculate the free energy of a system (pseudo-alloy), as a function of temperature, T; volume, V; and concentration, c, namely

$$F(T,c,V) = E_{\text{tot}}(T,c,V) - T\big(S_{\text{el}}(T,c,V) + S_{\text{mix}}(c) + S_{\text{mag}}(c) + S_{\text{vib}}(c)\big). \quad (28)$$

Here S_{el} is the electronic (particle-hole) entropy, S_{mix} the mixing entropy of the alloy, S_{mag} the magnetic entropy, and S_{vib} the entropy originating from the lattice vibrations. The discussion of cerium in Section 7.3 includes finite temperature effects along these lines.

3.7 The GW method

The GW method (Hedin, 1965; Aryasetiawan and Gunnarsson, 1998) is aimed at a precise determination of the excitations of the solid state system, which is fundamentally different from the focus on ground state properties of the density functional methods outlined in the preceding sections. In GW, the central object is the Green's function (Mahan, 1990). The excitation (quasi-particle) energies ω_α including correlations are expressed through the following equation

$$\left(\omega_\alpha - \hat{H}_0\right)\psi_\alpha(\mathbf{r}) - \int \Sigma(\omega_\alpha,\mathbf{r},\mathbf{r}')\psi_\alpha(\mathbf{r}')\mathrm{d}^3\mathrm{r}' = 0. \tag{29}$$

Here, $\hat{H}_0$ denotes the Hamiltonian for the uncorrelated (reference) system, whereas ψ_α denote the quasi-particle wavefunctions and Σ is the self-energy. The physical meaning of this equation is that Σ, through the integration in the last term, causes a shift of the eigenenergy from ε_α in the non-interacting case (assuming $\hat{H}_0\psi_\alpha \sim \varepsilon_\alpha\psi_\alpha$) to ω_α with interactions turned on. Obviously, Σ is the crucial quantity to determine. The Green's function G of the interacting system is in fact given by

$$G(\omega) = (\omega - \varepsilon_\alpha - \Sigma)^{-1}, \tag{30}$$

so that Eq. (29) may be seen as a search for poles in G.

The GW method takes its name from the approximation invoked to calculate Σ, namely $\Sigma = G_0W$, or explicitly

$$\Sigma(\omega,\mathbf{r},\mathbf{r}') = \frac{i}{2\pi}\int G_0(\omega+\omega',\mathbf{r},\mathbf{r}')W(\omega',\mathbf{r},\mathbf{r}')\mathrm{d}\omega'. \tag{31}$$

In this equation, G_0 is the Green's function of the uncorrelated reference system, whereas W denotes the screened Coulomb interaction. Commonly, G_0 is constructed from an LDA or LDA + U band structure, in which case, the reference system strictly speaking is not uncorrelated, but the potential due to correlation is the exchange-correlation potential, V_{xc}, which is explicitly known and can be subtracted from Σ, namely $\Sigma = \Sigma - V_{\mathrm{xc}}\delta(\mathbf{r}-\mathbf{r}')$.

In terms of the wavefunctions, $\psi^0_\alpha(\mathbf{r})$, of the reference system and the corresponding eigenenergies, ε_α, the reference Green's function reads

$$G_0(\omega,\mathbf{r},\mathbf{r}') = \sum_\alpha \frac{\psi^0_\alpha(\mathbf{r})\psi^{0*}_\alpha(\mathbf{r}')}{\omega - \varepsilon_\alpha \pm i\delta}, \tag{32}$$

where the sum is over the eigenstates of the reference system. The $\pm i\delta$ in the denominator in Eq. (32) is introduced as a mathematical trick to distinguish between occupied and unoccupied states.

The bare interaction between an electron in the position $\mathbf{r}$ and another electron in the position $\mathbf{r}'$ is

$$V(\mathbf{r}-\mathbf{r}') = \frac{1}{|\mathbf{r}-\mathbf{r}'|} \tag{33}$$

that becomes screened by the presence of the other electrons in the solid. This screening is expressed through the dielectric function, $\varepsilon(\omega, \mathbf{r}, \mathbf{r}')$, so that the effective interaction is

$$W(\omega,\mathbf{r},\mathbf{r}') = \int \varepsilon(\omega,\mathbf{r},\mathbf{r}')V(\mathbf{r}'-\mathbf{r})\mathrm{d}^3\mathrm{r}', \tag{34}$$

which defines the second ingredient of the GW method, Eq. (31). Note that the pure exchange, Hartree-Fock, approximation can also be expressed as a GV method.

The difficult part of this method is the evaluation of the dielectric function. In the simplest meaningful approximation, this is accomplished in the random phase approximation, in which ε is given explicitly in terms of the $\psi_{\alpha}^{0}(\mathbf{r})$ and ε_{α} of the reference system [see, e.g., Hybertsen and Louie (1986), Godby et al. (1988), Mahan (1990), and Aryasetiawan and Gunnarsson (1994, 1998) for technical details]. In the random phase approximation, the screening is mediated through the excitations of electron-hole pairs. The screening is dynamic leading to the ω-dependence of ε and hence Σ. This then leads to the very non-linear dependence on ω_{α} in Eq. (29). Further complications arise because ε is a complex valued function, the imaginary part contributing to finite lifetimes of quasi-particles.

A final issue to consider is which reference system is best suited. By far, most applications have used LDA as starting point, but for optimum consistency, the initial band structure should reflect as closely as possible the final result, for example for a semi-conductor, the screening properties are quite dependent on the fundamental gap, which however is consistently underestimated in the LDA and GGA band structures. This is in particular a problem when the LDA band structure is metallic, as happens for Ge (van Schilfgaarde et al., 2006a) and InN (Rinke et al., 2006). Likewise, for lanthanides, because of the localized nature of the f electrons, LDA and GGA are inadequate reference band structures for GW, whereas SIC-LSD or LDA + U might be better suited. Unfortunately, no GW calculations of this sort have been reported for lanthanide systems. Recently, van Schilfgaarde et al. (2006b) in their quasi-particle self-consistent GW approximation suggested to iterate the input band structure to the point that it comes as close as possible to the GW output band structure, which is the most consistent choice, but evidently requires more computing effort. They applied their approach to the lanthanide elements Gd and Er, as well as to the compounds GdAs and ErAs, and GdN, ErN, and YbN (Chantis et al., 2007). The calculations show the occupied f-bands shifted away from the Fermi level, with some multiplet-like splittings, showing good agreement with experimental photoemission spectra. The unoccupied f-bands appear 1–3 eV above their experimental positions. All in all, as far as the f-manifold is concerned, the GW band structure is quite LDA + U like, as indeed suggested by Anisimov et al. (1997). However, the authors do not find a straightforward mapping from GW to the appropriate parameters for LDA + U.

The greatest success of the GW method has hitherto been in the semiconducting solids, where the underestimate of the fundamental gap within LDA/GGA is greatly improved (Hybertsen and Louie, 1986; van Schilfgaarde et al., 2006b).

3.8 Dynamical mean field theory

The DMFT (Georges et al., 1996; Kotliar et al., 2006; Held, 2007) is a general framework for incorporating the self-energy of a correlated atom into the solid state environment. The basic assumption is that the correlation effects are local in nature, so that as a first step, the self-energy for a single atom may be computed in an otherwise uncorrelated environment, the conduction electron bath, which is described by the Green's function G_{bath}, that is:

$$\Sigma = \Sigma(G_{\text{bath}}). \tag{35}$$

This constitutes the DMFT impurity problem. Subsequently, the Green's function for the solid is constructed from

$$G^{-1} = G_0^{-1} - \Sigma(G_{\text{bath}}), \tag{36}$$

where G_0 is the Green's function of the uncorrelated solid, Eq. (32). From G, the solid state excitations can be obtained, for example the spectral function (generalized DOS) $A_{n\mathbf{k}}(\omega)$ is given as:

$$A_{n\mathbf{k}}(\omega) = \left|\frac{1}{\pi}\text{Im}G_{n\mathbf{k}}(\omega)\right|, \tag{37}$$

for the quasi-particle labelled by band and k-vector index $n\mathbf{k}$.

An intriguing aspect of DMFT is that the effective bath to be used in the impurity problem, Eq. (35), may be determined by averaging the solid state Green's function in Eq. (36) and subtracting the correlation term ($-\Sigma$), namely

$$[G_{\text{bath}}(\omega)]^{-1} = \left(\frac{1}{N_k}\sum_{\mathbf{k}}^{\text{BZ}} G_{\mathbf{k}}(\omega)\right)^{-1} + \Sigma(\omega). \tag{38}$$

Here, we explicitly write the averaging as a sum over the BZ. Hence, the imposed self-consistency condition is that the G_{bath} put into Eq. (35) should equal the G_{bath} extracted from Eq. (38) with Eq. (36). This is usually obtained via an iteration process (the DMFT self-consistency cycle).

Crucial to all DMFT calculations is how $\Sigma(G_{\text{bath}})$is evaluated. There are many possibilities and the quality of the calculation depends on this. Two aspects need to be specified, namely the model adopted to describe the correlation effects of the impurity atom and the method/approximation used to solve the impurity problem (the impurity solver), once the model has been chosen. The choice of the model requires physical insight. The Hubbard model (Hubbard, 1963) is the favoured choice in most approaches. Usually, it is necessary to reduce the number of degrees of freedom involved in the correlation problem to a minimum for computational reasons. Generally, the uncertainty of the double-counting term, haunting the LDA $+$ U method (Section 3.4), also prevails in the DMFT treatment. The method of solving the impurity problem can be either numerical, as in the Quantum Monte Carlo and exact diagonalization methods, or rely on approximate methods (which again require physical insight), for example perturbation theory. For details, we refer the reader to the recent reviews of DMFT (Kotliar et al., 2006; Held, 2007). In Section 6.1, we describe results of a particularly simple DMFT implementation that is well applicable to lanthanide compounds, in which the full multiplet structure of the lanthanide ion is computed; however, it ignores the coupling to the conduction sea.

Many DMFT calculations have been reported in recent years, the majority discussing 3d systems, but also several dealing with actinides. Less attention has been paid to the lanthanides, most probably because the atomic limit, as outlined Section 6.1, is sufficient for an accurate description in most cases. An important exception is the γ–α transition in cerium, which has been the subject of several studies (Held et al., 2001; Zölfl et al., 2001; McMahan et al., 2003; Haule et al., 2005; Amadon et al., 2006), all using the Hubbard model, but with various impurity solvers. Ce compounds have also been studied based on the Hubbard model (Lægsgaard and Svane, 1998; Sakai et al., 2005; Sakai and Shimuzi, 2007).

4. VALENCE AND VALENCE TRANSITIONS

4.1 Determining valence

Valence is a chemical concept but can be very useful in describing the lanthanides in the solid state, as it is strongly linked to their physical properties. In particular, valence changes can lead to anomalies of lattice parameters across the elemental lanthanides and their monopnictides and monochalcogenides (Jayaraman, 1978). Most of the lanthanide atoms in solids are trivalent, although in the atomic state, most are divalent (Gschneidner, 1971). However, there are exceptions to this rule, Eu, Yb metals are divalent, and in some compounds Eu, Sm, Tm, and Yb, can be either divalent or trivalent (Gschneidner, 1969). On the other hand, Ce, and its phases and compounds, can be either trivalent or tetravalent. Of course, not all the lanthanides and their compounds can be associated with an integer valence, and some of them are classified as intermediate- or mixed-valent systems, as it is the case for the heavy fermion materials.

In the ionic picture, divalent, trivalent, or tetravalent valence means that two, three, or four electrons, respectively, are chemically active. In the solid state context, lanthanide valence means that two, three, or four valence bands are occupied by two, three, or four electrons. In addition, unlike in the ionic picture, these valence band electrons can have s, p, d, and even f character, as it is often the case for the lanthanide materials.

The effect of SIC is different between atoms and solids. In the case of atoms, the levels are being populated in steps of one electron and the self-interaction is always large. In the solid state, the occupancy of a particular orbital can vary between zero and one, and whether to apply the SIC is determined by a competition between the band formation energy (no SIC) and the localization energy (application of SIC) of each of the bands. This leads to a definition of valence because the SI-corrected, localized, states are well separated from the valence states and are no longer available for bonding and band formation. In the SIC-LSD method, one calculates valence from first-principles, by comparing local energy minima corresponding to different valence scenarios composed of different numbers of localized and itinerant electrons. As mentioned earlier, this comparison establishes the nominal valence to be given by

$$N_{\mathrm{val}} = Z - N_{\mathrm{core}} - N_{\mathrm{SIC}},$$

with Z being the atomic number, N_{core} the total number of core (and semi-core) electrons, and N_{SIC} the number of localized, SI-corrected, states. Thus, in the SIC-LSD approach, these are the localized, SI-corrected, electrons that define the valence, and we shall come back to this point later.

It was postulated by Gschneidner (1971), more than 30 years ago, that there exist two types of f electrons in lanthanide materials, of which an integer number are atomic-like and a small, fractional number are band-like. Our *ab initio* approach confirms this dual character of f electrons, with the localized ones determining valence, and the itinerant ones, appearing at the Fermi level and hybridizing with the other, s, p, and d conduction electrons, being responsible for valence transitions, observed in many of the lanthanides systems. As, we shall discuss in the following, there exists a critical fractional number of these itinerant f electrons, above which, the solid will want to reduce its valence by localizing an additional electron. Such valence, and indeed also structural and magnetic, transitions can happen due to pressure or temperature.

4.2 Valence of elemental lanthanides

As already mentioned, in the SIC-LSD approach, one deals with the split f-manifold. The localized f electrons are responsible for establishing the ground state valence of the elements, based on the total energy considerations involving different valence configurations. In Figure 4, we show the total energy differences between the divalent and trivalent scenarios for all the lanthanide elemental solids, and their sulphides (which will be discussed in Section 4.3), as calculated within the SIC-LSD approach. As we are only interested in trends in valence across the lanthanide series, for simplicity, all calculations have been performed in the fcc structure, assuming in addition the ferromagnetic ordering of spins. The energy differences seen in Figure 4 are large and positive at the beginning of the lanthanide series, indicating preference for the trivalent state, but towards the middle of the series, they fall sharply, eventually becoming negative for Eu. This marks the change of valence to divalent state. From Eu to Gd, one observes a discontinuous jump due to the switch to a trivalent state at Gd, from where the

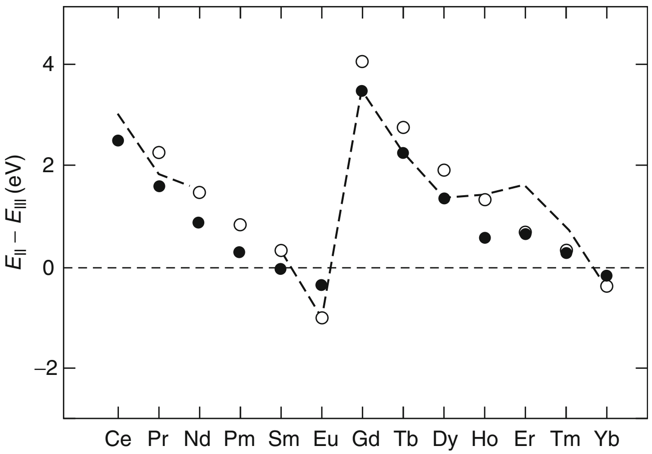

FIGURE 4 Total energy differences between divalent and trivalent elemental lanthanide metals (open circles) and their sulphides (solid circles). The dashed line shows the experimental values for the lanthanide metals. The calculated energy differences have been uniformly shifted upwards by 43 mRy to reproduce the valence transition pressure of 6 kbar in SmS. This rigid shift is sufficient to reproduce the correct valence states of the whole lanthanide metal series and their compounds.

behaviour of the energy differences repeats the one at the beginning of the series, until the arrival at Yb where a switch to divalence occurs.

To understand these anomalous changes in energies, in Figure 5, we show the corresponding energy differences as a function of the change in the number of itinerant f electrons across the lanthanide series, and also for the sulphides. One sees clearly the change from positive to negative values occurring when the number of itinerant electrons in the trivalent solid reaches the value of about 0.7, at which point, it is more favourable for the system to switch its valence to divalent. As observed above, these changes of valence happen for Eu and Yb, and these are precisely the elements for which one observes the dramatic jumps of lattice parameters now displayed in comparison with experiment in Figure 6. The agreement is very good and the anomalies are well reproduced. What we have learned from these *ab initio* SIC-LSDA calculations is that the dual character of the f electrons, postulated many years ago by Gschneidner (1971), can be understood from first principles and that both types of electrons play a different role in these systems. The localized electrons determine the valence and the magnetic and optical properties, whereas the valence transitions are driven by the itinerant f electrons. The latter are the conduction f electrons that hybridize strongly with the s, p, and d valence electrons, contributing to the DOS at the Fermi energy and establishing the Fermi surface. These itinerant f electrons exist only in the trivalent solids and, unlike the localized fs, they participate to bonding (Gschneidner, 1993).

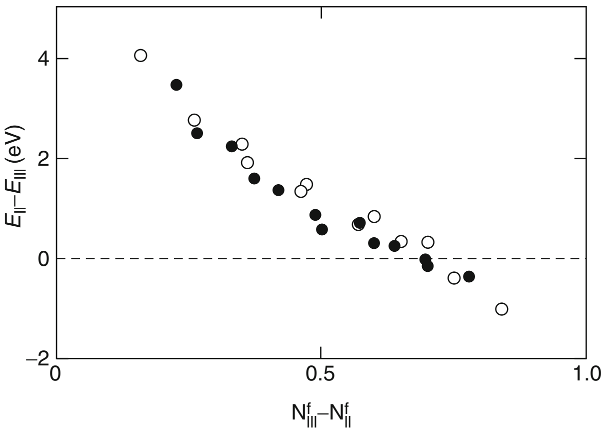

FIGURE 5 The energy differences between the divalent and trivalent valence states of the elemental lanthanides (open circles) and their sulphides (solid circles) versus the difference between the fractional numbers of itinerant f electrons in the two valence states.

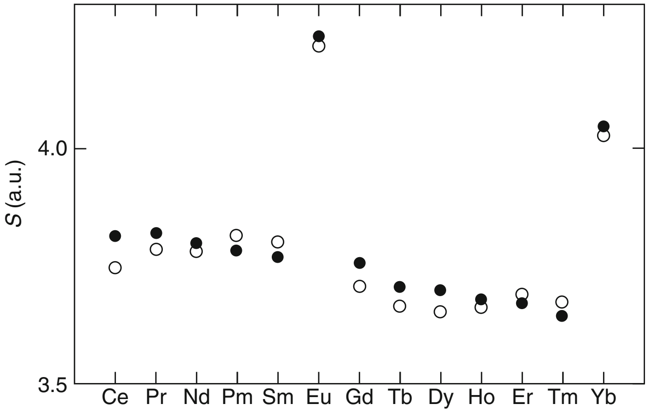

FIGURE 6 The calculated equilibrium atomic sphere radii, *S*, (open circles) and their experimental counterparts (solid circles) for all the lanthanide elements. The atomic sphere radius is defined in the caption of Figure 1.

4.3 Valence of pnictides and chalcogenides

At ambient conditions, the lanthanide monopnictides RX (X = N, P, As, Sb, Bi) and monochalcogenides RX (X = 0, S, Se, Te, Po) crystallize in the NaCl structure. Given the combination of an electropositive R-ion with an electronegative pnictide or chalcogenide, one might assume that an ionic picture can be applied here. But based on the observed properties, Rhyne and McGuire (1972) proposed a classification distinguishing between the so-called valence balanced compounds Pnictide^{3-}R^{3+}, Chalcogenide^{2-}R^{2+}, and valence unbalanced compounds such as

Chalcogenide^{2-}R^{3+} . The former being mostly ionic insulators, although there are exceptions, and the latter being mostly conductors.

The overall electronic properties of the lanthanide pnictides and chalcogenides are mainly determined by the f–f and f–d overlap between the corresponding orbitals on neighbouring lanthanide sites, and the f–p overlap between the lanthanide-sites and the pnictogen/chalcogen ion. While the f–f overlap in principle leads to narrow band formation, the corresponding small gain in energy has to compete with the strong intra-atomic correlations among the f-electrons that tend to localize them. As we will show, the difference between the valence balanced and valence unbalanced compounds is related to the competing trends of f-electron localization and f-band formation. In all our calculations, we assume the rock salt structure and ferromagnetic arrangement of spins. The reason is that the true magnetic structures of the lanthanide compounds are not always known.

4.3.1 The pnictides

The lanthanide pnictides have been studied extensively, given their potential applications. An overview of their electronic and magnetic properties has recently been written by Duan et al. (2007). An earlier review of the lanthanide pnictides can be found in Hulliger (1979). In this section, we shall mainly concentrate on the valencies of the lanthanide-ions, and the resulting electronic structure, as obtained within the SIC-LSD approach. In a simple ionic picture, one expects the pnictides to be trivalent insulators. The reason being that the pnictide ion, when alloyed with the lanthanide element, can accommodate additional three electrons through charge transfer and hybridization. The resulting trivalent lanthanide-ion configuration is confirmed by experiment and the present calculations. Many of these compounds, however, turn out not to be insulators.

Among the nitrides, only NdN, GdN, TbN, and DyN definitely order ferromagnetically, SmN is anti-ferromagnetic, and most of the remaining nitrides have not been investigated in sufficient detail for their magnetic structure to be unambiguously defined. The SIC-LSD study of the lanthanide–nitrides in the ferromagnetically ordered state finds all the compounds, from Pr onwards, to be trivalent in the ground state (Aerts et al., 2004). CeN is found to prefer, energetically, the tetravalent configuration. The calculated energy difference, $E_{\mathrm{II}}-E_{\mathrm{III}}$, between the divalent and trivalent configurations, is shown in Figure 7. As expected, the trend is towards a strongly trivalent state at the beginning of the series, and a decreasing energy difference as a function of filling up the f-shell up to Eu. Trivalent Gd is again very energetically favourable, given the half-filled f-shell, after which the energy trend repeats itself. The divalent configuration, however, does not become favourable for any of the nitrides. The calculated lattice parameters (Aerts et al., 2004) are compared to the experimental values (Wyckoff, 1968) in Figure 8. The jump between Ce and Pr is due to the valence change from tetravalent to trivalent. The overall agreement is very good, even though for some of the lighter lanthanides, the unexplained irregularities in the experimental data seem to reflect the relatively limited quality of the samples available at the time.

In Table 2, we show the spin-resolved band gaps and densities of states of each material at the Fermi energy. It is clear from the table that our SIC-LSD

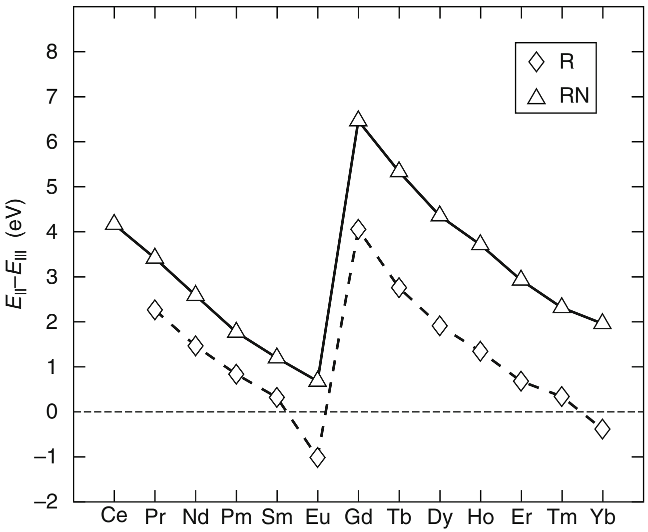

FIGURE 7 Total energy differences (in eV) between divalent and trivalent scenarios for lanthanide nitrides (triangles). The results for elemental lanthanides (diamonds) are repeated for an easy comparison (including 43 mRy correction, but not for the nitrides).

calculations find most of the light lanthanide nitrides to be half-metallic. Only CeN is metallic because it exists in the tetravalent state (in fact the trivalent state is also just metallic). TbN, DyN, and HoN are found to be narrow band gap insulators, and ErN, TmN, and YbN are metallic in both spin-channels, with the Fermi energy lying at the bottom of the spin-down 4f-states, leading to a rather large spin-down DOS at the Fermi energy. The insulating (semi-conducting), half-metallic, and full metallic behaviours that we have predicted for lanthanide nitrides is a consequence of the nitrogen p and the band-like lanthanide f-states occurring in the same energy window, in the vicinity of the Fermi level, which leads to strong hybridization of these states. Our results seem to suggest that lanthanide nitrides and their alloys may enable us to fabricate materials with a wide and continuous range of useful properties, particularly with regard to spin filtering applications where they may provide alternatives to the lanthanide chalcogenides already in use for this purpose (Moodera et al., 1993; Worledge and Geballe, 2000; Filip et al., 2002; LeClair et al., 2002).

The total and species-decomposed spin magnetic moments are displayed in Table 3. There we also present the lanthanide orbital moments. With the exceptions of ErN, TmN, and YbN, the spin magnetic moments of these materials take on an integer value. This indicates that these systems are either insulating (Tb-, Dy-, and Ho-nitrides) or half-metallic (Pr- to Gd-nitrides), since one needs at least one full band in one of the spin channels to obtain an integer value for the spin magnetic moment. CeN is a non-magnetic metal, and the last three compounds of the series are metallic in both spin-channels. These results are as one would expect; the spin magnetic moment is dominated by the rare earth f-electrons, with some hybridization yielding small contributions from the rare

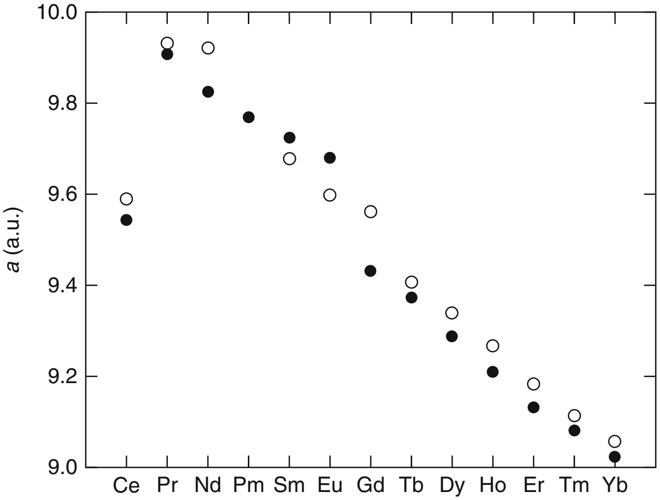

FIGURE 8 Lattice parameters of the lanthanide nitrides. The open circles are the experimental values, whereas the solid circles are the calculated lattice parameters.

TABLE 2 Spin-resolved band gaps (in Ry) and densities of states (in states/Rydberg/formula unit) at the Fermi energy for the lanthanide nitrides

	Band gap		DOS	
Material	Spin up	Spin down	Spin up	Spin down
CeN	0	0	15.37	15.37
PrN	0	0.039	0.0001	0
NdN	0	0.065	0.068	0
PmN	0	0.076	31.77	0
SmN	0	0.095	154.56	0
EuN	0	0.107	69.85	0
GdN	0	0.082	0.065	0
TbN	0.008	0.052	0	0
DyN	0.018	0.058	0	0
HoN	0.031	0.004	0	0
ErN	0	0	0.682	69.57
TmN	0	0	1.52	220.78
YbN	0	0	1.72	93.18

TABLE 3 Total and species-decomposed spin magnetic moments (M_S) of the rare earth nitrides. All values are in Bohr magnetons (μ_B). The contribution of the empty spheres to the total spin magnetic moments is not shown. Because of these empty spheres that were introduced in the unit cell to increase the accuracy of the calculation, the sum of the *R* and *N* spin magnetic contributions does not give the total spin magnetic moment. The lanthanide orbital moment (M_L) assumes that the lanthanide ions obey Hund's rules

	M_S			M_L
Material	*R*	*N*	Total	*R*
CeN	0.0	0.0	0.0	0.0
PrN	2.07	−0.08	2.00	−5.0
NdN	3.10	−0.11	3.00	−6.0
PmN	4.13	−0.14	4.00	−6.0
SmN	5.22	−0.24	5.00	−5.0
EuN	6.30	−0.30	6.00	−3.0
GdN	7.01	−0.04	7.00	−0.0
TbN	5.97	0.01	6.00	3.0
DyN	4.93	0.05	5.00	5.0
HoN	3.91	0.08	4.00	6.0
ErN	2.90	0.09	2.99	6.0
TmN	1.83	0.12	1.96	5.0
YbN	0.79	0.14	0.94	3.0

earth s-d electrons and the nitrogen p-states. This indicates that the nitrogen p-states occur in the same energy range as the valence rare earth states, allowing hybridization to occur. It is interesting to note that the contribution from the nitrogen atom to the spin moment changes sign half way through the series and becomes parallel to the lanthanide's spin moment. It appears that the nitrogen moment wants to point anti-parallel to the partially occupied majority f-spin channel.

With respect to the trends in the RX series as a function of pnictide X (X = N, P, As, Sb, Bi), a number of SIC-LSD investigations have been published, respectively for CeX (Svane et al., 1996, 1998), PrX (Vaitheeswaran et al., 2004), SmX (Svane et al., 2005), EuX (Horne et al., 2004), and YbX (Temmerman et al., 1999). Generally, it has been found that the tendency towards trivalence decreases with increasing anion size, that is from N to Bi. The larger pnictide ions push the lanthanide-ions further apart, thus decreasing the mutual f–f and f–d overlaps. As a consequence, band formation becomes less favourable as the lanthanide size increases, resulting in less gain of band formation energy, and the gain in SIC-localization energy becoming relatively more important. Eventually, as is the case with the late Eu-pnictides and Yb-pnictides, the SIC-energy becomes the more important energy scale, localizing an additional electron in the divalent ground state configuration.

In Figure 9A, the band structure for PrSb is shown. Here Pr is assumed to be in its trivalent ground state configuration. The lowest lying bands, around –0.6 Ry relative to the Fermi level, are mainly due to the Sb s-state, which is well separated from the remaining valence bands. Just below the Fermi level, we find the Sb p-band that is highly hybridized with Pr s- and d-states. The cluster of bands situated at 0.02–0.2 Ry above the Fermi level is due to the itinerant f-states of Pr. The two localized Pr f-states are not shown in the figure. PrSb remains metallic as hole pockets in the vicinity of the Γ-point compensate electron pockets around the X points. The major contribution to the DOS at the Fermi level comes from the d-states of Pr and the p-states of Sb. As can be seen from Figure 9B, the resulting DOS at the Fermi level is rather low, which makes PrSb a semi-metal, in agreement with results from an LDA + *U* calculation (Ghosh et al., 2003). With respect to the f-bands, we notice some hybridization with the spd-band, but the main part is bundled in the two large, exchange split peaks above the Fermi level.

For a given pnictogen, as we move through the lanthanide series, the lanthanide contraction results in increased localization of the f-electrons that, as we have seen for the RN compounds in Figure 7, results in a decreasing $E_{\mathrm{II}}-E_{\mathrm{III}}$. The

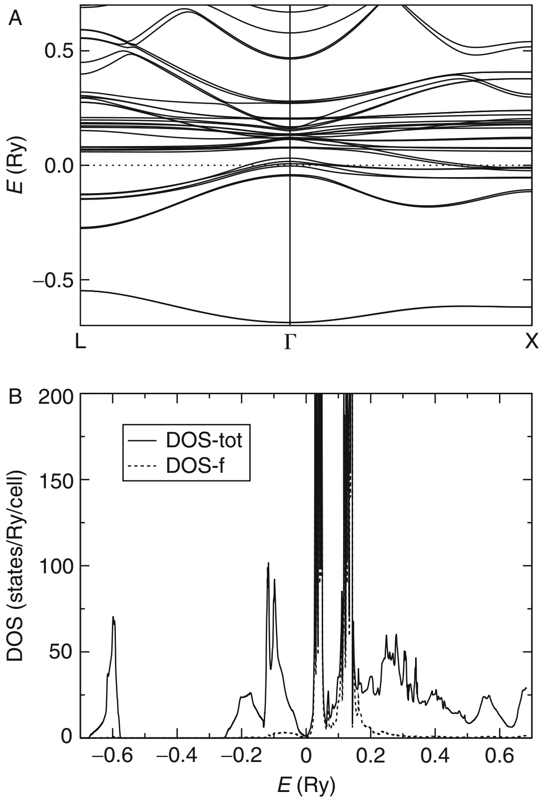

FIGURE 9 Band structure (A) and DOS (B) of trivalent PrSb. In (A), the dotted line marks the Fermi level. In (B), the energy (in Ry relative to the Fermi level) is plotted along the *x*-axis and the DOS (in units of states Ry^{-1} per formula unit) along the *y*-axis. The full curve is the total DOS whereas the dotted curve gives the itinerant Pr f partial DOS. The SIC localized states are not shown.

increasing trend towards localization also means that the corresponding f-state energy levels move towards lower energies, that is they move closer to the pnictogen p-band. This can be observed, for example, in the previously described PrSb DOS depicted in Figure 9B, as compared with the DOS of SmAs shown in Figure 10. In the latter, we find two narrow Sm f resonances situated just above the Fermi level. With increasing localization of the lanthanide ion f-electrons, the itinerant f-peak gets pinned to the Fermi level, and as they move to lower energies, they start filling up with valence electrons. It was shown earlier that the degree of populating the delocalized narrow f-peak is correlated with $E_{\mathrm{II}}-E_{\mathrm{III}}$, in the sense that the SIC energy is related to the occupied f-states and becomes increasingly important as the f-peak is being occupied, eventually preferring to localize. Thus, the increased occupancy of the f-peak explains the observed trend in valence as a function of lanthanide ion.

Parallel to the observed trend towards filling up the f-peak as a function of the lanthanide ion, one also observes increased occupancy for a given lanthanide as one moves through the pnictide series from N to Bi. Again this can be correlated to the corresponding $E_{\mathrm{II}}-E_{\mathrm{III}}$. In the Sm pnictides, for example, the preference for a trivalent ground state configuration is reduced from 135 mRy per formula unit in SmN to only 6 mRy per formula unit in SmBi (Svane et al., 2005). This trend is explained by the fact that with decreasing electronegativity, the p-bands move up in energy, which results in the Fermi energy moving progressively into the f-peak when going from N to Bi. As this happens, the pnictide p-bands are intersected at the top by the narrow f-band which pins the Fermi level.

The two trends of f-peak moving towards lower energies with increasing f-electron localization, and of the p-band moving towards higher energies with decreasing electronegativity, culminate for the Eu pnictides and Yb pnictides, and the resulting large degree of occupancy of the f-peak means that the gain in

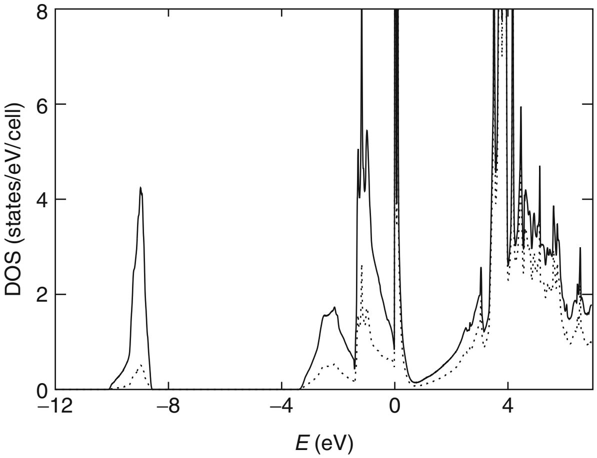

FIGURE 10 DOS with respect to the Fermi energy of trivalent SmAs. The full line shows the total DOS and the dotted line shows the Sm contribution. The SIC localized states are not shown.

SIC-energy becomes large enough to overcome the loss in band formation energy. Thus, from the calculated $E_{\mathrm{II}}-E_{\mathrm{III}}$, we observe that this energy difference eventually turns marginally positive or even negative for the later Eu pnictides, EuAs, EuSb, and EuBi, and YbBi. These findings are in good agreement with experiment, where it turns out that neither of the latter compounds exists in the NaCl structure (Iandelli and Franceschi, 1973), and one might speculate that this is due to the fact that the trivalent configuration is no longer stable in these compounds. Thus, EuAs adopts the hexagonal Na_2O_2 crystal structure (Ono et al., 1971; Wang et al., 1977), that is a distortion of the NiAs structure due to the formation of anion–anion pairs. In conclusion, although the large majority of the lanthanide pnictides prefer the trivalent ground state configuration, the trend towards trivalence decreases with cation size from Ce to Eu, and again from Gd to Yb, as well as with anion size from N to Bi. In the Eu series, the N and P are still sufficiently electronegative to support the charge transfer of three electrons resulting in Eu^{3+} ions, but starting with EuAs, seven f-electrons remain localized at the Eu site, and an eventual NaCl structure, with divalent Eu ions, is unstable to structural transition towards the Na_2O_2 crystal structure.

4.3.2 The chalcogenides

In many respects, the chalcogenides are similar to the pnictides, crystallizing in the same NaCl structure and with the s-, p-, and d-states situated at the same energy ranges as their corresponding neighbours to the left in the Periodic Table. Nevertheless, with respect to the electronic structure, they differ dramatically from each other, which can be traced to the fact that with one additional p-electron, there is only space for accommodating two additional electrons in the valence band, through charge transfer and hybridization. As a consequence, an eventual trivalent ground state is forced to accommodate the third electron in the narrow f-peak, which results in many more compounds being situated at the boundary of the trivalent–divalent phase transition. A divalent ground state configuration is in agreement with the ionic picture for chalcogenides.

Calculations with the SIC-LSD method of the lanthanide-sulphides (Strange et al., 1999) have shown that divalence already sets in here, although only with respect to the lanthanide ions Sm, Eu, and Yb, as can be seen from Figure 11. At the beginning of the lanthanide series, the empty f-levels are held well above the Fermi level, and the third electron is accommodated in the states at the bottom of the broad sd-band. As the atomic number increases, the f-levels move closer to the Fermi level and start picking up electrons. As we reach SmS, the state immediately above the Fermi level is almost entirely of f character, and the electrons now filling up the narrow peak prefer to localize, resulting in a divalent ground state. This behaviour occurs in the light lanthanide from CeS to EuS, and is repeated in the heavy lanthanide from GdS to YbS.

For the lanthanide chalcogenides, it was demonstrated experimentally that Sm, Eu, and Yb are divalent in their sulphide, selenide, and telluride compounds, while Tm becomes divalent for the telluride phase only (Jayaraman, 1978, 1979). The SIC-LSD calculations find all the Eu chalcogenides, including EuO, to be insulators in the ferromagnetic state, and to have a divalent configuration

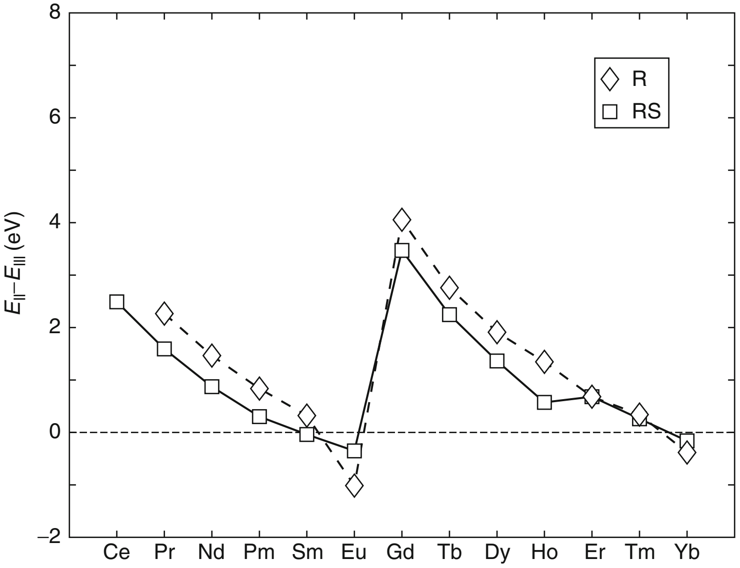

FIGURE 11 Total energy differences (in eV) between divalent and trivalent scenarios for lanthanide sulphides (squares). The results for elemental lanthanides (diamonds) are repeated for an easy comparison (including 43 mRy correction also applied to sulphides).

(Horne et al., 2004). For the Yb chalcogenides, the divalent state is seen to be favoured in all cases by 35–70 mRy (Svane et al., 2000). Both of these results are thus in good agreement with experiment. With respect to the Sm chalcogenides already in Sm monoxide, the divalent f^6 configuration is found to be energetically most favourable, by 6 mRy, and in SmS by 15 mRy (Svane et al., 2005). Hence, the SIC-LSD predicts a Sm valence transition between the pnictides and chalcogenides, as shown in Figure 12. This is not in complete agreement with the experimental picture, according to which the divalent and trivalent ground states in SmS are almost degenerate, while Sm in SmO is trivalent and metallic (Krill et al., 1980; Leger et al., 1980). Thus, it appears that the SIC-LSD functional overestimates the tendency for divalence by approximately 15 mRy in SmS. Assuming this error to be similar for all SmX compounds, this would imply that the calculated energy balance curve in Figure 12 lies too high by approximately 15 mRy. In Figure 12, we therefore include a calibrated energy curve (dashed line) when 15 mRy correction is subtracted from the calculated trivalent-divalent energy difference. In the paper by Strange et al. (1999), a similar uniform calibration of 43 mRy (this uniform energy shift is already included in Figure 11) was applied to the trivalent-divalent energy difference of the lanthanide sulphides in order to account for the experimentally observed valence of SmS. The different size of the calibrating energy shift can to a large extent be traced to the neglect of spin-orbit coupling in the former work of Strange et al. (1999).

In the Tm chalcogenides, the calculated energy differences between divalent f^{13} and trivalent f^{12} are found to be −1.2, −13.5, −24.3, and −37.3 mRy for TmS,

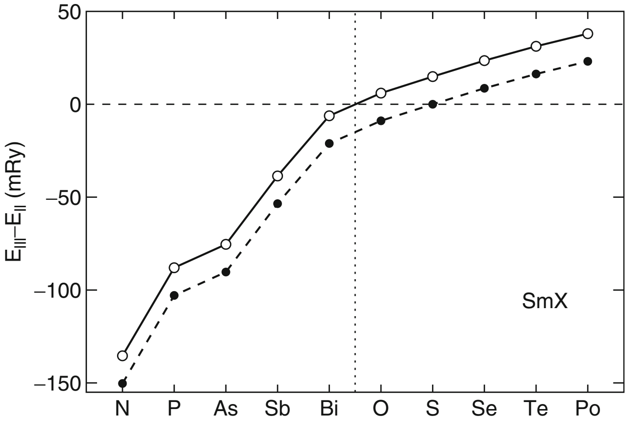

FIGURE 12 Total energy differences (in mRy) between divalent and trivalent scenarios for SmX (full line). A negative sign implies that the trivalent state is favoured. The dashed line marks a 15 mRy corrected energy curve: this is the amount by which the SIC-LSD (with spin-orbit included) overestimates the tendency to form the divalent configuration.

TmSe, TmTe, and TmPo, respectively, reflecting the trend towards greater localization with the larger ligand. Also here, it turns out that at ambient pressure, the trend towards localization is overestimated by some 15 mRy, as it is found experimentally that TmS is a trivalent metal and TmSe is in a mixed valent state.

4.4 Valence of ytterbium compounds

Ytterbium compounds show a wealth of anomalous physical phenomena caused by the intricate electronic structure related to its f-electrons (Cho et al., 1993; Wachter, 1993; Joyce et al., 1996). In the atomic ground state, Yb is divalent with a filled f^{14} shell, but in the solid state, the f-electrons may play an active role in the bonding giving rise to intermediate valent, heavy-fermion, or Kondo behaviour as well as complex magnetic structures. In Temmerman et al. (1999) and Svane et al. (2000), a number of Yb compounds were investigated with the SIC-LSD approach and the energetics of the valence of Yb ions was calculated. The divalent configuration is realized by applying SIC to all 14 f-electrons, while the nominally trivalent configuration is realized by applying SIC to 13 of 14 f-electrons. In this latter case, the last f-electron is allowed to hybridize with the normal sd conduction electrons and form band states. The effective Yb valence, which is given as the number of non-f valence electrons, is then determined by the degree of occupancy of these f-band states, and the resulting electronic structure may be viewed as a realization of an intermediate valence state. The highest effective valence found in this study is 2.88 (for YbN), that is, in no case is the ideal trivalent state reached. The results are summarized in Figure 13 that shows the energy difference between the two localization scenarios correlated with the degree of filling of the f-band in the nominally trivalent scenario.

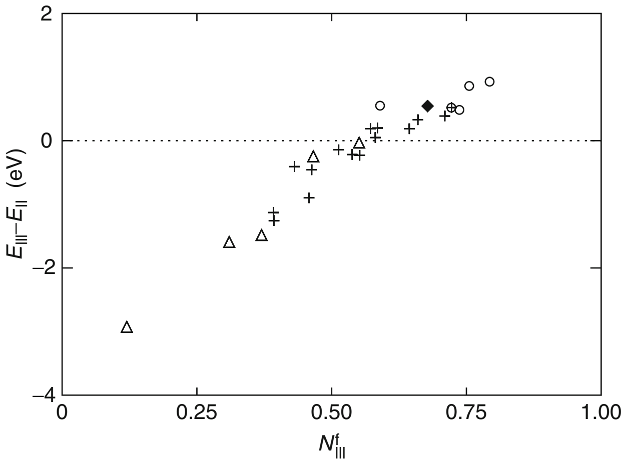

FIGURE 13 Energy difference between the configurations with 13 and 14 localized f-electrons, $\Delta E = E(f^{13}) - E(f^{14})$, correlated with the degree of filling of the 14th Yb f-band in the f^{13} configuration, N_f, for a sequence of Yb compounds. Triangles correspond to the mononitrides, in order of increasing N_f: YbN, YbP, YbAs, YbSb, and YbBi. Circles correspond to the monochalcogenides, in order of increasing N_f: YbO, YbS, YbSe, YbTe, and YbPo. Crosses correspond to the ytterbium intermetallics, in order of increasing N_f: $YbAl_3$, YbRu, YbIr, $YbPd_3$, YbRh, YbPd, $YbAl_2$, YbBiPt, YbZn, YbAu, YbAg, YbCd, Yb_3Pd, $YbPb_3$, and YbIn. Finally, the diamond denotes elemental fcc Yb.

The Yb compounds considered may be divided into three groups, according to the size and sign of the energy difference between the f^{14} and f^{13} localization scenarios. The group of strongly trivalent compounds comprises the monopnictides YbN, YbP, YbAs, and the intermetallics YbRu, YbRh, YbIr, $YbAl_3$, and $YbPd_3$. For this group, the f^{13} configuration is favourable over the f^{14} configuration by more than 0.25 eV per Yb atom. The effective valence ranges from 2.88 in YbN to 2.54 in YbRh and $YbPd_3$.

The second group consists of the strongly divalent Yb compounds, encompassing all the monochalcogenides YbO, YbS, YbSe, YbTe, and YbPo, as well as elemental Yb, Yb_3Pd, $YbPb_3$, and YbIn. Here the divalent Yb configuration is favoured over the nominally trivalent configuration by more than 0.25 eV. The effective valence is 2 for these compounds.

The remaining compounds are characterized by having the calculated energies of the f^{13} and f^{14} Yb configurations equal within 0.25 eV. Therefore, effects of valence fluctuations may start to be important. It has been found, however, that the weakly divalent compounds, the intermetallics YbCd, YbZn, YbAg, and YbAu, are in fact well described by the f^{14} localized configuration, as evidenced by the agreement between the calculated and experimental volumes (Svane et al., 2000). Hence, for these compounds, there seems to be no need for additional cohesive contribution originating from valence fluctuations. Interesting behaviour may be expected when pressure is applied to these materials since the effects of valence fluctuations will then become more pronounced. Unfortunately, no pressure experiments have been reported on any of the Yb compounds in this group. Finally, the compounds YbSb, YbBi, YbBiPt, YbPd, and $YbAl_2$ are weakly trivalent, that is according to the calculations, the f^{13} localization scenario is favoured by less than 0.25 eV. Among these, YbBiPt and $YbAl_2$ are known to be heavy-fermion compounds (Havinga et al., 1973; Robinson et al., 1994), and YbPd is believed to be a mixed valent system, with approximately equal proportions of Yb^{2+} and Yb^{3+} ions (Iandelli et al., 1980; Bonville et al., 1986). YbBi has never been synthesized, while YbSb in most respects resembles the other predominantly trivalent Yb pnictides, however, with somewhat unusual low-temperature magnetic behaviour (Kasuya, 1994; Oyamada et al., 1994; Li et al., 1995). Hence, for the compounds in this group, the valence fluctuation phenomena seem to be significant. The calculated effective valencies range from 2.53 in YbSb to 2.45 in YbBi and YbBiPt, that is, the band states of the 14th f-electron are approximately half-filled. The heavy-fermion character of YbBiPt is also confirmed by LDA + U calculations (Oppeneer et al., 1997).

In conclusion, the valence classification of Yb compounds, based on the SIC-LSD total energies, maps very well onto the physical properties observed experimentally. In particular, this allows to identify the third group of compounds as the heavy-fermion and mixed-valent systems on the trivalent side, and, on the divalent side, those systems that are likely to undergo pressure-induced valence transitions.

At ambient conditions, the Yb monopnictides and monochalcogenides crystallize in the B1 structure. As outlined, the Yb pnictides are all found to be well described by the nominally trivalent scenario, where the effective valence varies from 2.88 in YbN to 2.69, 2.63, and 2.53 in YbP, YbAs, and YbSb, respectively. Experimentally, the position of the f^{14} band is found ~0.2 eV above the Fermi level in YbN, YbP, and YbAs (Degiorgi et al., 1990, 1993). Other experiments have revealed heavy-electron behaviour in Yb pnictides (Ott et al., 1985; Sakon et al., 1992; Takeda et al., 1993), but this can be a reflection of sample non-stoichiometry (Degiorgi et al., 1990, 1993). The discrepancy between the present electronic structure and the picture provided by Degiorgi et al. (1990, 1993) can be due to the LSD approximation, since the position of the narrow f^{14} band in the theory is solely determined by the LSD potential (no correlation correction). LDA + U calculations on YbN (Larson et al., 2007) include a positive correlation shift of the unoccupied f-states that leads to an ideal trivalent Yb ion in accordance with Degiorgi et al. (1990, 1993).

In contrast to the pnictides, the equilibrium volumes of the Yb chalcogenides are accurately described assuming the divalent f^{14} configuration for Yb. As pressure is applied to the Yb chalcogenides, the f^{13} configuration becomes more and more favourable, and eventually a transition to an intermediate valence state occurs. Valence transitions in lanthanide systems will be discussed in the next section.

4.5 Valence transitions

When pressure is applied to lanthanide systems, the interaction of the electrons generally increases and at some point, it becomes advantageous for the f-electrons to contribute more actively to the bonding, that is the effective valence increases.

In the SIC-LSD formalism, this happens when localization scenarios of different f^n configurations become close in energy. In the present $T = 0$ K theory, only discontinuous pressure-induced transitions can be described, while experiments often, but not always, observe continuous transitions, signalled by anomalous softening of the pV-curve.

Tables 4 and 5 summarize results for valence transitions in the cerium and praseodymium pnictides (Svane et al., 1996, 1998; Vaitheeswaran et al., 2004) and selected rare earth chalcogenides (Svane et al., 1998, 1999, 2001, 2004; Vaitheeswaran et al., 2004; Lebegue et al., 2005; Svane et al., 2005). In Figure 14 is shown the total energy of CeP as calculated with SIC-LSD considering both the B1 (rocksalt) and B2 (caesium chloride) crystal structures as well as both the itinerant, f^0, and the localized, f^1, scenario for the Ce ions (Svane et al., 1996). The lowest energy is found in the B1 phase with localized f-electrons and with a specific volume of 348 a_0^3 per formula unit, which coincides with the experimental equilibrium volume. The B1 phase with delocalized f-electrons has its minimum at a considerably lower volume, due to the significant f-electron band formation energy providing a large negative component to the pressure. From the common tangent, a phase transition is predicted at a pressure of 7.1 GPa with a volume collapse of $\Delta V/V_0 = 8\%$ (change in volume relative to the zero pressure equilibrium volume), which is in excellent agreement with the transition observed at 5.5 GPa (Mori et al., 1993). The B2 structure is not as favourable for the CeP compound since the calculated energy is substantially higher than that of the B1 structure. This holds for both localized and delocalized f-electrons. From Figure 14, we conclude that the B2 structure with localized f-electrons is never reached in CeP, while at high pressure, a second phase transition to the B2 structure with delocalized f-electrons is found. The transition pressure is calculated to be 11.3 GPa and the volume collapse 12%, while experimentally, the B1 $\rightarrow$ B2 phase transition is seen at 15 ± 4 GPa (Vedel et al., 1987). The experimental volume collapse is 11%.

The results reported in Table 4 show that all of the observed pressure transitions in the cerium pnictides and chalcogenides are indeed reproduced (Svane et al., 1998). In all cases except CeN is the localized f^1 configuration favoured in the ground state. The total energy curves look rather similar to those of CeP in Figure 14, but minor changes in the relative positions occur when the ligand is varied. The localized phases are generally more favoured when the ligand ion becomes heavier, and as a consequence, in CeAs, no isostructural delocalization transition occurs in the B1 structure. Instead, a transition directly from the B1 structure with localized f-electrons to the B2 structure with delocalized f-electrons occurs, in agreement with experiment. In CeSb and CeBi, the first high-pressure transition to occur is from B1 to B2, with localized f-electrons in both cases, and only at higher pressures is a delocalization transition predicted to take place. The calculated transition pressures for these delocalization processes are only slightly above the ranges studied experimentally. In this work, only the B2 structure was considered for the second transition, but in reality, the valence transition which eventually must take place in CeSb and CeBi may involve another unknown high pressure phase.

TABLE 4 Calculated transition pressures for the electronic and structural phase transitions in the Ce pnictides and chalcogenides. Also quoted are the volume discontinuities (relatively to the zero pressure equilibrium volume) at the transition. The notation (f^n) refers to SIC-LSD calculations with n localized f-electrons. For the cerium pnictides, B2* denotes the distorted B2 structure. Experimentally, the transitions of the Ce pnictides are discontinuous, while those of the cerium chalcogenides (at room temperature) are continuous

		P_t (GPa)		Volume collapse (%)	
Compound	Transition	Theoretical	Experimental	Theoretical	Experimental
CeN	$B1(f^0)\rightarrow B2(f^0)$	62.0	–	3.6	–
CeP	$B1(f^1)\rightarrow B1(f^0)$	7.1	9.0[a],5.5[b]	8.0	4[a]
CeP	$B1(f^0)\rightarrow B2(f^0)$	11.3	15(4)[a],25.0[j]	12.1	11[a]
CeAs	$B1(f^1)\rightarrow B2(f^0)$	11.4	14(2)[c],21.0[j]	18.0	11[c]
CeSb	$B1(f^1)\rightarrow B2^*(f^1)$	7.0	8.5(2.5)[d],15[j]	10.9	10[d]
CeSb	$B2^*(f^1)\rightarrow B2^*(f^0)$	25.2	–	3.7	–
CeBi	$B1(f^1)\rightarrow B2^*(f^1)$	8.8	9(4)[e]	10.8	9[e]
CeBi	$B2^*(f^1)\rightarrow B2^*(f^0)$	37.0	–	2.8	–
CeS	$B1(f^1)\rightarrow B1(f^0)$	10.1	–[f],12.5(1.5)[g]	6.3	5[g]
CeS	$B1(f^0)\rightarrow B2(f^1)$	24.3	–	4.6	–
CeS	$B2(f^1)\rightarrow B2(f^0)$	29.5	–	3.6	–
CeSe	$B1(f^1)\rightarrow B2(f^1)$	12.4	17(3)[h]	11.1	9[h]
CeSe	$B2(f^1)\rightarrow B2(f^0)$	37.7	–	3.1	–
CeTe	$B1(f^1)\rightarrow B2(f^1)$	74.0	5.5(2.5)[i]	11.7	9[i]
CeTe	$B2(f^1)\rightarrow B2(f^0)$	43.5	–	2.4	–

[a] Vedel et al. (1987); [b] Mori et al. (1993); [c] Werner et al. (1983); [d] Léger et al. (1984); [e] Léger et al. (1985); [f] Léger (1993); [g] Croft and Jayaraman (1980); [h] Léger and Redon (1989); [i] Léger et al. (1983).

In CeS, the first transition occurs to the B1 phase with delocalized f-electrons (Svane et al., 1999), that is, the theory predicts an isostructural phase transition in CeS similar to CeP. The calculated transition pressure is 10.1 GPa with a volume collapse of 6%. These findings are in excellent agreement with the experiment of Croft and Jayaraman (1980), but at variance with the results of Vedel et al. (1986), who observe a soft anomaly in the pV-curve but no discontinuity. These results may indicate the proximity of a critical point. At higher pressures, CeS transforms into the B2 phase. According to the present calculations, this occurs in two steps. First, at a pressure of 24.3 GPa, CeS goes into the trivalent B2 phase with a 4.6% volume change. In the second step, at a pressure of 29.5 GPa, the tetravalent B2 phase is reached with a 3.6% volume collapse (Svane et al., 1999). Unfortunately, no experiments have been performed beyond 25 GPa (Léger, 1993).

In both CeSe and CeTe, the only pressure transition observed is that from B1 to B2 with localized f-electrons in both phases. These are also first to occur according to the calculations, whereas valence transitions are predicted in the range of 40 GPa. Thus, the situation here is quite similar to that in CeSb and CeBi, apart from the tetragonal distortion in these compounds that was not found for CeSe and

TABLE 5 Calculated transition pressures for the electronic and structural phase transitions in the Pr pnictides and chalcogenides of Pr, Sm, Eu, Tm, and Yb. Also quoted are the volume discontinuities (relatively to the zero pressure equilibrium volume) at the transition. The notation (f^n) refers to SIC-LSD calculations with *n* localized f-electrons. Experimentally, the transitions of SmS are discontinuous, while those of SmSe, SmTe, EuO, EuS, and the Tm and Yb chalcogenides (at room temperature) are continuous. The volume changes for SmSe and SmTe as well as TmTe are obtained by extrapolation over the transition range. For Yb compounds, we quote the relative volumes at which the delocalization starts

		P_t (GPa)		Volume collapse (%)	
Compound	Transition	Theoretical	Experimental	Theoretical	Experimental
PrP	$B1(f^2)\rightarrow B2(f^2)$	16.0	26[a]	11.4	–
PrAs	$B1(f^2)\rightarrow B2(f^2)$	12.0	27[a]	12.4	18.4[a]
PrSb	$B1(f^2)\rightarrow B2(f^2)$	8.0	13[a]	11.7	10.0[a]
PrBi	$B1(f^2)\rightarrow B2(f^2)$	8.0	14[a]	10.9	9.0[a]
PrS	$B1(f^2)\rightarrow B2(f^2)$	22.0	–	8.0	–
PrSe	$B1(f^2)\rightarrow B2(f^2)$	12.0	–	9.3	–
PrTe	$B1(f^2)\rightarrow B2(f^2)$	5.0	9	11.7	–
SmS	$B1(f^6)\rightarrow B1(f^5)$	0.1	0.65[b] 1.24[c]	11.1	13.5[b], 13.8[c]
SmSe	$B1(f^6)\rightarrow B1(f^5)$	3.3	∼4[b], 3.4[c], 3–9[d], 2.6–4[e]	9.8	8[b], 11[d], 7[e]
SmTe	$B1(f^6)\rightarrow B1(f^5)$	6.2	2–8[b], 5.2[c], 6–8[d], 4.6–7.5[e]	8.4	9[d],7[e]
EuO	$B1(f^7)\rightarrow B1(f^6)$	19.3	30[f], 13–30[g]	6.3	5[f]
EuS	$B1(f^7)\rightarrow B1(f^6)$	11.6	16[h]	5.7	0[h]
TmSe	$B1(f^{13})\rightarrow B1(f^{13})$	0	0–5[k]	14	8[k]
TmTe	$B1(f^{13})\rightarrow B1(f^{13})$	3.0	2–5[k]	15	14[k]
TmPo	$B1(f^{13})\rightarrow B1(f^{13})$	8.0	–	–	–
YbO	$B1(f^{14})\rightarrow B1(f^{13})$	18.0	8[i]	0.87	0.95[i]
YbS	$B1(f^{14})\rightarrow B1(f^{13})$	7.5	10[j]	0.93	0.88[j]
YbSe	$B1(f^{14})\rightarrow B1(f^{13})$	16.0	15[f]	0.79	0.75[f]
YbTe	$B1(f^{14})\rightarrow B1(f^{13})$	24.0	15[f]	0.78	0.65[f]

[a] Shirotani et al. (2003); [b] Benedict and Holzapfel (1993); [c] Insulator-metal transition of Sidorov et al. (1989); [d] Present author's estimates from figures of Bihan et al. (1995) and [e] Tsiok et al. (1991); [f] Jayaraman et al. (1974); [g] Zimmer et al. (1984); [h] Insulator-metal transition, Syassen (1986). [i] Werner et al. (1981); [j] Syassen (1986). [k] Debray et al. (1982).

CeTe. The B1 → B2 transition in cerium chalcogenides has also been investigated within the GGA approach (Bouhemadou et al., 2005), in which case, the f electrons are treated as itinerant.

The SIC-LSD studies on the Pr chalcogenides and pnictides show that the ground state favours the B1 structure over the B2 structure throughout the entire series. With applied pressure, all these compounds undergo a transition to the B2 CsCl structure (or a distorted version of it). For the Pr pnictides, the calculated transition pressures agree quite well with experiment, although they are

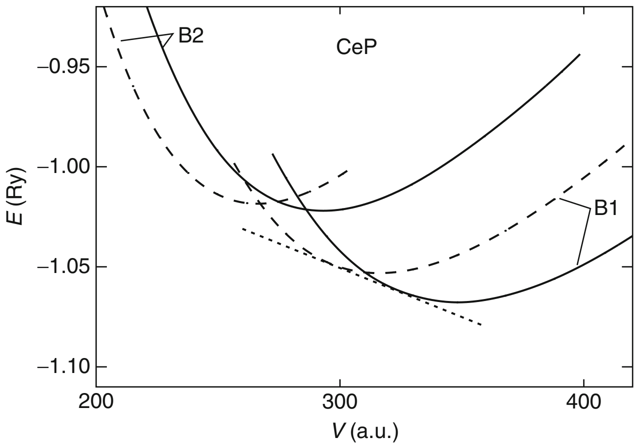

FIGURE 14 Cohesive energy of CeP (in Ry/formula unit) as a function of specific volume (in a_0^3/formula unit). Two crystal structures, the B1 and B2, are considered, and each with two different treatments of the Ce f-electrons. The full drawn curves correspond to calculations with one localized f-electron per Ce atom, whereas the dashed curves correspond to itinerant f-electrons. The dotted line marks the common tangent at the isostructural phase transition in the B1 structure.

systematically lower, as can be seen from Table 5. The agreement with experiment is equally good for PrTe, while the values for PrS and PrSe have not yet been measured experimentally. Unlike in the case for the Ce pnictides and chalcogenides, the trivalent Pr configuration remains stable under pressure up to 50 GPa.

At ambient pressure, the Sm ions in samarium chalcogenides are divalent, f^6, but the trivalent phase becomes relevant at high pressure. In this phase, the localized f^5 Sm ions coexist with a partly occupied narrow f-band, effectively describing an intermediate valent phase (Svane et al., 2005). The calculated and measured transition pressures are listed in Table 4. The good agreement both for transition pressures and for volume collapses shows that the bonding of the high-pressure phase is well described in the SIC-LSD approximation, even if the true many-body wavefunction of the intermediate valence phase is much more complicated than the corresponding SIC-LSD wavefunction. This is in line with the general philosophy of the density functional approach in obtaining good total energy estimates from simple reference systems (non-interacting electrons). The present theory cannot describe the continuous nature of the transition observed for SmSe and SmTe. The experiments were all conducted at room temperature and it would be interesting to investigate whether the continuous transition would exist at low temperature as well.

The calculated valence transition pressures for EuO and EuS in the B1 structure are compared with experiment in Table 5. Experimentally, the transition of EuO (at room temperature) is continuous, as in SmSe and SmTe. For EuS, the experiments show no anomalous compression curve (Jayaraman et al., 1974), but the band gap closes at 16 GPa, just before the structural transition to the B2 structure occurs (at 20 GPa) (Syassen, 1986). Due to the ASA in the LMTO-ASA band structure method, significant uncertainty exists in the comparison of the total energy between different crystal structures. Also the spin-orbit interaction can significantly alter the results: we found that without spin-orbit, the structural transition occurs at 13.7 GPa (Svane et al., 2001), however, without an isostructural transition occurring first.

For TmSe and TmTe, one observes continuous isostructural (B1 → B1) valence transitions over a wide volume range, for TmSe already starting at ambient conditions. The calculated discontinuous volume changes are in good agreement with the experimental volumes.

For Yb chalcogenides, the application of pressure leads to a pronounced softening of the pV-curve (Jayaraman et al., 1974; Werner et al., 1981; Syassen, 1986). This softening is found to be correlated with the closure of the f → d energy band gap, that is, it starts as the f^{14} shell becomes unstable. In Figure 15, the experimental pV-curve (Syassen, 1986) of YbS is compared with the theoretical curves, obtained with SIC-LSD for the two valence scenarios f^{13} and f^{14} (Temmerman et al., 1999). At pressures below 10 GPa, the experimental and theoretical (14 localized f-electrons) curves coincide. Above 10 GPa, the experimental curve is clearly anomalous, indicating valence instability (Syassen, 1986). The theoretical transition pressure is found to be $P_t \sim 7.5$ GPa, in good agreement with the observed onset of anomalous behaviour around ~10 GPa.

In Table 5, the calculated and available experimental data are collected for the isostructural pressure transitions in Yb chalcogenides. The general trends are reproduced by the calculations. Only for the case of YbO, the calculated transition pressure seems to be significantly too high. In the intermetallic $YbAl_3$ compound, pressure induces a continuous increase of valence (Kumar et al., 2008), which is in good agreement with the calculated rate of depletion of the 14th f-band in the SIC-LSD calculations.

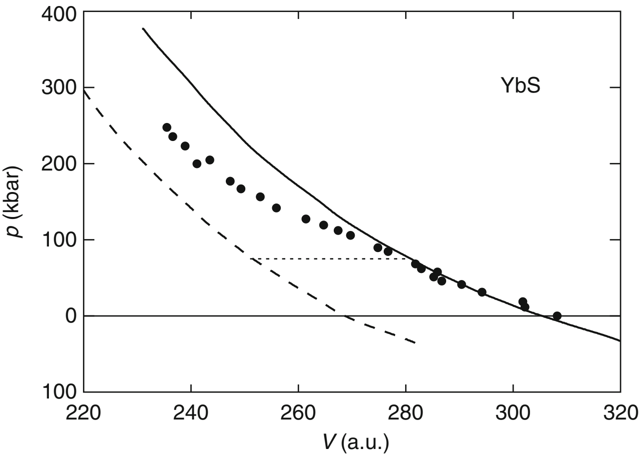

FIGURE 15 Equation of state for YbS as calculated by the SIC-LSD method. The two theoretical curves correspond to divalent Yb f^{14} ions (solid line) and trivalent Yb f^{13} ions (dashed line), respectively. The filled circles are the experimental data of Syassen et al. (1986). The dotted line marks the theoretical transition at $P_t = 7.5$ GPa.

4.6 Valence of lanthanide oxides

The lanthanide oxides find important applications in the catalysis, lighting, and electronics industries. In particular, the design of advanced devices based upon the integration of lanthanide oxides with silicon and other semiconductors calls for a detailed understanding of the bonding, electronic, and dielectric properties of these materials (Scarel et al., 2007). Here, we use the SIC-LSD to address the issue of the lanthanide valence in the dioxides RO_2 and sesquioxides R_2O_3, for R = Ce, Pr, Nd, Pm, Sm, Eu, Gd, Tb, Dy, and Ho.

Even though all the lanthanide elements readily oxidize, they do so with varying strength (Holland-Moritz, 1992). Ce metal oxidizes completely to CeO_2 in the presence of air, whereas the stoichiometric fluorite structured PrO_2 and TbO_2 exist under positive oxygen pressure. With the exception of Tb, the R-oxides from Nd onwards all occur naturally as sesquioxides R_2O_3. Under suitable conditions, all the lanthanide elements form as sesquioxides (Eyring, 1978), and there is general agreement, that in the corresponding ground states, the lanthanide atoms are in the trivalent R^{3+} configuration (Tanaka et al., 1995; Moewes et al., 1999). The debate is, however, still ongoing as to the tetravalent (Kern et al., 1984; Wuilloud et al., 1984; Hanyu et al., 1985; Karnatak et al., 1987; Marabelli and Wachter, 1987; Boothroyd et al., 2001) or intermediate-valent (Bianconi et al., 1988; Ogasawara et al., 1991; Butorin et al., 1997) configuration of the R-ions in CeO_2, PrO_2, and TbO_2. In the SIC-LSD approach, by studying the divalent, trivalent, and tetravalent configurations of the lanthanide ions in the respective oxides, we determined the valencies from first-principles and established the corresponding ground state electronic structure.

The calculated energy differences between respectively the tetravalent and trivalent R-ion configurations for the corresponding dioxides and sesquioxides are shown in Figure 16. For CeO_2, we find a clearly preferred tetravalent ground state configuration, as indicated by a large negative energy difference of 2.4 eV. With all the f-electrons delocalized, CeO_2 is thus best described in the LSD approximation, in line with results from earlier band structure calculations (Koelling et al., 1983; Skorodumova et al., 2001). The tetravalent state is also energetically most favourable for PrO_2, indicating a $\mathrm{Pr}(f^1)$ ground state configuration. The corresponding DOS is shown in Figure 17B, where it is compared with the LSD configuration with $\mathrm{Pr}(f^0)$ in Figure 17A and the trivalent configuration with $\mathrm{Pr}(f^2)$ in Figure 17C. In Figure 17A, with all the f-electrons treated as delocalized, the Fermi level is situated in the f-peak, in accordance with the LSD calculations by Koelling et al. (1983), but in disagreement with the experimentally observed insulating nature of PrO_2. Localizing a single f-electron gives an insulator, with the Fermi level situated between the occupied O p-states and the empty Pr f-states, as shown in Figure 17B. In the trivalent scenario of Figure 17C, a further f-electron becomes localized to form $\mathrm{Pr}(f^2)$, which results in some of the O p-states becoming depopulated (Wulff et al., 1988) with an associated cost in band formation energy that outweighs the gain in localization energy by 1.4 eV as can be seen from Figure 16.

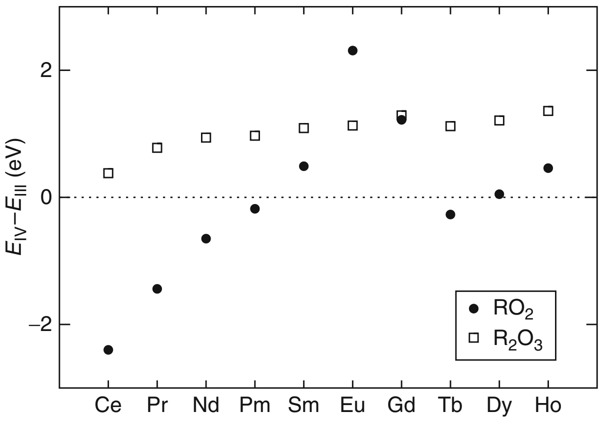

FIGURE 16 Energy difference $E_{IV}-E_{III}$ (in eV per lanthanide ion) between the tetravalent and trivalent lanthanide configurations in dioxides (solid circles) and A-type (hexagonal) sesquioxides (open squares).

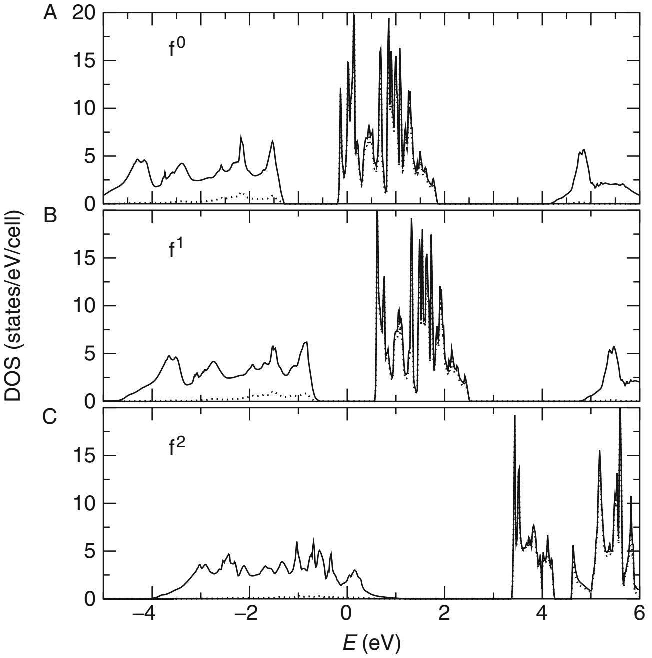

FIGURE 17 Total DOS (solid line) and f-projected DOS (dotted line) for PrO_2, with Pr in (A) the pentavalent (f^0) configuration, (B) the tetravalent (f^1) configuration, and (C) the trivalent (f^2) configuration. The SIC localized states are not shown. The energy is in units of eV, with zero marking the Fermi level.

The tetravalent ground state in the SIC-LSD translates into a gain of band formation energy from delocalizing an additional f-electron compared with the corresponding trivalent lanthanide metal. In the light lanthanides, the f-electrons are less tightly bound, resulting in compounds that display a larger oxygen coordination number, as the lanthanide atom donates electrons to each of the strongly electronegative O ions. In TbO_2, the tetravalent ground state configuration is also found to be energetically the most favourable, although the energy difference $E_{IV} - E_{III}$ is now reduced to 0.27 eV as can be seen from Figure 16. In Tb, the extra f-electron on top of the half-filled band is again less tightly bound that results in a valence larger than 3+ . The calculated equilibrium volumes in the tetravalent ground state are in good agreement with the experimental values, respectively for CeO_2, 39.61 $Å^3$ ($V_{exp} = 39.6$ $Å^3$); for PrO_2, 39.22 $Å^3$ ($V_{exp} = 39.4$ $Å^3$); and for TbO_2, 36.50 $Å^3$ ($V_{exp} = 35.6$ $Å^3$). We similarly find a tetravalent ground state for NdO_2 and PmO_2, but it turns out that these dioxides do not form in nature, that is it is found that these compounds are unstable with respect to the reduction to their respective sesquioxide, as is the case for all lanthanides, except for CeO_2, PrO_2, and TbO_2.

Calculations based on the LSD approximation tend to give a reliable picture of the electronic structure of CeO_2 (Koelling et al., 1983), resulting in the tetravalent ground state configuration, with no localized f-electrons. We find an energy gap between the valence band and the unoccupied conduction band (situated above the empty f-peak) to be around 5.1 eV (Gerward et al., 2005), as compared with the experimental value of 6 eV (Wuilloud et al., 1984). Not surprisingly, the LSD somewhat underestimates the band gap. Recent calculations with respectively the hybrid functional method (Silva et al., 2007), and the LDA + U approach (Loschen et al., 2007), find good agreement with experimental data when applied to CeO_2. For PrO_2, we find an energy gap of approximately 1.1 eV in the ground state f^1 configuration, considerably larger than the 0.262 eV derived from conductivity measurements by Gardiner et al. (2004), but smaller than the 6 eV obtained in LDA + U calculations treating the localized 4f-states with the open core approach (Diviš and Rusz, 2005).

Our calculations do not confirm an intermediate valent ground state for either dioxide, which has, however, been proposed as a possible interpretation of core-level spectroscopy data (Bianconi et al., 1988; Ogasawara et al., 1991; Butorin et al., 1997). Koelling et al. (1983) have instead argued that the intermediate valence scenario is related to the ionic description of the lanthanide-oxides, which cannot account for the covalent f–p bonding. In the ionic picture, valence is defined as the number of valence electrons that have transferred from the R atoms to the O atoms, that is f-electrons do not participate in the bonding, and only exist as localized states at the lanthanide sites. Thus, a given integer valent configuration has an integral number of f-electrons, and consequently, a non-integral number of f-electrons can only result from an intermediate valence scenario. In the SIC picture, both localized and delocalized f-states coexist. The delocalized f-states are allowed to participate in the band formation, and they occur as part of the tails of the O p-states. The overall number of f-electrons is non-integral, in analogy to the intermediate valent picture, however not as a consequence of intermediate valence but rather as a result of the p–f mixing.

At temperatures below 2000 °C, the lanthanide sesquioxides adopt three different structure types (Eyring, 1978). The light lanthanides crystallize in the hexagonal La_2O_3 structure (A-type, space group $P3m1$, no. 164), and the heavy lanthanides assume the cubic Mn_2O_3 structure (C-type, $Ia3$, no. 206), also known as the bixbyite structure (Villars and Calvert, 1991). The middle lanthanides can be found either in the C-type structure or a monoclinic distortion hereof (B-type structure). Transitions between the different structure types are induced under specific temperature and pressure conditions (Hoekstra and Gingerich, 1964). We investigated the electronic structure of both A-type and C-type sesquioxides (Petit et al., 2005). The valence energy difference $E_{\mathrm{IV}} - E_{\mathrm{III}}$ for the sesquioxides in the A-type structure is displayed in Figure 16, where it can be seen that the trivalent configuration is the ground state in all cases. The overall trend is that of an increasing energy difference from Ce_2O_3 to Gd_2O_3 and again from Tb_2O_3 to Ho_2O_3. Apart from the extraordinary stability of the half-filled shell, which results in a slightly increased influence of the tetravalent configuration in Tb_2O_3 relative to Gd_2O_3, the general tendency towards trivalence is clearly related to the increasing localization of the f-electrons with increasing atomic number.

A similar total energy behaviour is observed for the simulated C-type structure sesquioxides. The highly directional f-orbitals are only partially able to screen each other from the attractive force of the nucleus, which results in a steadily increasing effective nuclear charge with an increasing number of f-electrons. The increase in localization leads to the well-known lanthanide contraction, that is the decrease in ionic radius across the lanthanide series, which is also reflected in the volumes of the lanthanide sesquioxide series, as illustrated in Figure 18. We notice that the agreement between theory and experiment is considerably better for the C-type structure than for the A-type one, which might be related to the fact that the ASA used in the calculations is likely less reliable when applied to the hexagonal A-type structure than when applied to the higher symmetry cubic C-type structure. Overall, for the C-type structure, the calculated values are in better agreement with the experimental values for the early lanthanide sesquioxides. This behaviour is compared in Figure 18 to the results obtained with the projector augmented PAW (Hirosaki et al., 2003). Here the localized partly filled f-shell is treated as part of the core, which results in better agreement with experiment for the later lanthanides with localized f-states, but which may be too restrictive an approximation for the early lanthanide sesquioxides.

The DOS and band structures for all the sesquioxides are quite similar and differ mostly with respect to the unoccupied f-electron states (Petit et al., 2007). In Figure 19, we show three representative examples, namely, Eu_2O_3, Gd_2O_3, and Tb_2O_3. The energy zero has been placed at the top of the valence bands. The valence band, originating from the O p-states, is of equal width (of the order of 3.5 eV) in all the compounds, and is completely filled as a result of hybridization and charge transfer. In the DOS of Eu_2O_3, depicted in the top panel of Figure 19, an empty f-band is situated in the gap between the valence band and the (non-f) conduction band. The low position of the f-band is caused by the exchange

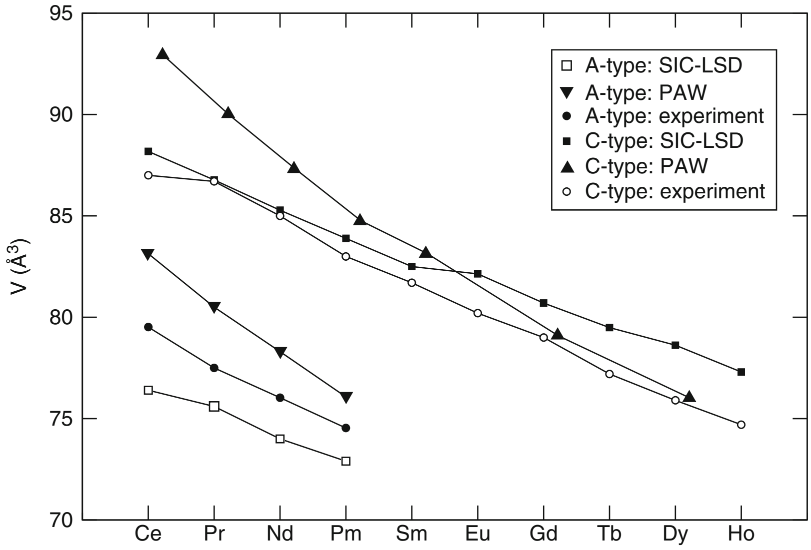

FIGURE 18 Calculated equilibrium volumes (in Å^3) of the lanthanide sesquioxides, crystallizing in the hexagonal A-type structure and the cubic C-type structure. The triangles, squares, and circles refer to PAW (Hirosaki et al., 2003), SIC-LSD (present), and experimental results (Eyring, 1978), respectively.

interaction with the localized f^6 shell of Eu. In Gd_2O_3 and Tb_2O_3, there are only unoccupied minority spin f-states, and their position is significantly higher. All the sesquioxides, with the exception of C-type Eu_2O_3 are found to be insulators.

In Figure 20A, we show the evolution across the sesquioxide series of the unoccupied f-band (hatched area indicating f-band width) and the non-f conduction band edge with respect to the top of the O p-bands (at zero energy). With respect to experimental data, in Figure 20B, one notices a considerable discrepancy between optical (Prokofiev et al., 1996) and conductivity (Lal and Gaur, 1988) measurements of the energy gaps. The direct comparison between theory and experiment (Petit et al., 2005) is further complicated by the fact that in the SIC-LSD, the bare f-bands always appear at too high binding energies due to the neglect of screening and relaxation effects (Temmerman et al., 1993). The position of the occupied and empty f-states with respect to the band edges is crucial, and the interpretation of the optical data is that the empty f-levels are situated above the conduction band minimum, while the gap energies obtained from conductivity measurements indicate that, for some compounds, the transitions are from valence $\rightarrow f$, that is that the empty levels can be situated in the gap between valence band maximum and conduction band minimum.

From experiment, we know that whereas all the lanthanide sesquioxides can be found in nature, the only lanthanide dioxides that occur naturally are CeO_2, PrO_2, and TbO_2. On the other hand, SIC-LSD theory concludes that all the lanthanide sesquioxides prefer the trivalent ground state configuration, whereas the dioxides can be separated into tetravalent light lanthanide dioxides, including

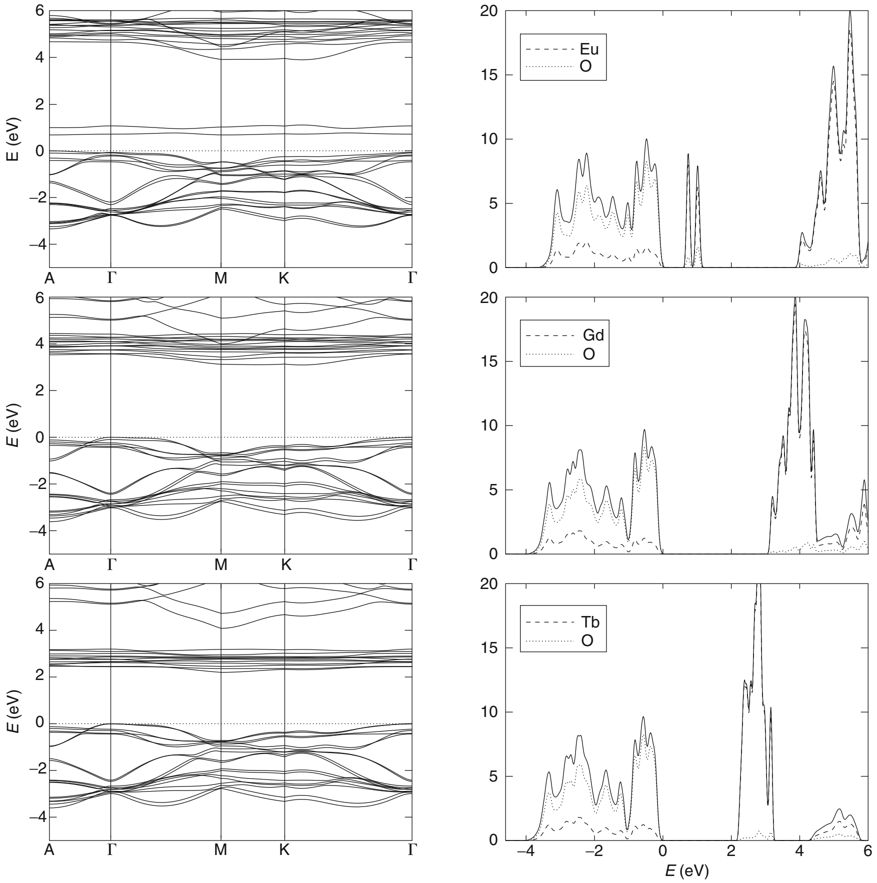

FIGURE 19 Band structure and DOS (in states per formula unit and eV) for Eu_2O_3 (top), Gd_2O_3 (middle), and Tb_2O_3 (bottom) in the trivalent configuration, in the A-type structure, and at the calculated equilibrium volume. The energy zero has been put at the top of the valence bands. The horizontal axis in the band structure diagram refers to the wave vector **k** along the symmetry directions denoted by the high symmetry points of A, Γ, M, K, Γ, in the BZ of the A-type lattice. The total DOS in the DOS plots is indicated by a continuous line, whereas the R and O partial DOS are shown with dashed and dotted lines, respectively. The SIC localized states are not shown.

CeO_2 and PrO_2, and trivalent heavy lanthanide dioxides, with the exception of TbO_2, which again prefers the tetravalent ground state configuration. This leads us to conclude that with respect to the naturally occurring lanthanide oxides, the oxidation process from sesquioxide to dioxide goes hand in hand with the delocalization of an extra electron. The question then is why the heavy lanthanide dioxides do not form in nature. To shed some light on this issue, we have investigated the oxidation process

$$R_2O_3 + \frac{1}{2}O_2 \rightleftharpoons 2RO_2. \qquad (39)$$

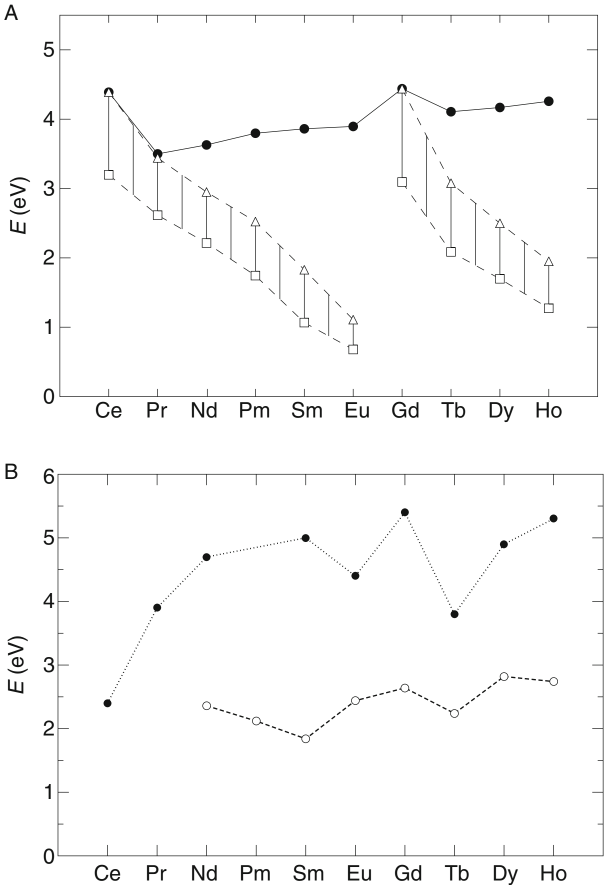

FIGURE 20 Band gaps of the lanthanide sesquioxides. Energy is in units of eV, and the valence band maximum is situated at zero energy. (A) Evolution of the SIC-LSD gap structure through the lanthanide sesquioxide series (A-type). The unoccupied f-band (of majority spin character only from Ce to Eu) is positioned between squares and triangles (hatched area). The non-f conduction band edge is marked with solid circles. (B) Experimental values for the optical gaps (Prokofiev et al., 1996) are shown as solid circles connected by a dotted line, while the energy gap E_g values, deduced from high-temperature conductivity experiments (Lal and Gaur, 1988) are shown as open circles connected by a dashed line.

The balance of this reaction in general will depend on the Gibbs free energy of the reactants at the given temperature and pressure. The *ab initio* calculations of these quantities are beyond the capability of the present theory. However, we can still to some extent analyse the reaction (39) by looking at the zero temperature and zero pressure limit (Petit et al., 2005). In that case, the free energy difference between the reactants reduces to the corresponding total energy difference, as obtained by the SIC calculations, namely

$$E_{\mathrm{ox}} \equiv 2E^{\mathrm{SIC}}(\mathrm{RO_2}) - E^{\mathrm{SIC}}(\mathrm{R_2O_3}) - \mu_{\mathrm{O}}, \qquad (40)$$

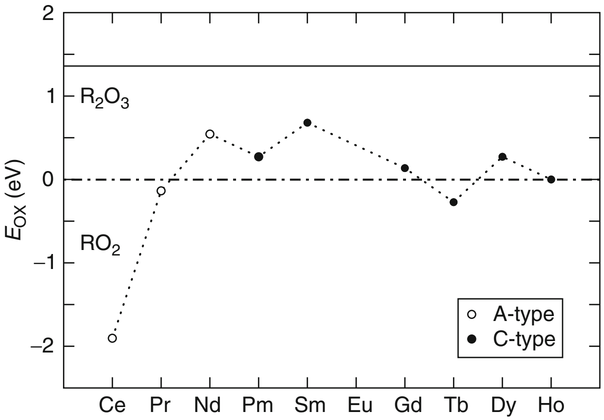

FIGURE 21 Oxidation energies, E_{ox} in Eq. (40), for the lanthanides Ce to Ho. The filled circle is for the cubic C-type sesquioxide and the open circle for the A-type hexagonal structure of the sesquioxide. Negative values indicate that the dioxide is stable. The chemical potential of free O is taken as $\mu_O = -6.12$ eV. The solid line just below 1.5 eV indicates the dioxide/sesquioxide borderline in the case when the FP-LMTO calculated value $\mu_O = -4.76$ eV is used.

where μ_O is the chemical potential of O. The result of this study is shown in Figure 21. Here a negative (positive) energy means that the formation of the dioxide (sesquioxide) is preferred energetically. Furthermore, the oxidation energies [Eq. (40)] with respect to both the A- and C-type sesquioxides were calculated, and the energetically most favourable of these two structures is compared to the corresponding dioxide in Figure 21. The conclusion is that for Ce, Pr, and Tb, the dioxide is energetically preferred. With respect to the corresponding sesquioxides, the A-type is closest in energy for Ce and Pr, while the C-type is closest in energy to the dioxide for Tb. All other compounds prefer reduction to the sesquioxide, which crystallizes in the A-type structure for Nd and the C-type structure for the remainder. This overall picture is in relatively good agreement with the degree of oxidation observed in the naturally occurring compounds.

5. LOCAL SPIN AND ORBITAL MAGNETIC MOMENTS

The SIC-LSD method provides an approach for the *ab initio* determination of the magnetic moment of materials. *Ab initio* theory has the advantage that it can be used to calculate quantities that are inaccessible to experiment. Here we exploit this advantage to explore the magnetic moments of the lanthanide elements. The electrons in the lanthanides generate an exchange field that is modelled as half of the difference in potential felt by spin-up and spin-down electrons. The exchange field defines a direction in the crystal and this is arbitrarily chosen as the *z*-direction. All magnetic moments are defined as parallel or anti-parallel to the exchange field. Within the electronic structure calculation, we define lattice vectors that also determine the *z*-direction and so a direction of the moment within the crystal can be defined. The results discussed in this section are all the result of fully self-consistent relativistic calculations unless otherwise stated. This is absolutely necessary for a quantitative evaluation of the orbital moments. We discuss the light lanthanides and the heavy lanthanides separately.

5.1 Hund's rules

In the description of the standard model, Section 2.2, it is assumed that the electrons distribute themselves among the available f-states according to Hund's rules. However, Hund's rules are essentially based on experiment. A good first-principles theory of electronic structure is one where Hund's rules drop out of the theory rather than having to be included empirically.

As already said, to apply the SIC to the f-states, it is first necessary to decide which (and how many) states it should be applied to based on total energy considerations. Of course, it needs to be applied to the occupied states, but not to the unoccupied ones. If we take trivalent praseodymium as our example, there are nominally two occupied f-states out of a possible 14, and in principle we can choose to occupy any 2. Let us start by occupying two states of opposite spin and a variety of possible m_l quantum numbers. During iteration to self-consistency, the SIC-states adjust but largely keep their initial characteristics, that is the scheme possesses many different solutions, which can be accessed by different starting conditions. In the end, it is the total energy that selects the proper ground state. For each arbitrarily chosen pair of initially occupied m_l values, a fully self-consistent SIC-LSD calculation is performed and we plot the energy and the total orbital moment. This process is repeated choosing two states with parallel spins. The results of this are shown in Figure 22. It is clear that the data points separate into two clusters. Those above –2.28 Ry are those where the two spins are anti-parallel (solid circles) and those below –2.28 Ry are those with parallel spins (open circles). Evidently lining up the spins parallel to each other of the individual states is energetically preferable to having them anti-parallel, and so Hund's first rule is satisfied. Examining this figure further, we see that for the states with parallel spin, there is a rough linearity between the total energy and the orbital moment with the minimum total energy being when the orbital moment has maximum magnitude anti-parallel to the spin moment. Clearly, then Pr obeys all three of Hund's rules. In all honesty, Pr is the best example, but the trends displayed here are also observed in all the light lanthanides. In the heavy lanthanides, similar behaviour is displayed but the lowest total energy is when the orbital moment is a maximum and parallel to the spin moment, also completely consistent with Hund's rules.

5.2 The heavy lanthanides

Although the relativistic SIC-LSD (Beiden et al., 1997) calculations have been carried out for all the lanthanide metals, we start discussing results from the heavy lanthanides. Thus, in Figures 23 and 24, we display the densities of states for Tb and Ho as illustrative examples. Figure 23A shows the majority spin d and f

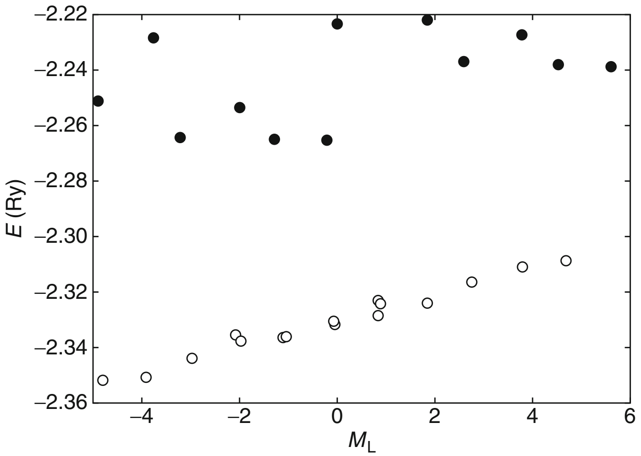

FIGURE 22 The total energy of praseodymium calculated as a function of orbital and spin magnetic moments. The SIC was applied to two f-states and the calculations were performed for a variety of m_s and m_l quantum numbers. All the total energies above −2.28 Ry (solid circles) are calculated with the spin of the localized electrons anti-parallel, while the points below −2.28 Ry (open circles) had parallel spins. This shows that the parallel arrangement is preferred and is consistent with Hund's first rule. The rough proportionality between total energy and orbital moment displayed by the parallel spin states, together with the fact that the most negative orbital moment has the lowest energy, is consistent with Hund's second rule.

densities of states for Tb. Figure 23B shows the equivalent minority spin curves. The details are described in the figure caption. In Figure 24A and B, we display the equivalent curves for Ho. There are several key points to note about these curves. First, the amount of minority (majority) spin f-character hybridized into the majority (minority) spin bands is small on the scale of the f DOS, but appreciable on the scale of the d DOS. Second, the amount of hybridization between different f-spin states increases from Tb to Ho and generally increases in the heavy lanthanides as atomic number increases. It is straightforward to understand why this occurs. At the Gd end of the series, the exchange field dominates the spin-orbit coupling and so states are split according to their spin. At the Yb end of the series, the f-states are more or less completely filled and there is no exchange field, the dominant splitting in the f-states is spin-orbit coupling where each individual state has mixed spin-up and spin-down character. The change from exchange splitting to spin-orbit splitting is not abrupt, but occurs gradually as we proceed across the 4f-series. Comparison of the d-bands in Figures 23 and 24 shows that they are all broadly similar. However, the effect of changing f-hybridization and small changes in the lattice such as a slightly different lattice constant and c/a ratio means that the details of the d densities of states vary from element to element. In turn, this affects the calculated lattice and magnetic properties.

Now we go on to discuss the results of the calculation of the heavy lanthanide magnetic moments. These calculations were performed on a hexagonal close packed lattice at the experimental lattice constant, so these numbers should be

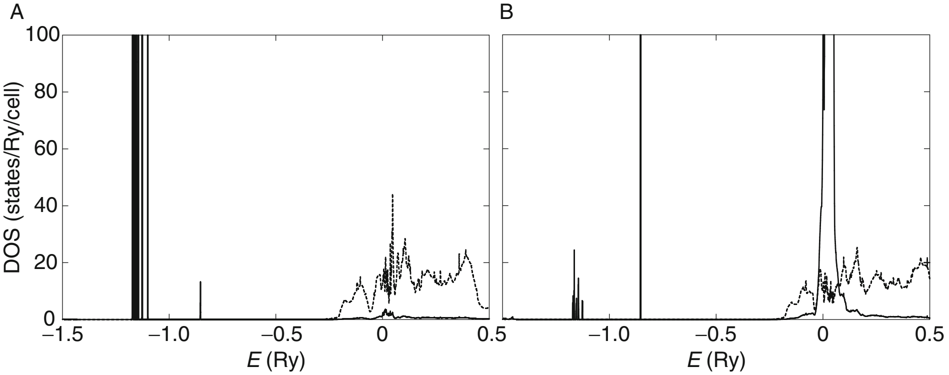

FIGURE 23 The d (dashed lines) and f (full lines) densities of states for Tb with respect to the Fermi energy. (A) Majority spin: the very tall and narrow peaks at around −1.15Ry are the majority spin f-states. The small peak at −0.85 is majority spin f hybridized into the minority spin states through spin-orbit coupling. From −0.25 to 0.5Ry, the d-bands dominate the DOS, but the lower curve indicates a very small majority spin f-contribution in this region. (B) Minority spin: there is considerable minority spin character hybridized into the occupied spin-up f-states. The single occupied predominantly minority spin f-state is at −0.85Ry. The minority spin f-states are close to the Fermi energy and these overlap and hybridize with the d-bands.

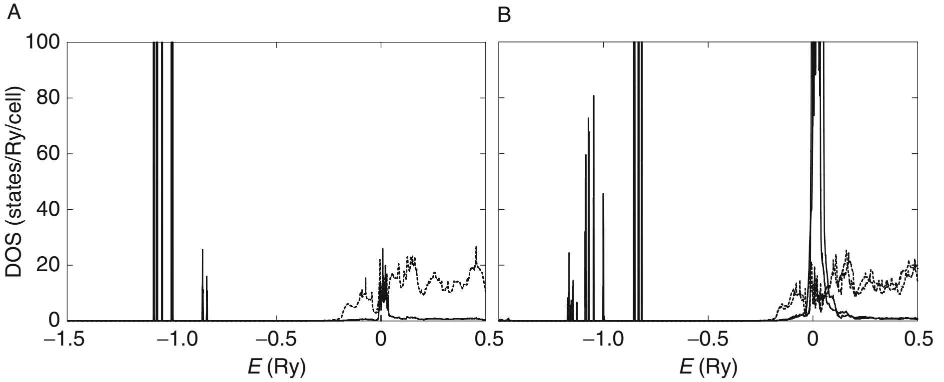

FIGURE 24 The d (dashed lines) and f (full lines) densities of states for Ho with respect to the Fermi energy. (A) Majority spin: The very tall and narrow peaks at around −1.1Ry are the majority spin f-states. The small peaks at −0.85 are majority spin f hybridized into the minority spin states through spin-orbit coupling. From −0.25 to 0.5Ry, the d-bands dominate the DOS, but the lower curve indicates a very small majority spin f-contribution in this region. There is considerable majority spin DOS hybridized into the d-bands around the Fermi energy. (B) Minority spin: There is considerable minority spin character hybridized into the occupied spin-up f-states. The three occupied predominantly minority spin f-states are at −0.85Ry. The minority spin f-states are close to the Fermi energy and these overlap and hybridize with the d-bands.

TABLE 6 The magnetic properties of the heavy lanthanides. The magnetic moments are all written in units of Bohr magnetons per atom. The first column is the spin magnetic moment of the valence states. The second column is the orbital moment associated with the valence electrons. The third column gives the spin moment for the SIC f-states, the fourth column is their orbital moment. The fifth column is the sum of all the previous contributions. The final column is the experimental saturated magnetic moment (Jensen and Mackintosh, 1991). For Gd through Tm, the calculations were done in the trivalent state. For Yb, the divalent state was the only state to which the calculation could be reliably converged and the moments are all close to zero and so are not shown. From Gd through Tm, the calculations were performed in the Hund's rule ground state

	Valence moments		f(SIC) moments		Total moment	
	Spin	Orbital	Spin	Orbital	Theoretical	Experimental
Gd	−0.05	0.53	6.94	0.013	7.43	7.63
Tb	−0.29	0.40	5.90	3.03	9.04	9.34
Dy	−0.45	0.12	4.88	5.04	9.59	10.33
Ho	−0.56	−0.34	3.84	6.06	9.00	10.34
Er	−0.65	−1.02	2.86	6.06	7.25	9.1
Tm	−0.83	−1.96	1.88	5.05	4.14	7.14

directly comparable with experiment. In Table 6, we lay out all the magnetic quantities calculated within an SIC-LSD calculation. These are the expectation values of $2S_z$ and L_z, that is assuming an ordered magnetic state with a local intrinsic exchange field directed along the z-axis. The quantities obtained are those for the Hund's rule arrangement of initial states within the f-manifold. In principle, we could show systematically that this is the ground state by performing calculations for every possible configuration of electrons and finding that the Hund's rule state is the one with minimum energy. We have done this for some elements such as Pr above, and found the Hund's rule result, but a full systematic study has not been carried out. However, we assume that this could have been done and the Hund's rule configuration is assumed henceforth. The normal procedure to calculate the total magnetic moment for these elements would be to add all the different, valence and localized, contributions together. However, if we do this, it does not work well when compared with the experimental saturated magnetic moment as can be seen from the last two columns of Table 6. There are only two systems, Gd and Tb, for which our calculations show a reasonable agreement with the experimental values of the saturated magnetic moment. These results of the calculations do not compare as well as the values obtained from the standard model (see Table 1), which contain only the localized f contributions. In particular, for Tm and Er, the valence orbital magnetic moments are large and anti-parallel to the orbital magnetic moments from the localized f-states. The valence orbital moment for Gd is positive, decreases for Tb and Dy, changes sign in Ho. The valence spin magnetic moment changes continuously from –0.05 in Gd to –0.83 in Tm. Thus, the present theory seems to overestimate these valence contributions to the ordered moment of the lanthanides. The

TABLE 7 The magnetic properties of the heavy lanthanides. The magnetic moments are all written in units of Bohr magnetons per atom. The first three columns are the *S*, *L*, and *J* quantum numbers and g_J is the effective Landé g-factor, all of which can be compared with the equivalent results in Table 1. The remaining columns are, respectively, the effective moments calculated according to Eq. (5) and the experimental moment deduced from the Curie-Weiss behaviour of the magnetic susceptibilities in the paramagnetic phases (Jensen and Mackintosh, 1991). The Hund's rule ground state was chosen throughout

	S	L	J	g_J	μ_t	μ_e
Gd	3.47	0.013	3.48	1.997	7.88	7.95
Tb	2.95	3.03	5.98	1.493	9.65	9.5
Dy	2.44	5.04	7.48	1.326	10.56	10.6
Ho	1.92	6.06	7.98	1.240	10.50	10.4
Er	1.43	6.06	7.49	1.191	9.50	9.5
Tm	0.94	5.05	5.99	1.157	7.49	7.3

SIC-LSD method has a slight tendency to overlocalize states and as a result brings a small amount of unphysical valence f-states below the Fermi energy. This means that the lanthanides become divalent slightly too early as we proceed across the Periodic Table (Strange et al., 1999). The extra unphysical valence f-states replace d-states. However, they play a similar role in bonding to the d-states, so do not affect the prediction of crystal structural properties, but can distort the prediction of the magnetic moment.

A better agreement with experiment is obtained if the valence moments are ignored, as in the following procedure. The SIC states are highly localized on a particular lattice site. This can be seen from Table 6 where the values of L_z and S_z of the SIC states of f-character are essentially the atomic values presented in Table 1. Thus, we may interpret these as projections onto the z-axis corresponding to effective S, L, and ensuing J quantum numbers, which can be used in Eqs. (4) and (5) to determine the total magnetic moment due to the SIC states. In this estimate, the moment of the occupied valence states is ignored. In Table 7, we show the results of this procedure and compare them directly with the experimental values. Surprisingly with the omission of the spin and orbital moments of the valence states, we obtain excellent agreement between theory and experiment. This can indicate that the experiment provides only the contribution of the localized states to the spin and orbital magnetic moments. This is plausible since these experimental magnetic moments are deduced from the linear dependence of the inverse magnetic susceptibilities on temperature in the high-temperature paramagnetic phases, Eq. (6). At these elevated temperatures, the magnetic behaviour is best described by the DLM model (see the next section), according to which the local f magnetic moments are not aligned but rather point randomly in all directions. As a consequence, one does not expect much of a valence electron polarization to develop and could even be negligible, which we assumed in our analysis presented in Table 7. The success of this reasoning might also be construed as an illustration on how well the SIC describes the localized part of the f-states.

5.3 The light lanthanides

In this section, we discuss some calculations of the magnetic moments of the light lanthanides using SIC-LSD in a variety of situations. We have calculated the magnetic moments of all the light lanthanides on an fcc lattice with an identical volume per atom for each element. This has enabled us to untangle the effect of small lattice constant changes on the moment from the effect of the extra f-electron as we proceed across the Periodic Table. The results of these calculations are shown in Tables 8 and 9, where we have explicitly shown all contributions to the moment. In Table 8 are shown the ordered moments, whereas in Table 9 are shown the paramagnetic moments, extracted as outlined for the heavy lanthanides in subsection 5.2.

TABLE 8 The magnetic properties of the light lanthanides. The magnetic moments are all written in units of the Bohr magneton. The first column is the spin magnetic moment of the valence states. The second column is the orbital moment associated with the valence electrons. Column three is the spin moment for the SIC f-states, the next column is their orbital moment. The fifth column is the total moment and the last column is the experimental saturated magnetic moment (Jensen and Mackintosh, 1991). For Ce through Sm, the calculations were done in the trivalent state, whereas for Eu, the calculation was done in the divalent state. From Ce through Sm, the state chosen was the Hund's rule ground state and this turned out to be the lowest energy state

	Valence moments		f(SIC) moments		Total moment	
	Spin	Orbital	Spin	Orbital	Theoretical	Experimental
Ce	0.32	0.03	0.96	2.96	1.71	0.6
Pr	0.44	0.16	1.98	4.96	2.7	2.7
Nd	0.34	0.51	2.94	5.93	3.16	2.2
Pm	0.32	1.74	3.94	5.95	3.43	–
Sm	0.55	1.69	4.94	4.94	1.14	0.13
Eu	0.42	0.001	6.96	0.01	7.37	5.1

TABLE 9 The magnetic properties of the light lanthanides.The magnetic moments are all written in units of Bohr magnetons per atom. The first three columns are the *S*, *L*, and *J* quantum numbers and g_J is the effective Landé g-factor, all of which can be compared with the equivalent results in Table 1. The remaining columns are the calculated effective moment calculated according to Eq. (5) and the experimental moment (Jensen and Mackintosh, 1991). The Hund's rule ground state was chosen throughout

	S	L	J	g_J	μ_t	μ_e
Ce	0.48	2.96	2.48	0.93	2.73	2.4
Pr	0.99	4.96	3.97	0.80	3.55	3.5
Nd	1.47	5.93	4.46	0.73	3.60	3.5
Pm	1.97	5.95	3.98	0.60	2.67	
Sm	2.47	4.94	2.47	0.29	0.84	1.5
Eu	3.48	0.01	3.47	1.96	7.72	3.4

TABLE 10 The magnetic properties of neodymium on a variety of crystal lattices (fcc, bcc, simple cubic, and hexagonal lattices) calculated as described in the text. The magnetic moments are all written in units of the Bohr magneton. The second column is the spin magnetic moment of the valence s, p, d, and f-states. The third column is the orbital moment associated with the valence electrons. The final two columns are the spin and orbital magnetic moments of the SI-corrected f-states

	Valence moments		f(SIC) moments	
	Spin	Orbital	Spin	Orbital
fcc	0.34	0.51	2.94	5.93
bcc	0.75	0.51	2.95	5.95
sic	0.90	0.88	2.93	5.89
hcp	0.74	0.34	2.94	5.96

It is notable that the spin and orbital contributions of the localized states are nearly the same as for the ionic case. This shows that in the light lanthanides, the f-states are as localized as for the heavy lanthanides. For the paramagnetic moments, the agreement between theory and experiment is very satisfactory (Table 9) and much better than using a band description of adding the contributions of the localized and delocalized states (Table 8). Sm and Eu are less well described by this procedure and it could be that the assumption of pure trivalent Sm and pure divalent Eu are not fully applicable and some divalent Sm and some trivalent Eu might be mixed into the ground state.

Now let us consider the effect of crystal environment on the magnetic moment of the lanthanides. In Table 10, we show the results of calculations of the magnetic moment of neodymium on several common crystal lattices. A trivalent Nd ion yields a spin moment of $3\mu_B$ and an orbital moment of $6\mu_B$. In the final two columns of Table 10, we see that the SIC-LSD theory yields values slightly less than, but very close to, these numbers. This is independent of the crystal structure. The valence electron polarization varies markedly between different crystal structures from $0.34\mu_B$ on the fcc structure to $0.90\mu_B$ on the simple cubic structure. It is not at all surprising that the valence electron moments can differ so strongly between different crystal structures. The importance of symmetry in electronic structure calculations cannot be overestimated. For example, the hcp lattice does not have a centre of inversion symmetry and this allows states with different parity to hybridize, so direct f–d hybridization is allowed. However, symmetry considerations forbid f–d hybridization in the cubic structures. Such differences in the way the valence electrons interact with the f-states will undoubtedly lead to strong variations in the valence band moments.

6. SPECTROSCOPY

In this section, we highlight two spectroscopies that can reveal information on the valence of the lanthanide ion. First, we will discuss high-energy photoemission spectroscopy that shows the multiplet nature of the lanthanide ion. Second, we discuss resonant MXRS that allows us to study directly the spin and orbital magnetic properties of the late lanthanides. This experimental probe also has the potential to determine the number and symmetry of the localized f-states. In the first spectroscopy, the starting band structure is that of the LDA, while in the second one, the SIC-LSD is used.

6.1 Hubbard-I approach to lanthanide photoemission spectra

Photoemission is a powerful spectroscopy of lanthanide systems (Campagna et al., 1979). This is due to the distinct atomic multiplet features, which serve as a fingerprint of the configuration adopted by the lanthanide ion in the solid environment.

In photoemission, a photon γ of energy $\hbar\omega$ impinges on a solid, which is an N-electron system in its ground state $|N;\ 0\rangle$. The photon is absorbed and its energy is transferred to an electron, which is emitted, leaving behind a solid with only $N-1$ electrons and in some excited state. Schematically,

$$\gamma + |N;0> \rightarrow |N-1;i> \ +e. \tag{41}$$

The energy of the electron, E_e, is measured and contains information about the excitation energies in the $N-1$ electron system:

$$E_e = \hbar\omega + E(N;0) - E(N-1;i). \tag{42}$$

In principle, all possible excitations contribute to the photoelectron spectrum and the proper quantum mechanical amplitude must be calculated. For the lanthanides, the atomic limit corresponds to the assumption that the photoelectron spectrum is dominated by those processes, where the photon hits a particular ion and causes an excitation on that ion without disturbing the remainder of the crystal. In the standard model, the lanthanide ion would initially be in its trivalent f^n configuration with the Hund's rule ground state multiplet (Table 1 in Section 2.2), and would be transferred into some multiplet ${}^{2S+1}L_J$ within configuration f^{n-1} when the photon has been absorbed. The photoelectron energy would thus be

$$E_e \approx \hbar\omega + E_{\text{ion}}(f^n;0) - E_{\text{ion}}\left(f^{n-1};{}^{2\text{S}+1}L_J\right), \tag{43}$$

where E_{ion} is the atomic energy. The amplitude for this to happen is proportional to the product of two matrix elements:

$$A \propto \langle\psi_e|e^{i\mathbf{kr}}|\phi_f\rangle \cdot \langle f^{n-1};{}^{2\text{S}+1}L_J)|\hat{f}|f^n;0\rangle, \tag{44}$$

where the first factor is the matrix element of the photon field between the wavefunction of the outgoing electron ψ_e and the f electron wavefunction ϕ_f, whereas the second factor is the matrix element of the f destruction operator $\hat{f}$ between the final and initial f multiplets.

In view of the strength of the Coulomb interaction, the atomic limit is certainly a quite idealized assumption. For example, in the real world, the kicked out electron still has some distance to travel through the solid before leaving at the surface and might scatter off other atoms or electrons on its way (secondary processes). Furthermore, the sea of conduction electrons might react to the presence of a hole in the f-shell of the targeted ion, with some partial transfer of relaxation energy to the photoelectron (screening). Finally, the photon might induce some further excitations of the conduction electrons (shake up effects), for example by exciting plasmon oscillations. For a complete understanding of photoemission, all such processes must be considered, which is a formidable task. It so happens that the atomic limit is a good first approximation for many lanthanide systems, so we will describe in the following text its implementation within the DMFT framework (Lichtenstein and Katsnelson, 1998) and compare with experimental spectra.

The atomic multiplet DMFT method is a generalization of the Hubbard-I approximation (Hubbard, 1963, 1964a, 1964b) to a full f-manifold of 14 orbitals. The model adopted for the isolated atom considers only these 14 degrees of freedom, and their interaction through the Coulomb force in the atomic Hamiltonian

$$H^{\mathrm{at}} = \frac{1}{2}\sum_{\{m_j\}} U_{m_1m_2m_3m_4}\hat{f}^{\dagger}_{m_1}\hat{f}^{\dagger}_{m_2}\hat{f}_{m_3}\hat{f}_{m_4} + \xi\sum_i \vec{l}_i\cdot\vec{s}_i - \mu\sum_m \hat{f}^{+}_{m}\hat{f}_{m}. \tag{45}$$

Here, index m_j labels the f orbitals, and $\hat{f}^{\dagger}_{m}$ and $\hat{f}_{m}$ are creation and annihilation operators. The first term in Eq. (45) is the electron–electron interaction, with the matrix element

$$\begin{aligned} U_{m_1m_2m_3m_4} &= \iint \frac{\phi^{*}_{m_1}(\mathbf{r})\phi^{*}_{m_2}(\mathbf{r}')\phi_{m_3}(\mathbf{r}')\phi_{m_4}(\mathbf{r})}{|\mathbf{r}-\mathbf{r}'|}\mathrm{d}^3r\,\mathrm{d}^3r' \\ &= \sum_{\ell} a_{\ell}(m_1m_2m_3m_4)F^{\ell}, \end{aligned} \tag{46}$$

where $\varphi_m(\mathbf{r})$ are the f-orbitals. The Coulomb integrals may be expressed in terms of vector coupling coefficients, a_ℓ, and Slater integrals, F_ℓ, with $\ell = 0, 2, 4, 6$ (Lichtenstein and Katsnelson, 1998). The second and third terms in Eq. (45) are the spin-orbit interaction, and a chemical potential term used to align with the Fermi level of the solid [see, e.g., Lebegue et al. (2006a)].

The Hamiltonian, H^{at}, is solved by exact diagonalization in the space of all possible Slater determinants for each of the f^n configurations needed in the calculation (typically for the ground state configuration with n electrons and for the $n \pm 1$ configurations corresponding to excited states). The eigenvalues and eigenvectors, denoted respectively by E_ν and $|\nu\rangle$, are obtained and the atomic Green's function $G^{\mathrm{at}}_{mm'}$ calculated as:

$$G^{\mathrm{at}}_{mm'}(\omega) = \sum_{\lambda v} g_{\lambda\nu}\frac{\langle\lambda|c_m|\nu\rangle\langle\nu|c^{\dagger}_{m'}|\lambda\rangle}{\omega + E_\lambda - E_v}, \tag{47}$$

where the weight factor $g_{\lambda\nu} = \delta_{\lambda,0} + \delta_{\nu,0}$ specifies that one of the states in the sum must be a ground state ($T = 0$). More generally, in a thermal environment, $g_{\lambda\nu}$ is given by the appropriate Boltzmann weights (Lichtenstein and Katsnelson, 1998).

From G^{at} the atomic self-energy, $\Sigma^{\mathrm{at}}_{mm'}$, is finally extracted

$$\Sigma^{\mathrm{at}}_{mm'}(\omega) = \omega\delta_{mm'} - \left(G^{at}\right)^{-1}_{mm'}(\omega), \tag{48}$$

to be inserted in the DMFT Eq. (36) for the solid. We have used the LDA as reference system to obtain G^0. The procedure outlined above describes the multiplets of the 4f atom and combines in a unified framework the strong intra-shell correlation effects related to the 4f electrons and the weaker interaction between s, p, and d electrons. Adding Σ^{at} to the LDA Hamiltonian on the right-hand side of Eq. (36) shifts the f-weight from the narrow LDA bands into the energy positions corresponding to multiplet excitation energies. The matrix elements in the numerator of Eq. (47) ensure that the proper transition amplitudes, according to atomic selection rules, enter the spectral function in Eq. (37). Not included in the description based upon Eq. (37) are the matrix elements between the outgoing photoelectron and the orbital of the left-behind hole. These matrix elements will depend on the angular character of the photo-hole. However, in the applications to be discussed in the following, we will focus on the f-part of the spectral function only, and compare to photoemission spectra using photon energies chosen so as to enhance the f-contribution. Viewed as a DMFT implementation, the above procedure is particularly simple since the impurity is uncoupled from the bath [G_{bath} does not enter in the model Eq. (45)].

In Figures 25 and 26, we show the calculated spectral functions, respectively, for SmAs and SmS using the above theory (Svane et al., 2005). The chemical potential of the reference ion is chosen such that the ground state is $f^5(^6H)$ for trivalent Sm in SmAs and $f^6(^7F)$ for divalent Sm in SmS with an energy separation to the lowest $n-1$ excited levels [$f^4(^5I)$ of 4.0 eV for SmAs and $f^5(^6H)$ of 0.8 eV for SmS, respectively], to coincide with the experimental values for these energies. The Slater integrals entering into the Coulomb matrix in Eq. (46) are almost

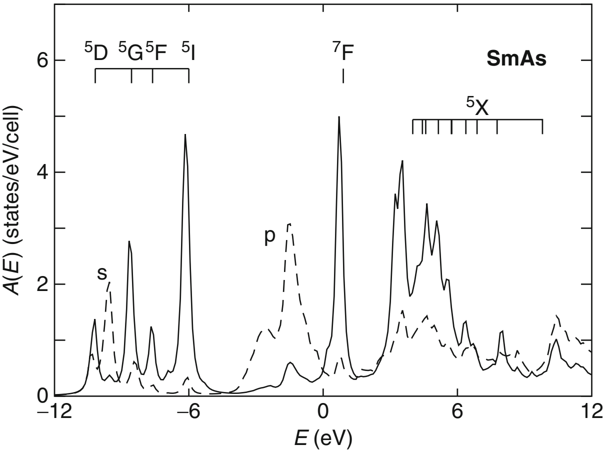

FIGURE 25 The calculated spectral function of trivalent Sm in SmAs at equilibrium volume, with $a = 5.91$ Å. The full curve shows the f-contribution and the dashed curve the non-f contribution. The energy is given relative to the Fermi level. The main lines are characterized by their final state characteristics, either As s, p-bands, or as Sm $f^{n\pm1}$ multiplet term.

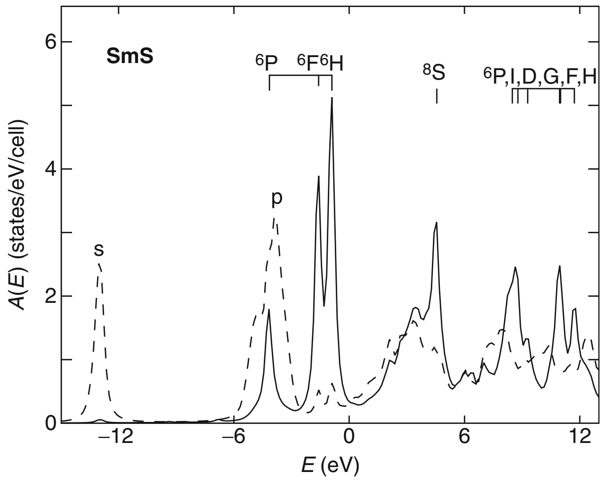

FIGURE 26 The calculated spectral function of divalent Sm in SmS (black phase, $a = 5.95$ Å). The full curve shows the f-contribution and the dashed curve the non-f contribution. The energy is given relative to the Fermi level. The main lines are characterized by their final state characteristics, either as Sulphur s, p-bands or as Sm $f^{n\pm1}$ multiplet term.

equal for the two compounds, $F^\ell = 23.9, 10.6, 6.5,$ and 4.6 eV, respectively, for $\ell = 0, 2, 4, 6$ (evaluated with the f-radial wave at an energy given by the centre of gravity of the occupied f-partial DOS). However, for the direct Coulomb parameter, $F^0 \equiv U$, a screened value of $F^0 = 7.1$ eV was used instead of the unscreened value quoted above.

The SmAs spectral function in Figure 25 shows four distinct peaks between −5 and −12 eV corresponding to the $f^4(^5L)$, $L = D, G, F, I$, final states in the photoemission process. These states agree well with the three-peak structure observed by Pollak et al. (1974) at binding energies of approximately −10.0 eV, −8.2 eV, and −6.0 eV (presuming that the ^5F emission is too weak to lead to a resolvable peak). In the positive frequency range, one observes the ^7F peak just above the Fermi level whereas the f^6 final states of $S = 2$ are situated further up in energy, however, now with a considerable spread due to the many allowed multiplets. The position of the corresponding levels in the reference atomic calculation are marked in the figure.

The SmS spectral function is shown in Figure 26. The spectrum is now characterized by the low binding energy three-peak structure, which is also observed in several experiments (Campagna et al., 1974b; Pollak et al., 1974; Chainani et al., 2002; Ito et al., 2002), at binding energies −0.8 eV, −1.5 eV, and −4.0 eV, and which is attributed to the ^6H, ^6F, and ^6P final states (Campagna et al., 1974b). The latter state coincides with the sulphur p-band, as also found in the calculations. The results in Figure 26 agree well with those obtained by Lehner et al. (1998) by a similar theoretical procedure.

The two spectra of SmAs and SmS demonstrate the distinctly different signatures of trivalent and divalent Sm ions in photoemission. Recent experiments (Chainani et al., 2002; Ito et al., 2002) show traces of Sm f^5 emission in SmS photoemission experiments, possibly also present in older works (Pollak et al., 1974). It is unclear whether this is due to small impurity concentrations or implies a more complicated ground state for SmS than the ideal divalent state, which is normally assumed and indeed also was found by the SIC-LSD calculations discussed in Section 4.3.1. It is well known that doping of SmS can lead to the intermediate valence phase, characterized by photoemission spectra of both the high and low binding energy type (Campagna et al., 1974b; Pollak et al., 1974). The unoccupied states of SmS have been monitored with bremsstrahlung inverse spectroscopy (Oh and Allen, 1984). The spectra reveal two broad structures, approximately 4.5 and 9 eV above the Fermi level, which are in good agreement with the positions in Figure 26 of the ^8S and $^6P, I, D, G, F, H$ features, respectively.

As an example of application of the atomic multiplet theory to the elemental metals (Lebegue et al., 2006a, 2006b), we show in Figure 27 a comparison of the calculated and measured spectra for terbium. The removal part of the spectrum at negative energies, corresponding to $f^8 \rightarrow f^7$ transitions, reveals the exchange splitting between the ^8S and ^6L ($L = G, H, I$) peaks, which in band language translates into the minority and majority spin bands. At positive energy, the spectrum is dominated by the strong peak at 3 eV with a shoulder towards higher energy. There is a one to one correspondence between the observed and calculated peaks, although their relative intensities differ, which could be a matrix element effect. For the high-energy shoulder, there is a 1.5 eV discrepancy in position, which could be due to the neglect of the non-f electrons in the theory. Similarly, the smaller hump-like spectral intensity observed in experiment, in the region just below the Fermi level, could be a reflection of the normal valence electrons,

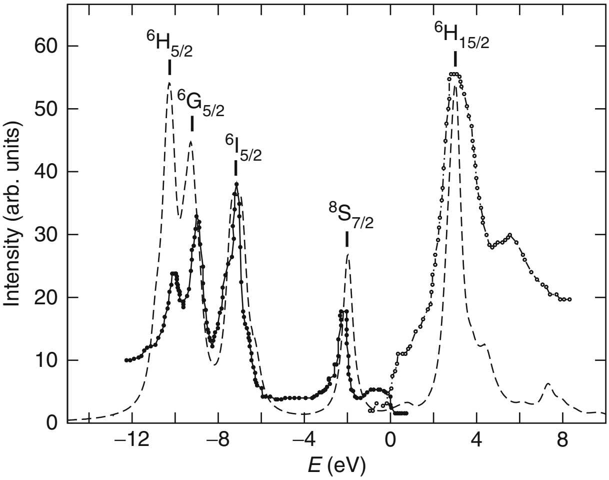

FIGURE 27 The calculated f-contribution to the spectral function of Tb in the hcp structure at the equilibrium volume computed within the Hubbard-I method (dashed line) compared with experiments (circles). Experimental data are X-ray photoemission and bremsstrahlung isochromat spectroscopy from Lang et al. (1981). The Fermi level is at zero energy and the dominating atomic final states are marked.

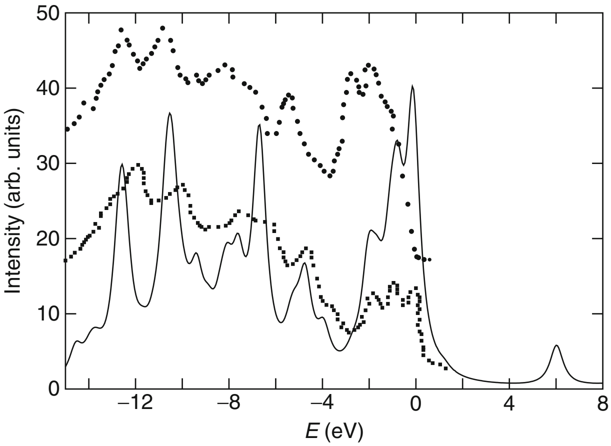

FIGURE 28 The calculated f-contribution to the spectral function of TmSe at equilibrium volume computed within the Hubbard-I method (full line) compared with photoemission spectrum of Campagna et al. (1974b) (solid squares) and of Ufuktepe et al. (1998) (solid circles) (vertically displayed for clarity). The Fermi level is at zero energy.

possibly with some small interaction effects with the f-manifold, which are not treated by the present theory.

As a final example we show in Figure 28 a mixed valence spectrum of TmSe (Lebegue et al., 2005). TmSe is situated between the predominantly trivalent TmS and the divalent TmTe in the thulium monochalcogenides series. The figure shows data from two different experiments (Campagna et al., 1974a; Ufuktepe et al., 1998) with similar results, possibly with a relative shift in the Fermi level position. The recorded photoemission spectra exhibit both low lying excitations (between the Fermi level and 3 eV below) due to $f^{13} \rightarrow f^{12}$ transitions and higher excitations (between 5 and ∼13 eV below the Fermi level) due to $f^{12} \rightarrow f^{11}$ transitions, each of these with their distinct multiplet structure. TmTe shows only the former and TmS only the latter kinds of excitations (Lebegue et al., 2005). Again, there is good agreement between the positions of peaks in theory and experiment. The two experiments differ somewhat in the relative intensities of the divalent and trivalent parts. This could be an effect of different sample quality that influences the relative balance of the f^{13} and f^{12} configurations in the mixed valent ground state. A second possibility is a different surface sensitivity in the two experiments, combined with surface influence on the mixed valent ground state.

The theory presented here is not fully *ab initio* since it involves the adjustment of the chemical potential as well as the F^0 (or Hubbard U) parameter. The U parameter only enters in cases where three or more occupation numbers n of f^n configurations are involved, as is the case in the examples presented here. The size of multiplet splittings within a given configuration is solely determined by the $F^\ell(\ell > 0)$ parameters, which are calculated from the self consistent f partial wave, as the examples show with quite accurate results. Hence, screening effects do not enter as severely into the higher F^ℓ Slater integrals as they do for the Coulomb U parameter.

6.2 Relativistic theory of resonant X-ray scattering

MXRS is a well-developed technique for probing the magnetic and electronic structures of materials. The foundations of the theory of MXRS were laid down by Blume (1985). He showed that this spectroscopy is intrinsically relativistic. Later on Blume and Gibbs (1988) developed the theory further to show that the orbital and spin contributions to the magnetic moment can be measured separately using MXRS with a judicious choice of experimental geometry and polarization of the X-rays. This makes it a potentially very powerful spectroscopy. Integration of the SIC into the MXRS theory enables us to describe lanthanide and actinide materials on an equal footing with transition and simple materials. We then go further and make the connection between this theory and the standard theories of resonant X-ray scattering (Hill and McMorrow, 1996; Lovesey and Collins, 1996) and illustrate it with a calculation for the heavy lanthanides. In the relativistic SIC-LSD approach (Beiden et al., 1997), we adopt the same strategy as in the non-relativistic theory, but instead of Eq. (23), we have to solve the Dirac equation of the form

$$\left(\frac{c\hbar}{i}\boldsymbol{\alpha}\cdot\nabla + mc^2(\beta - I_4) + V^{\text{eff}}(\mathbf{r}) + \mu_B\beta\boldsymbol{\sigma}\cdot\mathbf{B}^{\text{eff}}(\mathbf{r}) + V_\gamma^{\text{SIC}}(\mathbf{r})\right)\psi_\gamma(\mathbf{r}) = \sum_{\gamma'}\lambda_{\gamma,\gamma'}\psi_{\gamma'}(\mathbf{r}), \tag{49}$$

where $\boldsymbol{\alpha}$ and β are Dirac matrices, $\mathbf{B}^{\text{eff}}$ is an effective magnetic field, σ_4 and I_4 are 4×4 spin operator and unit matrices, respectively, and $\lambda_{\gamma,\gamma'}$ is the Lagrange multipliers matrix. The SIC potential is given by

$$V_\gamma^{\text{SIC}}(\mathbf{r}) = -\left(\frac{e^2}{4\pi\varepsilon_0}\int\frac{n_\gamma(\mathbf{r}')}{|\mathbf{r}-\mathbf{r}'|}\mathrm{d}^3r' + \frac{\delta E_{\text{xc}}^{\text{LSD}}[\bar{n}_\gamma(\mathbf{r})]}{\delta n_\gamma(\mathbf{r})} - \mu_{\text{B}}\beta\boldsymbol{\sigma}_4\cdot\frac{\delta E_{\text{xc}}^{\text{LSD}}[\bar{n}_\gamma(\mathbf{r})]}{\delta\mathbf{m}_\gamma(\mathbf{r})}\right), \tag{50}$$

with γ denoting orbitals and

$$\mathbf{m}_\gamma(\mathbf{r}) \equiv -\mu_B\psi_\gamma^\dagger(\mathbf{r})\beta\boldsymbol{\sigma}_4\psi_\gamma(\mathbf{r}).$$

The task of finding the single particle-like wavefunctions is now in principle equivalent to that within non-relativistic SIC-LSD theory. The four-component nature of the wavefunctions and the fact that neither spin nor orbital angular momentum are conserved separately presents some added technical difficulty, but this can be overcome using well-known techniques (Strange et al., 1984). The formal first-principles theory of MXRS, for materials with translational periodicity, is based on the fully relativistic spin-polarized SIC-LSD method in conjunction with second-order time-dependent perturbation theory (Arola et al., 2004).

6.2.1 Basic theory of X-ray scattering

The theory of X-ray scattering is based on the second-order golden rule for the transition probability per unit time:

$$w_{\text{if}} = \frac{2\pi}{\hbar}\left|\langle f|\hat{H}'_{\text{int}}|i\rangle + \sum_I\frac{\langle f|\hat{H}'_{\text{int}}|I\rangle\langle I|\hat{H}'_{\text{int}}|i\rangle}{E_{\text{i}} - E_{\text{I}}}\right|^2\delta(E_{\text{f}} - E_{\text{i}}), \tag{51}$$

where $|i\rangle, |I\rangle$, and $|f\rangle$ are the initial, intermediate, and final states of the electron–photon system. E_i, E_I, and E_f are the corresponding energies. $\hat{\mathrm{H}}'_\mathrm{int}$ is the time-independent part of the photon–electron interaction Hamiltonian

$$\hat{H}_\mathrm{int}(t) = -e\int_\infty \hat{\psi}^\dagger(\mathbf{r},t)\boldsymbol{\alpha}\hat{\psi}(\mathbf{r},t)\cdot\hat{A}(\mathbf{r},t)\mathrm{d}^3r \tag{52}$$

where $\hat{A}(\mathbf{r},t)$ is the quantized radiation field operator, and $\hat{\psi}(\mathbf{r},t)$and $\hat{\psi}^\dagger(\mathbf{r},t)$ are the quantized Dirac field operators. The formalism to reduce Eq. (51) to single-electron-like form has been published previously (Arola et al., 1997). Therefore, we will not repeat the details here, but only the equations that are key to an understanding of the theory.

In relativistic quantum theory, it is the second term in Eq. (51) that is entirely responsible for scattering as it is second order in the vector potential. It is convenient to divide this term into four components, and the X-ray scattering amplitude in the case of elastic scattering may be written as (Arola et al., 1997; Arola and Strange, 2001)

$$\begin{aligned} f_{\mathbf{q}\lambda;\mathbf{q}'\lambda'}(\omega) &= \sum_{I,\varepsilon_\Lambda>0}\frac{\langle f|\hat{H}'_\mathrm{int}|I\rangle\langle I|\hat{H}'_\mathrm{int}|i\rangle}{E_i - E_I} - \sum_{I,\varepsilon_\Lambda>0}\frac{\langle f|\hat{H}'_\mathrm{int}|I\rangle\langle I|\hat{H}'_\mathrm{int}|i\rangle}{E_i - E_I} \\ &= f^{+(\mathrm{pos})}_{\mathbf{q}\lambda;\mathbf{q}'\lambda'}(\omega) + f^{-(\mathrm{pos})}_{\mathbf{q}\lambda;\mathbf{q}'\lambda'}(\omega) + f^{+(\mathrm{neg})}_{\mathbf{q}\lambda;\mathbf{q}'\lambda'}(\omega) + f^{-(\mathrm{neg})}_{\mathbf{q}\lambda;\mathbf{q}'\lambda'}(\omega), \end{aligned} \tag{53}$$

where $\mathbf{q}$, λ ($\mathbf{q}'$, λ') represent the wave vector and polarization of the incident (outgoing) photon. Two different terms arise, as the distinction in energy is made between $\varepsilon_\Lambda > 0$ and $\varepsilon_\Lambda < 0$ according to whether the intermediate states contain excitations from the 'negative-energy sea of electrons', that is the creation of electron–positron pairs. For both positive and negative energies, there are two separate types of intermediate states, $|I\rangle$, that is those containing no photons and those containing two photons, which altogether results in the four separate scattering amplitudes. In the energy range of interest, $\hbar\omega << 2mc^2$, three of these components (the latter three) have no resonance, and so will only make a contribution to the cross section that is slowly varying. In the following, we shall only be interested in scattering around resonance, and the corresponding expression for the scattering amplitude reduces to the component that is large and rapidly varying around resonance, namely

$$f_{\mathbf{q}\lambda;\mathbf{q}'\lambda'}(\omega) = f^{+\mathrm{pos}}_{\mathbf{q}\lambda;\mathbf{q}'\lambda'}(\omega) = -\sum_{\Lambda\Lambda'}\frac{\int \mathrm{d}^3r\, u^\dagger_\Lambda(\mathbf{r})X^\dagger_{\mathbf{q}'\lambda'}(\mathbf{r})u_{\Lambda'}(\mathbf{r})\int \mathrm{d}^3\mathrm{r}'u^\dagger_{\Lambda'}(\mathbf{r}')X_{\mathbf{q}\lambda}(\mathbf{r}')u_\Lambda(\mathbf{r}')}{\varepsilon_\Lambda - \varepsilon_{\Lambda'} + \hbar\omega} \tag{54}$$

where $u_\Lambda(\mathbf{r})$ and $\upsilon_\Lambda(\mathbf{r})$ are positive and negative energy electron eigenstates with quantum numbers Λ of the Dirac Hamiltonian for the crystal and form a complete orthonormal set of four-component basis functions in the Dirac space. The one-electron states are subject to the constraint that $\varepsilon_\Lambda \le \varepsilon_\mathrm{F}$ and $\varepsilon_{\Lambda'} > \varepsilon_\mathrm{F}$, where ε_F is the Fermi energy. The relativistic photon–electron interaction vertex is

$$X_{\mathbf{q}\lambda}(\mathbf{r}) = -e\left(\frac{\hbar c^2}{2V\varepsilon_0\omega}\right)^{1/2}\boldsymbol{\alpha}\cdot\hat{\varepsilon}^{(\lambda)}(\mathbf{q})e^{i\mathbf{q}\cdot\mathbf{r}}, \tag{55}$$

where $e = -|e|$, and $\hat{\varepsilon}^{(\lambda)}(\mathbf{q})$ is the polarization vector for the X-ray propagating in the direction of $\mathbf{q}$.

Equation (54) represents scattering with no photons and positive energy electrons only in the intermediate state. The corresponding theory is only applicable around resonance that makes it complementary to the work of Blume (1985), which is only valid well away from resonance.

The final expression for the resonant part of the scattering amplitude in Bragg diffraction is

$$f^{+(\text{pos})}_{\mathbf{q}\lambda;\mathbf{q}'\lambda'}(\omega) = f^{+(\text{pos})}_{0;\mathbf{q}\lambda;\mathbf{q}'\lambda'}(\omega) N_{\text{cells}} \delta_{\mathbf{QK}}, \tag{56A}$$

where N_{cells} stands for the number of unit cells, $\mathbf{K}$ is a reciprocal lattice vector, $\mathbf{Q} \equiv \mathbf{q}' - \mathbf{q}$, and the 0th unit cell contribution to the scattering amplitude is

$$\begin{aligned} f^{+(\text{pos})}_{0;\mathbf{q}\lambda;\mathbf{q}'\lambda'}(\omega) = \sum_j \frac{V}{(2\pi)^3} \int_{\mathbf{k}\in 1.\text{BZ}} \mathrm{d}^3k \sum_{t=1}^{N_{\text{type}}} \sum_{i=1}^{N_{\text{t}}} \sum_{\Lambda_{\text{t}}} e^{-i\mathbf{Q}\cdot\tau_i^{(\text{t})}} \\ \times \frac{m^{(ti)\,+\,j\mathbf{k}}_{\Lambda_{\text{t}}}(\mathbf{q}'\lambda') m^{(ti)\,+\,j\mathbf{k}^*}_{\Lambda_{\text{t}}}(\mathbf{q}\lambda)}{\varepsilon^{(t)}_{\Lambda_{\text{t}}} - \varepsilon^{j\mathbf{k}} + \hbar\omega + \Gamma^{(t)}_{\Lambda_{\text{t}}}/2} \theta\left(\varepsilon^{j\mathbf{k}} - \varepsilon_{\text{F}}\right). \end{aligned} \tag{56B}$$

Here j is the band index, N_{type} represents the number of different atom types and N_{t} is the number of atoms of each type. The matrix elements $m^{(ti)\,+\,jk}_{\Lambda_t}(\mathbf{q}\lambda)$ are given by

$$m^{(n)\,+\,j\mathbf{k}}_{\Lambda_n}(\mathbf{q}\lambda) \equiv \int_{S^n} \mathrm{d}^3 r_n u^{(n)\dagger}_{\Lambda_n}(\mathbf{r}_n) X^{\dagger}_{\mathbf{q}\lambda}(\mathbf{r}_n) \psi^{j\mathbf{k}}\left(\mathbf{R}^{(0)}_n + \mathbf{r}_n\right), \tag{56C}$$

where S^n refers to the nth atomic sphere within the unit cell. The added phenomenological parameter $\Gamma^{(t)}_{\Lambda_t}$ represents the natural width of the intermediate states created by the core hole state $|\Lambda_{\text{t}}\rangle$ at the t type basis atom.

Within the electric dipole approximation [$e^{i\mathbf{q}\cdot\mathbf{r}} \approx 1$ in Eq. (55)], the polarization can be taken outside the matrix elements and the scattering amplitude of Eq. (56B) can be written as

$$\begin{aligned} f^{+(\text{pos})}_{0;\mathbf{q}\lambda;\mathbf{q}'\lambda'}(\omega) = \sum_j \frac{V}{(2\pi)^3} \int_{\mathbf{k}\in 1.\text{BZ}} \mathrm{d}^3k \sum_{t=1}^{N_{\text{type}}} \sum_{i=1}^{N_{\text{t}}} \sum_{\Lambda_{\text{t}}} e^{-i\mathbf{Q}\cdot\tau_i^{(t)}} \\ \times \frac{\lambda' \cdot m^{(ti)\,+\,j\mathbf{k}}_{\Lambda_{\text{t}}}(\mathbf{q}') \lambda \cdot m^{(ti)\,+\,j\mathbf{k}^*}_{\Lambda_{\text{t}}}(\mathbf{q})}{\varepsilon^{(t)}_{\Lambda_{\text{t}}} - \varepsilon^{j\mathbf{k}} + \hbar\omega + \Gamma^{(t)}_{\Lambda_{\text{t}}}/2} \theta\left(\varepsilon^{j\mathbf{k}} - \varepsilon_{\text{F}}\right), \end{aligned} \tag{57}$$

where the scalar product is between the photon polarization and the Pauli spin matrices that appear within the matrix elements in this formulation. This equation can be reduced to a rather appealing form. Using the notation

$$Q_{+1} = \frac{1}{\sqrt{2}}\left(Q_x + iQ_y\right) \quad Q_0 = Q_z \quad Q_{-1} = \frac{1}{\sqrt{2}}\left(Q_x - iQ_y\right) \tag{58}$$

the numerator in Eq. (57) can be written as

$$
\begin{aligned}
\left(\lambda'\cdot m_{\Lambda_t}^{(ti)\,+\,j\mathbf{k}}\right)\left(\lambda\cdot m_{\Lambda_t}^{(ti)\,+\,j\mathbf{k}^*}\right) &= \sum_{v=0,\pm 1} \lambda'_v\lambda_v\left|m_{v\Lambda_t}^{(ti)\,+\,j\mathbf{k}}\right|^2 \\
&= \frac{1}{2}\Big[(\lambda'\cdot\lambda)\left(\left|m_{+\,1\Lambda_t}^{(ti)\,+\,j\mathbf{k}}\right|^2 + \left|m_{-1\Lambda_t}^{(ti)\,+\,j\mathbf{k}}\right|^2\right) \\
&\quad + i m_z\cdot(\lambda'\times\lambda)\left(\left|m_{-1\Lambda_t}^{(ti)\,+\,j\mathbf{k}}\right|^2 - \left|m_{+1\Lambda_t}^{(ti)\,+\,j\mathbf{k}}\right|^2\right) \\
&\quad + (\lambda'\cdot m_z)(\lambda\cdot m_z)\left(2\left|m_{0\Lambda_t}^{(ti)\,+\,j\mathbf{k}}\right|^2\right. \\
&\quad \left.-\left|m_{+1\Lambda_t}^{(ti)\,+\,j\mathbf{k}}\right|^2 - \left|m_{-1\Lambda_t}^{(ti)\,+\,j\mathbf{k}}\right|^2\right)\Big],
\end{aligned}
\tag{59}
$$

where m_z is a unit vector in the direction of the magnetization. The advantage of a formulation of the scattering amplitude in these terms is that the geometry of the experiment is separated from the matrix elements and other atomic level information. It is possible to choose a geometry such that only one of the three terms in Eq. (59) is non-zero. For example, if we have π–π scattering with 90° between the incident and outgoing beam, the first term is zero. If the magnetization points at 90° to both the incident and outgoing polarizations, then the third term is zero and only the second term remains. This cancellation was exploited in Brown et al. (2007) in the investigation of magnetism in lanthanide elements (see below). Furthermore, if a spherical approximation is made for the electronic structure, the matrix elements can be calculated as a function of energy just once and all the angular dependence of the scattering is in the polarization and m_z dependence.

In the LMTO implementation, the resonant matrix element $m_{\Lambda_t}^{(ti)\,+\,j\mathbf{k}}(\mathbf{q}\lambda)$ can be written as

$$
m_{\Lambda_t}^{(ti)\,+\,j\mathbf{k}}(\mathbf{q}\lambda) = \sum_{\Lambda}\left[A_{ti\Lambda}^{j\mathbf{k}}\left(u_{\Lambda_t}^{(t)}|X_{\mathbf{q}\lambda}^{\dagger}|\phi_{vt\Lambda}\right) + B_{ti\Lambda}^{j\mathbf{k}}\left(u_{\Lambda_t}^{(t)}|X_{\mathbf{q}\lambda}^{\dagger}|\dot{\phi}_{vt\Lambda}\right)\right],
\tag{60A}
$$

where A and B are the wavefunction coefficients of the LMTO-ASA wavefunction (Skriver, 1983a) and $(f|X_{\mathbf{q}\lambda}^{\dagger}|g)$ is defined as

$$
(f|X_{\mathbf{q}\lambda}^{\dagger}|g) \equiv \int_{S^t} \mathrm{d}^3 r f^{\,\dagger}(\mathbf{r}) X_{\mathbf{q}\lambda}^{\dagger}(\mathbf{r}) g(\mathbf{r}),
\tag{60B}
$$

with $f \equiv u_{\Lambda_t}^{(t)}$ and $g \equiv \phi_{vt\Lambda}$ or $\dot{\phi}_{vt\Lambda}$

While the cross section is the fundamental measurable quantity in scattering theory, it is frequently more convenient in X-ray scattering from magnetic materials to measure the asymmetry ratio (dichroism). This is defined as the difference divided by the sum of the cross section for the moment in one direction and the moment in the opposite direction.

$$
A(\mathbf{q};\mathbf{q}'\lambda;\omega) \equiv \frac{\omega_{d\Omega}(\mathbf{q}+;\mathbf{q}'\lambda';\omega) - \omega_{d\Omega}(\mathbf{q}-;\mathbf{q}'\lambda';\omega)}{\omega_{d\Omega}(\mathbf{q}+;\mathbf{q}'\lambda';\omega) + \omega_{d\Omega}(\mathbf{q}-;\mathbf{q}'\lambda';\omega)}
\tag{61}
$$

where the scattering rate $\omega_{d\Omega}$ into a solid space angle $d\Omega$ can be written in terms of the scattering amplitude $f_{\mathbf{q}\lambda;\mathbf{q}'\lambda'}(\omega)$ as

$$
\omega_{d\Omega} = \frac{2\pi}{\hbar}\left|f_{\mathbf{q}\lambda;\mathbf{q}'\lambda'}(\omega)\right|^2 \frac{V}{(2\pi)^3}\frac{\omega^2}{\hbar c^3}\,d\Omega
\tag{62}
$$

As shown by Lovesey and Collins (1996), the asymmetry ratio directly reflects the scattering amplitude rather than the cross section and emphasizes the interference between magnetic scattering and charge scattering.

6.2.2 Application to lanthanides

As discussed previously, the SIC-LSD method has been used successfully to describe properties of lanthanide materials that cannot be described within the bare LDA (Strange et al., 1999). Here we look at how SIC-LSD describes resonant X-ray scattering. An important point made in the paper of Arola et al. (2004) is that the spectra are dependent on the number and symmetry of the localized states and intermediate states. Therefore, this spectroscopy could become quite important for the unravelling of the nature of the localized states.

Calculations of the asymmetry ratio for the heavy lanthanide metals have been carried out by Brown et al. (2007). They have shown that the asymmetry ratio consists of two features. There is a major peak in the asymmetry ratio that is predominantly due to dipolar scattering from the magnetic moment of the 5d states, and a smaller feature (below the elemental absorption edge) which in their experiment is also dipolar but in general is due to a mixture of dipolar and quadrupolar scattering. These features are labelled *A* and *B*, respectively, in Figure 29. Feature B remains more or less in the same place relative to the absorption edge as we proceed along the lanthanide series whereas feature A gradually moves higher above the absorption edge. This means that these features separate and feature B changes from being a shoulder on the side of feature A to a separate peak. Note also the inversion of feature A in Tm. This is related to the fact that the d-electrons couple anti-ferromagnetically to the f-electrons in Tm, but ferromagnetically in the other heavy lanthanides. Obviously the data in Figure 29 are providing information about the details of the electronic structure of the lanthanides. In Figure 30, we present the 5d electron spin moment (left panel) and orbital moment (right panel) of the heavy lanthanides as a function of energy. As expected in the left panel, a lower energy peak is representing the majority spin states and a higher peak is representing the minority spin states. Features A and B from Figure 29 are also shown. It is clear that feature A in the scattering corresponds to the peak in the 5d minority spin states. Feature B does not correspond exactly to anything in the spin moment although it is fairly close in energy to the maximum in the majority spin moment as a function of energy. If we look at the right panel, the magnitude of the 5d orbital moment is generally small, although for Er and Tm, it does become comparable to the spin moments. Clearly feature A has no correspondence with the orbital moment whereas feature B is close to a peak in the orbital moment. It is clear then that feature A arises from scattering from the empty spin states anti-parallel to the f spin moments whereas feature B represents scattering from both the orbital and spin moments parallel to the f spin moment. The correlation of peaks A and B in Figure 29, with the structure in Figure 30, demonstrates that the dipolar asymmetry ratios at the L_{III} edges reflect the progression from spin-dominated Gd to orbital-dominated Er and Tm electronic structure.

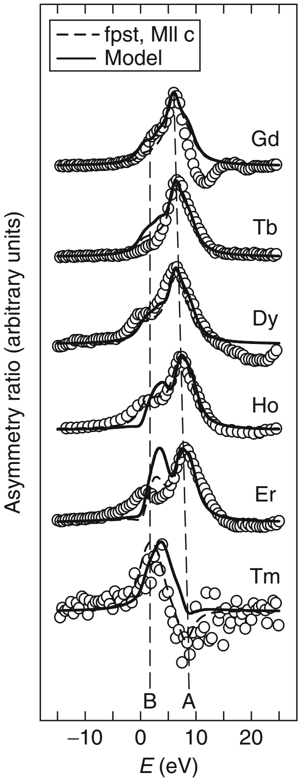

FIGURE 29 The asymmetry ratio of the lanthanides Gd through to Tm after Brown et al. (2007). The circles represent the experimental results measured on the XMaS beamline at the ESRF. The dashed line represents the full first-principles theory outlined in this section and yields at least good qualitative agreement with experiment. The full line is a simple model calculation that neglects all matrix elements and bases the asymmetry ratio on the DOS calculated using SIC-LSD theory. Note the features A and B that are discussed in the text.

7. FINITE TEMPERATURE PHASE DIAGRAMS

7.1 Thermal fluctuations

Up to now, we have concentrated on the physics at zero kelvin. In this section, we extend the studies to finite temperatures and discuss finite temperature phase diagrams. The physics at finite temperatures is dominated by thermal fluctuations between low lying excited states of the system. These fluctuations can include spin fluctuations, fluctuations between different valence states, or fluctuations between different orbitally ordered states, if present. Such fluctuations can be addressed through a so-called 'alloy analogy'. If there is a timescale that is slow compared to the motion of the valence electrons, and on which the configurations persist between the system fluctuations, one can replace the temporal average over all fluctuations by an ensemble average over all possible (spatially

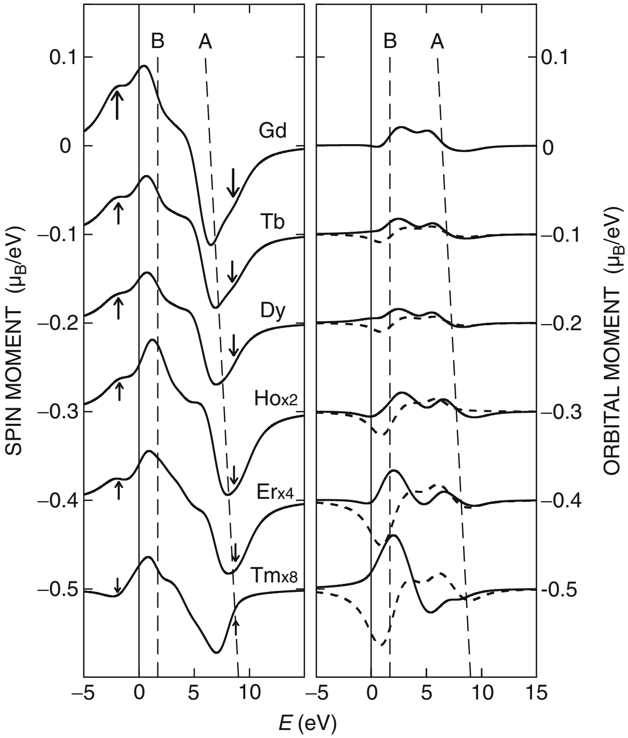

FIGURE 30 The spin and orbital moments associated with the 5d states in the heavy lanthanide metals after Brown et al. (2007). (A) The spin moment. The arrows on the left-hand side represent the coupling to the empty f-states above E_F. The zero of energy on this scale is the Fermi energy. Also shown are features A and B from Figure 29. (B) The orbital moment of the 5d states. As expected, this quantity is generally small, although it becomes comparable with the spin moment in Er and Tm. The dashed line represents the case when the f-states are filled according to Hund's rules and the full line when they are filled directly opposite to Hund's rules.

disordered) configurations of the system. In the following text, we will explain this procedure in detail for the treatment of spin fluctuations, which leads to the well-known DLM theory of finite temperature magnetism. After that, the same methodology is applied to different valence configurations and demonstrated on the example of the finite temperature phase diagram of Ce.

This static alloy analogy picture should be a good description as long as there is a separation of timescales. If this breaks down, dynamical fluctuations—or quantum fluctuations—which are beyond this static picture, become important. These quantum fluctuations are the main emphasis of DMFT (Georges et al., 1996), which maps the system onto an effective Anderson impurity model, describing a dynamically fluctuating impurity in a self-consistently determined effective host. So far, DMFT has been formulated for model Hamiltonians, such as the Hubbard model, and material-specific results have been achieved by constructing these model Hamiltonians from realistic band structure calculations. In the context of model Hamiltonians, it has been shown (Kakehashi, 2002) that DMFT is equivalent to a dynamical CPA. Hence, the static CPA approach, presented here, corresponds to the static limit of a, still to be developed, fully *ab initio* version of DMFT. A discussion on how such a theory could be constructed is given in Section 8.

7.2 Spin fluctuations: DLM picture

For low temperatures, calculations of the characteristics of the free energy (ground state energy) of a magnetic material are all based on an electronic band structure for a given configuration, such as a fixed spin-polarization, for example a uniform spin-polarization for a ferromagnet and fixed sublattice spin polarizations for an anti-ferromagnet, a given valence state, or, if present, a given orbital order. With increasing temperature, fluctuations between those configurations are induced that eventually destroy the long-range order. These collective electron modes interact as the temperature is raised and are dependent upon and affect the underlying electronic structure. In this and the following sections, we concentrate on magnetic order and magnetic excitations through spin fluctuations. For many materials, the magnetic excitations can be modelled by associating local spin-polarization axes with all lattice sites and the orientations vary very slowly on the timescale of the electronic motions (Moriya, 1981). These 'local moment' degrees of freedom produce local magnetic fields on the lattice sites that affect the electronic motions and are self-consistently maintained by them. By taking appropriate ensemble averages over the orientational configurations, the system's magnetic properties can be determined. The DLM DFT-based theory has been developed and used in this context to describe the onset and type of magnetic order *ab initio* in many magnetic systems (Gyorffy et al., 1985; Staunton et al., 1985; Staunton and Gyorffy, 1992). Moreover, the recent inclusion of relativistic effects into DLM theory produces an *ab initio* description of the temperature dependence of magnetic anisotropy of metallic ferromagnets, which agrees well with experimental results and deviates qualitatively from simple, widely used models (Staunton et al., 2004, 2006). It is the incorporation of the LSIC method for describing strongly correlated electrons into the DLM theory that we focus on in this section and its application to the magnetic structure of Gd and other heavy lanthanide systems. The standard model of lanthanide electronic structure gives a good qualitative description of the formation and magnitude of the magnetic moments. It has long been understood that these local moments, formed predominantly by the localized f-electrons, interact with each other by spin-polarizing the sea of conduction electrons in which they sit. The RKKY interaction is the simplest example of this effect. As we will show, our DLM-LSIC theory gives a quantitative *ab initio* description of this physics.

In principle, the extension of electronic DFT to finite temperatures was carried out by Mermin (1965) soon after the pioneering papers of Hohenberg, Kohn, and Sham (Hohenberg and Kohn, 1964; Kohn and Sham, 1965). The single-particle entropy is included and the effective one-electron fields involve Ω_{xc}, the exchange-correlation part of the Gibbs free energy functional of particle and magnetization densities. Formally, this can be expressed in terms of spin-dependent pair correlation functions $g_\lambda(\sigma, \sigma'; \mathbf{r}, \mathbf{r}')$, that is

$$\Omega_{\text{xc}}[n, \mathbf{m}] = \frac{e^2}{2}\int_0^1 \mathrm{d}\lambda \int \mathrm{d}^3 r \int \mathrm{d}^3 r' \sum_{\sigma,\sigma'} \frac{n_\sigma(\mathbf{r}) n_{\sigma'}(\mathbf{r}')}{|\mathbf{r}-\mathbf{r}'|} g_\lambda(\sigma, \sigma'; \mathbf{r}, \mathbf{r}') \tag{63}$$

where $n_\sigma(\mathbf{r})$ is the spin resolved charge density.

It would seem logical then simply to make the finite temperature extension of the LDA (or GGA) that is successfully exploited in applications on the ground state of magnetic materials in conjunction with, say, the SIC, to deal with localized states where appropriate. So, for example, $\Omega_{\text{xc}}[n, \mathbf{m}]$ is replaced by $\int \mathrm{d}^3 r n(\mathbf{r}) \Omega^0_{\text{xc}}(n(\mathbf{r}))$ where Ω^0_{xc} is the exchange-correlation part of the Gibbs free energy of a homogeneous electron gas. This assumption allows the thermally averaged magnetization, $\overline{\text{M}}$, along with the spin splitting of the electronic structure to decrease only by the excitation of particle-hole, 'Stoner' excitations across the Fermi surface. However, it severely underestimates the effects of the thermally induced spin-wave excitations. For lanthanide materials, these orientational magnetic fluctuations are entirely neglected, whereas in transition metal ferromagnets, the reliance on Stoner particle-hole excitations causes the calculated Curie temperatures to be typically an order of magnitude too high with no obvious mechanism for the Curie-Weiss behaviour of the uniform static paramagnetic susceptibility found for many metallic systems.

Evidently, part of the pair correlation function $g_\lambda(\sigma, \sigma'; \mathbf{r}, \mathbf{r}')$ should be related by the fluctuation dissipation theorem to the magnetic susceptibilities harbouring information about spin waves. These spin fluctuations interact as temperature is increased and so Ω_{xc} $[n, \mathbf{m}]$ should deviate significantly from the local approximation with a consequent impact upon the form of the effective single electron states. Indeed, accounts of modern electronic structure theory for magnetic systems (Staunton, 1994; Kübler, 2000) have large sections devoted to work that is concerned with the modelling of spin fluctuation effects while maintaining the spin-polarized single electron basis.

Most of this work is based on a rather simple, pervasive picture of fluctuating 'local moments' that stems from the belief of a timescale separation of the electronic degrees of freedom. A conduction electron (in a lanthanide material) travels from site to site on a much faster timescale than that of the collective spin wave motion. So the dominant thermal fluctuation of the magnetization that the straightforward finite temperature extension of spin-polarized band theory misses can be pictured quite simply as orientational fluctuations of 'local moments'. These entities are the magnetizations within each unit cell of the underlying crystal lattice that are largely determined by the localized f-electrons in the lanthanides, while in itinerant electron transition metal magnets, they are set up by the collective behaviour of all the electrons. Their orientations persist on timescales long compared to electronic 'hopping' times. At low temperatures, their long wavelength, slow spin wave dynamics can be directly extracted from the transverse part of the magnetic susceptibility. At higher temperatures, the more complex behaviour can be described with a classical treatment. The energy is considered of the many interacting electron system constrained to have a set inhomogeneous magnetization profile. From atomic site to atomic site, the local magnetic moments are oriented along prescribed directions, that is producing a 'local moment' configuration. Averages over such orientational configurations are subsequently taken to determine the equilibrium properties of the system. $\overline{\mathrm{M}}$ can now vanish as the disorder of the 'local moments' grows. There remains, however, the issue as to which fluctuations are the most important.

Formally DFT (Gyorffy et al., 1985) is used to specify the 'generalized' grand potential, $\Omega^{(\hat{n})}(\{\hat{e}\})$, of an interacting electron system which is constrained in such a way that the site by site spin polarization axes are configured according to $\{\hat{e}\} = \{\hat{e}_1, \hat{e}_{2,\ldots,}\hat{e}_N\}$, where N is the number of sites (moments) in the system. The $\{\hat{e}\}$, classical unit vectors, are thus the degrees of freedom describing the local moment orientations and $\Omega^{(\hat{n})}(\{\hat{e}\})$ is the 'local moment' Hamiltonian. (With relativistic effects such as spin-orbit coupling included, the temperature dependence of magnetic anisotropy can be described. This means that orientations of the local moments with respect to a specified direction $\hat{n}$ within the material are relevant.)

One way forward from this point is to carry out calculations of $\Omega^{(\hat{n})}(\{\hat{e}\})$ for a selection of configurations ('spin' spirals, two impurities in a ferromagnet, magnetically ordered supercells, etc.) by making some assumptions about the most dominant fluctuations. One then fits the set of $\Omega^{(\hat{n})}(\{\hat{e}\})$'s to a simple functional form. Typically a classical Heisenberg model, $\Omega^{(\hat{n})}(\{\hat{e}\}) = -1/2\sum_{ij} J_{ij}\hat{e}_i \cdot \hat{e}_j$ is set up and various statistical mechanics methods (e.g., Monte Carlo) are used to produce the desired thermodynamic averages. Many useful studies have been carried out in this way but there is a risk that a bias is produced so that some of the physics is missed. The spin-polarized electronic structures of the restricted set of constrained systems are not guaranteed to generate magnetic correlations that are consistent with the chosen sampling of the orientational configurations. In other words, the electronic and magnetic structures are not necessarily mutually consistent. In the following, we summarize the main points of our DLM theory which avoids these problems. Full details can be found in references Gyorffy et al. (1985), Staunton et al. (1985), and Staunton and Gyorffy (1992) and relativistic extension in references Staunton et al. (2004, 2006).

The DLM picture is implemented within a multiple-scattering formalism (KKR) (Korringa, 1947; Kohn and Rostoker, 1954; Stocks et al., 1978; Stocks and Winter, 1982; Johnson et al., 1986). Some applications include the description of the experimentally observed local exchange splitting and magnetic short-range order in both ultrathin Fe films (Razee et al., 2002) and bulk Fe (Gyorffy et al., 1985; Staunton et al., 1985), the damped RKKY-like magnetic interactions in the compositionally disordered CuMn 'spin-glass' alloys (Ling et al., 1994), and the onset of magnetic order in a range of alloys (Staunton et al., 1997; Crisan et al., 2002). By combining it with the LSIC (Lüders et al., 2005) for strong electron correlation effects, we have recently used it to account quantitatively for the magnetic ordering in the heavy lanthanides (Hughes et al., 2007). This gives an *ab initio* account of the well-known picture of f-electron magnetic moments interacting via the conduction electrons.

We consider a collinear magnetic system magnetized with reference to a single direction $\hat{n}$ at a temperature T. (A non-collinear generalization can be made by making the notation more complicated.) The orientational probability distribution is denoted by $P^{(\hat{n})}(\{\hat{e}\})$, and its average for a lattice site i,

$$\langle \hat{e}_i \rangle = \int \ldots \int \hat{e}_i P^{(\hat{n})}(\{\hat{e}\}) \mathrm{d}\hat{e}_1 \ldots \mathrm{d}\hat{e}_N = m\hat{n}, \tag{64}$$

is aligned with the magnetization direction $\hat{n}$. The canonical partition function and the probability function are defined as $Z^{(\hat{n})} = \int \ldots \int e^{-\beta\Omega^{(\hat{n})}(\{\hat{e}\})} \mathrm{d}\hat{e}_1 \ldots \mathrm{d}\hat{e}_N$ and $P^{(\hat{n})}(\{\hat{e}\}) = e^{-\beta\Omega^{(\hat{n})}(\{\hat{e}\})}/Z^{(\hat{n})}$, respectively. The thermodynamic free energy that includes the entropy associated with the orientational fluctuations as well as creation of electron-hole pairs is given by $F^{(\hat{n})} = -1/\beta\left(\ln Z^{(\hat{n})}\right)$. By choosing a trial Hamiltonian function, $\Omega_0^{(\hat{n})}(\{\hat{e}\})$ with

$$Z_0^{(\hat{n})} = \int \ldots \int e^{-\beta\Omega_0^{(\hat{n})}(\{\hat{e}\})} \mathrm{d}\hat{e}_1 \ldots \mathrm{d}\hat{e}_N, \tag{65}$$

$$P_0^{(\hat{n})}(\{\hat{e}\}) = \frac{e^{-\beta\Omega_0^{(\hat{n})}(\{\hat{e}\})}}{Z_0^{(\hat{n})}}, \tag{66}$$

and $F_0^{(\hat{n})} = -1/\beta(\ln Z_0^{(\hat{n})})$, the *Feynman-Peierls Inequality* (Feynman, 1955) implies an upper bound for the free energy, that is,

$$F^{(\hat{n})} \le F_0^{(\hat{n})} + \langle \Omega^{(\hat{n})} - \Omega_0^{(\hat{n})} \rangle^0, \tag{67}$$

where the average refers to the probability $P_0^{(\hat{n})}(\{\hat{e}\})$. By expanding $\Omega_0^{(\hat{n})}(\{\hat{e}\})$ as

$$\Omega_0^{(\hat{n})}(\{\hat{e}\}) = \sum_i \omega_i^{1(\hat{n})}(\hat{e}_i) + \frac{1}{2}\sum_{i \neq j} \omega_{i,j}^{2(\hat{n})}(\hat{e}_i, \hat{e}_j) + \ldots, \tag{68}$$

the 'best' trial system is found to satisfy (Gyorffy et al., 1985; Staunton and Gyorffy, 1992)

$$\langle \Omega^{(\hat{n})} \rangle_{\hat{e}_i}^0 - \langle \Omega^{(\hat{n})} \rangle^0 = \langle \Omega_0^{(\hat{n})} \rangle_{\hat{e}_i}^0 - \langle \Omega_0^{(\hat{n})} \rangle^0, \tag{69}$$

$$\langle \Omega^{(\hat{n})} \rangle_{\hat{e}_i,\hat{e}_j}^0 - \langle \Omega^{(\hat{n})} \rangle^0 = \langle \Omega_0^{(\hat{n})} \rangle_{\hat{e}_i,\hat{e}_j}^0 - \langle \Omega_0^{(\hat{n})} \rangle^0, \tag{70}$$

and so on, where $\langle\rangle_{\hat{e}_i}or\langle\rangle_{\hat{e}_i,\hat{e}_j}$ denote restricted statistical averages with $\hat{e}_i$ or both $\hat{e}_i$ and $\hat{e}_j$ kept fixed, respectively. (In the following, we shall omit the superscript 0 from the averages.)

If we set $\Omega_0^{(\hat{n})}(\{\hat{e}\})$ as a sum of mean field Weiss terms, namely

$$\Omega_0^{(\hat{n})}(\{\hat{e}\}) = \sum_i \vec{h}_i^{(\hat{n})} \cdot \hat{e}_i, \tag{71}$$

where $\vec{h}_i^{(\hat{n})} = h_i^{(\hat{n})}\hat{n}$ with

$$h_i^{(\hat{n})} = \int \frac{3}{4\pi} (\hat{e}_i \cdot \hat{n}) \langle \Omega^{(\hat{n})} \rangle_{\hat{e}_i} \mathrm{d}\hat{e}_i, \tag{72}$$

the probability distribution factorizes as

$$P_0^{(\hat{n})}(\{\hat{e}_i\}) = \prod_i P_i^{(\hat{n})}(\hat{e}_i) \tag{73}$$

with

$$P_i^{(\hat{n})}(\hat{e}_i) = \frac{\exp\left(-\beta \vec{h}_i^{(\hat{n})} \cdot \hat{e}_i\right)}{Z_i^{(\hat{n})}} = \frac{\beta h_i^{(\hat{n})}}{4\pi \sinh \beta h_i^{(\hat{n})}} \exp\left(-\beta \vec{h}_i^{(\hat{n})} \cdot \hat{e}_i\right). \tag{74}$$

The average alignment of the local moments, proportional to the magnetization, is

$$\vec{m}_i^{(\hat{n})} = \int \hat{e}_i P_i^{(\hat{n})}(\hat{e}_i) \mathrm{d}\hat{e}_i = m_i^{(\hat{n})} \hat{n} \tag{75}$$

and

$$m_i^{(\hat{n})} = -\frac{\mathrm{d} \ln Z_i^{(\hat{n})}}{\mathrm{d}\left(\beta h_i^{(\hat{n})}\right)} = \frac{1}{\beta h_i^{(\hat{n})}} - \coth \beta h_i^{(\hat{n})} = L\left(-\beta h_i^{(\hat{n})}\right) \tag{76}$$

follows, where $L(x)$ is the Langevin function. Moreover, the free energy of the system is

$$F^{(\hat{n})} = \langle \Omega^{(\hat{n})} \rangle + \frac{1}{\beta} \sum_i \int P_i^{(\hat{n})}(\hat{e}_i) \ln P_i^{(\hat{n})}(\hat{e}_i) \mathrm{d}\hat{e}_i. \tag{77}$$

Another way of writing the Weiss field is (Gyorffy et al., 1985)

$$h_i^{(\hat{n})} = S_i^{1,(\hat{n})} = \frac{\partial \langle \Omega^{(\hat{n})} \rangle}{\partial m_i^{(\hat{n})}}. \tag{78}$$

Using Eqs. (74) and (76), this is shown to be equivalent to solving the equation of state

$$\frac{\partial F^{(\hat{n})}}{\partial m_i^{(\hat{n})}} = 0. \tag{79}$$

7.2.1 The role of the CPA

The averaging over local moment configurations is conveniently carried out using CPA technology (Soven, 1967; Stocks et al., 1978; Stocks and Winter, 1982; Johnson et al., 1986). The electronic charge density and also the magnetization density, which sets the magnitudes, $\{\mu\}$, of the local moments, are determined from an SCF-KKR-CPA (Stocks and Winter, 1982; Johnson et al., 1986) calculation. For a given set of (self-consistent) potentials, electronic charge and local moment magnitudes, the orientations of the local moments are accounted for by the similarity transformation of the single-site t-matrices (Messiah, 1965),

$$\underline{t}_i(\hat{e}_i) = \underline{R}(\hat{e}_i) \underline{t}_i(\hat{z}) \underline{R}(\hat{e}_i)^+ , \tag{80}$$

where for a given energy (not labelled explicitly), $\underline{t}_i(\hat{z})$ stands for the t-matrix with effective field pointing along the local z-axis (Strange et al., 1984) and $\underline{R}(\hat{e}_i)$ is a unitary representation of the $O(3)$ transformation that rotates the z axis along $\hat{e}_i$.

The CPA determines an effective medium through which the motion of an electron mimics the motion of an electron *on the average*. In a system magnetized with reference to a direction $\hat{n}$, the medium is specified by t-matrices, $\underline{t}^{(\hat{n})}_{i,c}$, which satisfy the condition (Stocks et al., 1978),

$$\langle \underline{\tau}^{(\hat{n})}_{ii}(\{\hat{e}\})\rangle = \int \langle \underline{\tau}^{(\hat{n})}_{ii}\rangle_{\hat{e}_i} P^{(\hat{n})}_i(\hat{e}_i)\mathrm{d}\hat{e}_i = \underline{\tau}^{(\hat{n})}_{ii,c}, \tag{81}$$

where the site-diagonal matrices of the multiple scattering path operator (Gyorffy and Stott, 1973) are defined as,

$$\langle \underline{\tau}^{(\hat{n})}_{ii}\rangle_{\hat{e}_i} = \underline{\tau}^{(\hat{n})}_{ii,c}\underline{D}^{(\hat{n})}_i(\hat{e}_i), \tag{82}$$

with the CPA projector

$$\underline{D}^{(\hat{n})}_i(\hat{e}_i) = \left(\underline{1} + \left[(\underline{t}_i(\hat{e}_i))^{-1} - \left(\underline{t}^{(\hat{n})}_{i,c}\right)^{-1}\right]\underline{\tau}^{(\hat{n})}_{ii,c}\right)^{-1}, \tag{83}$$

and

$$\underline{\underline{\tau}}^{(\hat{n})}_c = ((\underline{\underline{t}}^{(\hat{n})}_c)^{-1} - \underline{\underline{G}}_0)^{-1}. \tag{84}$$

Equation (81) can be rewritten in terms of the excess scattering matrices,

$$\underline{X}^{(\hat{n})}_i(\hat{e}_i) = \left(\left[\left(\underline{t}^{(\hat{n})}_{i,c}\right)^{-1} - (\underline{t}_i(\hat{e}_i))^{-1}\right]^{-1} - \underline{\tau}^{(\hat{n})}_{ii,c}\right)^{-1}, \tag{85}$$

in the form

$$\int \underline{X}^{(\hat{n})}_i(\hat{e}_i)P^{(\hat{n})}_i(\hat{e}_i)\mathrm{d}\hat{e}_i = \underline{0}. \tag{86}$$

Thus, for a given set of Weiss fields, $h^{(\hat{n})}_i$, and corresponding probabilities, $P^{(\hat{n})}_i(\hat{e}_i)$, Eq.(86) can be solved by iterating together with Eqs. (85) and (84) to obtain the matrices, $\underline{t}^{(\hat{n})}_{i,c}$ (Staunton et al., 2006).

Using the magnetic force theorem, the single-particle energy part of the DFT grand potential gives

$$\Omega^{(\hat{n})}(\{\hat{e}\}) \simeq -\int \mathrm{d}\varepsilon\, f_\beta\left(\varepsilon; \nu^{(\hat{n})}\right)N^{(\hat{n})}(\varepsilon; \{\hat{e}\}), \tag{87}$$

as an effective 'local moment' Hamiltonian, where $\nu^{(\hat{n})}$ is the chemical potential, $f_\beta(\varepsilon; \nu^{(\hat{n})})$ is the Fermi-Dirac distribution, and $N^{(\hat{n})}(\varepsilon; \{\hat{e}\})$ denotes the integrated DOS for the orientational configuration, $\{\hat{e}\}$. From the Lloyd formula (Lloyd and Best, 1975),

$$N^{(\hat{n})}(\varepsilon; \{\hat{e}\}) = N_o(\varepsilon) - \frac{1}{\pi}\mathrm{Im}\ \ln\ \det\left(\underline{\underline{t}}^{(\hat{n})}(\varepsilon; \{\hat{e}\})^{-1} - \underline{\underline{G}}_0(\varepsilon)\right), \tag{88}$$

[$N_0(\varepsilon)$ being the integrated DOS of the free particles] and properties of the CPA effective medium, the partially averaged electronic Grand Potential is given by

$$\begin{aligned}\langle\Omega^{(\hat{n})}\rangle_{\hat{e}_i} = &-\int \mathrm{d}\varepsilon\, f_\beta\left(\varepsilon;\nu^{(\hat{n})}\right)N_c^{(\hat{n})}(\varepsilon)\\ &+\frac{1}{\pi}\int \mathrm{d}\varepsilon\, f_\beta\left(\varepsilon;\nu^{(\hat{n})}\right)\mathrm{Im}\,\ln\,\det\underline{M}_i^{(\hat{n})}(\varepsilon;\hat{e}_i)\\ &+\sum_{j\neq i}\frac{1}{\pi}\int \mathrm{d}\varepsilon\, f_\beta\left(\varepsilon;\nu^{(\hat{n})}\right)\mathrm{Im}\langle\ln\,\det\underline{M}_j^{(\hat{n})}(\varepsilon;\hat{e}_j)\rangle,\end{aligned} \tag{89}$$

and the Weiss field, $h_i^{(\hat{n})}$, can be expressed, using Eq. (72), as

$$h_i^{(\hat{n})} = \frac{3}{4\pi}\int(\hat{e}_i\cdot\hat{n})\left[\int \mathrm{d}\varepsilon\, f_\beta\left(\varepsilon;\nu^{(\hat{n})}\right)\frac{1}{\pi}\mathrm{Im}\,\ln\,\det\underline{M}_i^{(\hat{n})}(\varepsilon;\hat{e}_i)\right]\mathrm{d}\hat{e}_i, \tag{90}$$

where

$$\underline{M}_i^{(\hat{n})}(\varepsilon;\hat{e}_i) = \left(\underline{1} + \left[(\underline{t}_i(\hat{e}_i))^{-1} - \left(\underline{t}_{i,\mathrm{c}}^{(\hat{n})}\right)^{-1}\right]\underline{\tau}_{ii,\mathrm{c}}^{(\hat{n})}\right)\ \text{and}$$
$$N_\mathrm{c}^{(\hat{n})}(\varepsilon) = -\frac{1}{\pi}\mathrm{Im}\,\ln\,\det\left(\underline{\underline{t}}_\mathrm{c}^{(\hat{\mathrm{n}})}(\varepsilon)^{-1} - \underline{\underline{\mathrm{G}}}_0(\varepsilon)\right).$$

The solution of Eqs. (90) and (76) produces the variation of the magnetization $m_i^{(\hat{n})}$ with temperature T with $m_i^{(\hat{n})}$ going to zero at $T = T_\mathrm{c}^{(\hat{n})}$.

7.2.2 The paramagnetic DLM state

The paramagnetic state is given by the Weiss fields being zero so that the probabilities, $P_i^{(\hat{n})} = 1/4\pi$, and on any site, a moment has an equal chance of pointing in any direction. This means the magnetizations, $m_i^{(\hat{n})}$, vanish. The magnetic transition temperature, onset, and type of magnetic order can be extracted by studying the effects of a small inhomogeneous magnetic field on this high T paramagnetic state (Gyorffy et al., 1985; Staunton et al., 1985; Staunton and Gyorffy, 1992).

When relativistic spin-orbit coupling effects are omitted, the single-site matrix $\tilde{t}(\hat{e}_i)$ describing the scattering from a site with local moment orientated in the direction $\hat{e}_i$ becomes

$$\tilde{t}_i = \frac{1}{2}(t_+ + t_-)\tilde{1} + \frac{1}{2}(t_+ - t_-)\tilde{\sigma}\cdot\hat{e}_i, \tag{91}$$

where $\tilde{\sigma}_x, \tilde{\sigma}_y$, and $\tilde{\sigma}_z$ are the three Pauli spin matrices defined according to the global z-axis. In the local reference frame, where the z-axis is aligned with $\hat{e}_i$, we evaluate the matrices t_+/t_-, representing the scattering of an electron with spin parallel/anti-parallel to the local moment direction $\hat{e}_i$. These matrices are calculated according to

$$t_{+(-)L}(\varepsilon) = -\frac{1}{\sqrt{\varepsilon}}\sin\delta_{+(-)L}(\varepsilon)e^{i\delta+(-)L(\varepsilon)} \tag{92}$$

where the phase shifts $\delta_L(\varepsilon)$ are computed using effective DFT potentials. These effective potentials, υ_+ and υ_-, differ on account of the 'local exchange splitting', which is the cause of the local moment formation. Unlike the conventional LSDA implementation, the potentials υ_+/υ_- are orbital dependent when the DLM theory is combined with the SIC-LSD approach. This dependency comes about by our SI-correcting certain L channels as discussed earlier. Importantly, the SI-corrected channels of υ_+ and υ_- may differ. Indeed, as described in Section 3.6, the channels to which we apply the SIC are those with a resonant phase shift (Lüders et al., 2005). Such resonant behaviour is characteristic of well-localized electron states, which will establish quasi-atomic like moments. Through the influence they exert on the electron motions, these moments will be reinforced by the spins of more itinerant-like electrons. It thus follows that resonant states will tend to define the local moment orientation and, as such, we expect to SI-correct a greater number of channels of υ_+ than we do for υ_-. For example, for Gd, all 7 υ_+ f-channels are SI-corrected while no correction is applied to any of the υ_- f-channels.

In the paramagnetic regime, we find

$$\tilde{D}_i^0 = \frac{1}{2}(D_+^0 + D_-^0)\tilde{1} + \frac{1}{2}(D_+^0 - D_-^0)\tilde{\sigma}\cdot\hat{e}_i \tag{93}$$

where

$$D_{+(-)}^0 = \left[1 + \left[t_{+(-)}^{-1} - (t^c)^{-1}\right]\tau^{c,00}\right]^{-1}. \tag{94}$$

The superscript 0 signifies that the CPA projector is evaluated in the paramagnetic state. Substituting $P_i(\hat{e}_i) = P^0 = 1/4\pi$ into Eq. (81), we obtain

$$\frac{1}{4\pi}\int d\hat{e}_i\, \tilde{D}_i^0(\hat{e}_i) = \tilde{1}, \tag{95}$$

which becomes, on carrying out the integration,

$$\frac{1}{2}D_+^0 + \frac{1}{2}D_-^0 = 1. \tag{96}$$

Equation (96) is evidently just the CPA equation for a system with 50% of moments pointing 'up' and 50% pointing 'down', that is an Ising-like system. The electronic structure problem is thus reduced to that of an equiatomic binary alloy, where the two 'alloy' components have anti-parallel local moments. Treating this 'alloy' problem with the KKR-CPA, in conjunction with the LSIC charge self-consistency procedure, outlined in Section 3.6 and by Lüders et al. (2005), we arrive at a fully self-consistent LSIC-CPA description of the DLM paramagnetic state.

It should be noted that the equivalence of the DLM electronic structure problem to that of an Ising-like system is purely a consequence of the symmetry of the paramagnetic state, and is not the result of our imposing any restriction on the moment directions. Indeed, in the formalism for the paramagnetic spin susceptibility, which we outline now, we maintain and consider the full 3D orientational freedom of the moments.

Within the DLM method, the magnetization at a site i, $\mathbf{M}_i$, is given by $\int \mathrm{d}\hat{e}_i\ \mu P_i(\hat{e}_i)\hat{e}_i$, where μ is the local moment magnitude, determined self-consistently. In the paramagnetic regime, where P_i is independent of $\hat{e}_i$ and $\mathbf{M}_i = \mathbf{0}$, we can study the onset of magnetic order by considering the response to the application of an external, site-dependent magnetic field. Focusing on the dominant response of the system to line up the moments with the applied field, from the equation of state, we obtain the following expression for the static spin susceptibility:

$$\chi_{ij} = \frac{\beta}{3}\sum_k S^{(2)}_{ik}\chi_{kj} + \frac{\beta}{3}\delta_{ij}, \tag{97}$$

where $S^{(2)}$ is the direct correlation function for the local moments, defined by

$$S^{(2)}_{ik} = -\frac{\partial^2\langle\Omega\rangle}{\partial m_i \partial m_k}, \tag{98}$$

and depends only on the vector difference between the positions of sites i and k. A lattice Fourier transform can hence be taken of Eq. (97), giving

$$\chi(\mathbf{q}) = \frac{1}{3}\beta\mu^2\left(1 - \frac{1}{3}\beta S^{(2)}(\mathbf{q})\right)^{-1}. \tag{99}$$

By investigating the wave vector dependence of the susceptibility, we gain information about the wave vector ($\mathbf{q}$) dependence of the spin fluctuations that characterize the paramagnetic state and the type of magnetic order that might occur as the temperature is lowered through a phase transition. For example in a ferromagnetic material, such as gadolinium, the paramagnetic state is characterized by ferromagnetic spin fluctuations, which have long wavelengths, $\mathbf{q}\sim(0,0,0)$, becoming unstable to them at the Curie temperature, T_C. For a system that orders into an incommensurate anti-ferromagnetic structure, the paramagnetic state is dominated by 'anti-ferromagnetic' spin fluctuations, specified by a finite, incommensurate, wave vector $\mathbf{q} = \mathbf{Q_0}$ which also characterizes the static magnetization or spin density wave state formed below the Néel temperature, T_N. For example, the magnetic structures of the heavy lanthanides terbium (Tb) to thulium (Tm) are described by wave vectors of the form $\mathbf{Q_0} = (0, 0, q_{\mathrm{inc}})$, where individual hexagonal layers are uniformly magnetized in a direction that changes from layer to layer according to the modulation vector q_{inc}.

An expression for $S^{(2)}(\mathbf{q})$, involving scattering quantities obtained from the electronic structure of the paramagnetic state, can be found in Staunton et al. (1986). In brief:

$$S^{(2)}(\mathbf{q}) = \int \mathrm{d}\varepsilon\, f_\beta\left(\varepsilon; v^{(\hat{n})}\right)\frac{1}{\pi}\mathrm{Im}\ \mathrm{Tr}\underline{\Lambda}^0\underline{\chi}_0(\mathbf{q})\underline{\Lambda}(\mathbf{q}), \tag{100}$$

where

$$\underline{\chi}_0(\mathbf{q}) = \int_{BZ}\mathrm{d}^3k\ \underline{\tau}^c(\mathbf{k})\underline{\tau}^c(\mathbf{k}+\mathbf{q}) - \underline{\tau}^{c,00}\underline{\tau}^{c,00}, \tag{101}$$

which is the lattice Fourier transform of the 'non-interacting' susceptibility for the system, and $\underline{\Lambda}(\mathbf{q})$ satisfies the following Dyson-like equation:

$$\underline{\Lambda}(\mathbf{q}) = \underline{\Lambda}^0 + \underline{\Lambda}^0 \underline{\chi}_0(\mathbf{q})\underline{\Lambda}(\mathbf{q}), \tag{102}$$

with $\underline{\Lambda}^0 = \underline{D}^0_+ \left(\underline{t}_+^{-1} - \underline{t}_-^{-1}\right)\underline{D}^0_-$.

7.2.3 Magnetic order in gadolinium: The prototype

A summary of this work is provided by Hughes et al., (2007). Gadolinium's hcp crystal structure is parametrized by two variables, the c/a ratio of the lattice parameters and the atomic unit cell volume, expressed in terms of the WS radius. Experimentally, these two parameters are 1.597 and 3.762 a.u., respectively (Banister et al., 1954). A LSDA calculation of the DOS of gadolinium in its paramagnetic (DLM) state at these lattice parameters reveals the minority 4f-states making a significant contribution at the Fermi energy. This has important implications for the magnetic ordering in the system (Heinemann and Temmerman, 1994). A SIC-LSDA calculation, however, where all seven majority 4f-states are corrected, opens up a Hubbard gap between the occupied and unoccupied f-states. The majority f-states are pushed down to approximately 16 eV below the Fermi energy and the minority f-states are moved away from the conduction bands, reducing the f contribution to the DOS at the Fermi energy. The SIC-LSDA electronic structure thus describes the experimental picture well, with the f-states playing little role in conduction.

Figure 31 shows paramagnetic spin susceptibilities for gadolinium, corresponding to these electronic structures. For the LDA calculation (a), the susceptibility attains its maximum at $\mathbf{q} = (0,0,1)$, indicating that the system should order with a commensurate type 1 anti-ferromagnetic (AF1) structure, where magnetic moments are oppositely aligned in alternate planes along the *c*-axis. This is consistent with ground state energy ($T = 0$ K) calculations from other LDA studies of gadolinium (Heinemann and Temmerman, 1994), where an anti-ferromagnetic structure was found to be energetically favourable over the experimentally observed ferromagnetic structure. The origin of this AF1 coupling derives from the proximity of 4f minority states to the Fermi energy (Kurz et al., 2002). Previous investigations have shown that by pushing the 4f-states away from the Fermi energy, either by treating them as part of the core (Eriksson et al., 1995) or including a Coulomb parameter U for the f-states (LDA + U) (Harmon et al., 1995), a ferromagnetic ground state can be obtained. Since the SIC succeeds in pushing the f-states away from the Fermi energy, the paramagnetic DLM state should show an instability to ferromagnetic order when the LSIC is included. This feature is evident in Figure 31B, which shows the susceptibility attaining its maximum value at $\mathbf{q} = \mathbf{0}$. Note, however, the presence of a shoulder in the susceptibility along the [001] direction, around $q = 0.2$. This feature is significant as we shall show.

Having demonstrated that the LSIC gives an appropriate treatment of the 4f-states, leading to a ferromagnetic ground state, we proceed further with the investigation of gadolinium. We determined the theoretical lattice parameters of

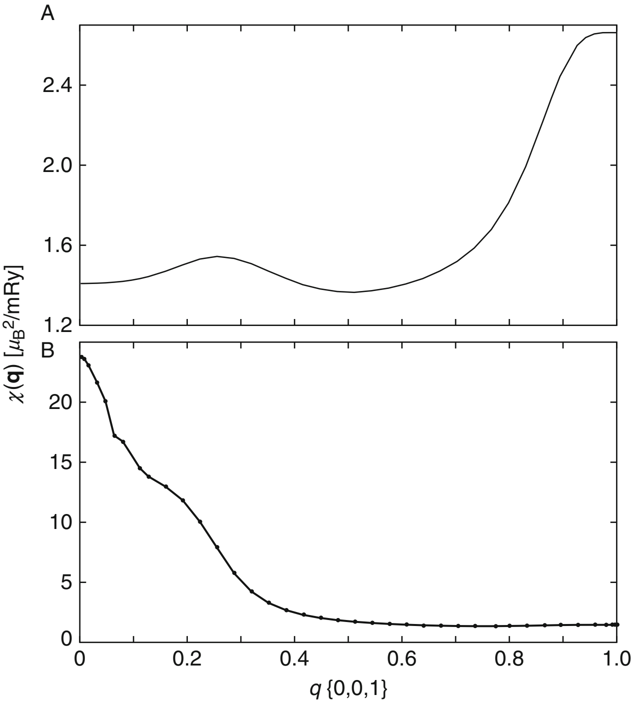

FIGURE 31 Paramagnetic spin susceptibilities for gadolinium at wave vectors along the [0,0,1] direction, obtained from (A) LSDA calculation and (B) LSIC-LSDA calculation.

the paramagnetic state from calculations of the total energy. The energy is minimized at a WS radius which is almost invariant of the c/a values. The overall minimum occurs at a c/a ratio of 1.63 and a WS radius of 3.654 a.u. We find the paramagnetic spin susceptibility for these lattice parameters to attain its maximum at $\mathbf{q} = \mathbf{0}$ also and hence to infer ferromagnetic ordering.

Figure 32 shows the temperature dependence of the $\mathbf{q} = \mathbf{0}$ (ferromagnetic) susceptibility of gadolinium. A Curie-Weiss type behaviour is observed, with T_C = 280 K/324 K for the theoretical/experimental lattice parameters in fair agreement with that measured experimentally, T_C = 293 K (Jensen and Mackintosh, 1991). The effective magnetic moment was 7.34μ_B/7.36μ_B for the theoretical/experimental lattice parameters, also in reasonable agreement with the experimental value of 7.63μ_B and also the results from calculations where the 4f-states were treated as part of the core [7.44μ_B (Turek et al., 2003)] or the LDA + U was used [7.41μ_B (Kurz et al., 2002)]. Examining the l-decomposed spin densities obtained from the LSIC DOS shows the magnetic moment to originate mainly from the f-states (~6.95μ_B), with the remainder coming from a polarization of the d-states (~0.34μ_B) and a small contribution from the s- and p-states (~0.07μ_B).

In our computations, we find the magnetic ordering tendencies of gadolinium to change as the lattice parameters are altered away from their equilibrium values. On changing the c/a ratio over the range 1.54–1.66, with the WS-radius fixed at the

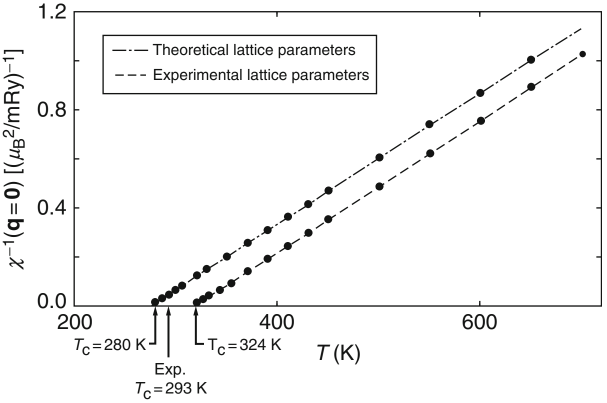

FIGURE 32 Inverse spin susceptibilities for Gd as a function of temperature, calculated for the theoretical and experimental lattice parameters.

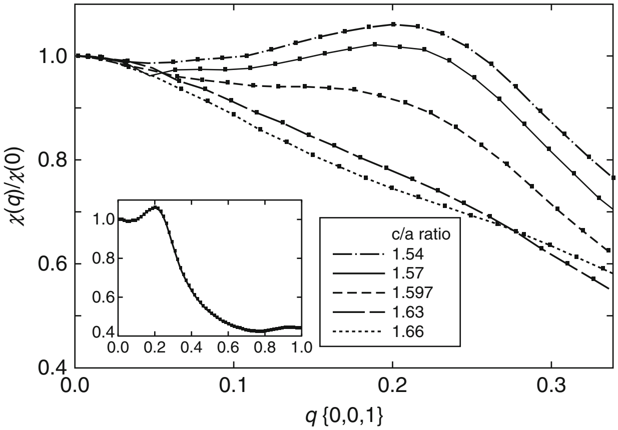

FIGURE 33 Normalized paramagnetic spin susceptibilities for Gd, obtained using the theoretical unit cell volume. The inset shows the susceptibility up to the zone boundary for c/a ratio 1.54.

theoretical value (3.654 a.u.), our calculated paramagnetic spin susceptibility, shown in Figure 33, starts to develop a shoulder near $\mathbf{q} = (0,0,0.2)$, similar to that observed in Figure 31B. Moreover, at the lowest c/a ratios, this shoulder grows into a peak and the susceptibility no longer attains its maximum value at $\mathbf{q} = \mathbf{0}$. The maximum occurs instead at some incommensurate wave vector, q_{inc}, meaning that the system now has a tendency to order into an incommensurate magnetic structure at low temperatures. This could be helical, where the helix turn angle, that is the angle between magnetic moments in adjacent layers, would be given by πq_{inc}.

Such incommensurate ordering is characteristic of the heavy lanthanide elements, terbium to thulium, and is associated with a ‘webbing’ feature of their

Fermi surfaces. This webbing structure contains large parallel sheets of Fermi surface, which can nest together when translated by some vector in **k**-space. This can cause an enhancement of the magnetic susceptibility at the nesting vector, and indeed it has been shown, both theoretically (Keeton and Loucks, 1968) and experimentally (Dugdale et al., 1997), that the size of the nesting vector in the heavy lanthanides is correlated with their magnetic ordering vectors. The shape of the Fermi surface in heavy lanthanide metals depends critically on the c/a ratio of the lattice parameters (Cracknell and Wong, 1973), implying that the magnetic structures of these elements are sensitive to the c/a ratio. This is corroborated by experimental studies by Andrianov and others, which have shown that it is possible to alter the magnetic state of lanthanide metals and alloys by changing the lattice parameters through application of external pressure or tension (Andrianov and Chistiakov, 1997; Andrianov et al., 2000) and by alloying with yttrium (Andrianov, 1995). Such behaviour is possibly interpreted in terms of an electronic topological transition (Lifshitz, 1960; Blanter et al., 1994) at some critical c/a ratio, where the webbing structure of the Fermi surface ruptures.

To analyse our susceptibility results shown in Figures 31B and 33, we investigate the Fermi surface of paramagnetic (DLM) gadolinium at various c/a ratios. For a given configuration of local moments, this Fermi surface can be defined in the usual way. However, when considering the whole ensemble of moment orientations, the 'Fermi surface' is a smeared out average of itself over all moment configurations. A useful tool for defining this surface is the BSF (Faulkner, 1982) that is periodic in reciprocal wave vector **k** space and is given by

$$\overline{A}_B(\mathbf{k},E) = -\frac{1}{\pi}\mathrm{Im}\sum_{nm}\exp[i\mathbf{k}\cdot(\mathbf{R}_n-\mathbf{R}_m)]\int \mathrm{d}^3r\langle G(\mathbf{r}+\mathbf{R}_n,\mathbf{r}+\mathbf{R}_m,E)\rangle, \qquad (103)$$

in terms of an ensemble average, $\langle\rangle$, of the electronic real space Green's function and where the integral over **r** is within the unit cell at the origin. In this case, the ensemble average is taken over local moment configurations (Szotek et al., 1984). For ordered systems, $\bar{A}_B(\mathbf{k}, E)$ consists of a set of δ-function peaks:

$$\overline{A}_B(\mathbf{k},E) = \sum_n \delta(E - E_n(\mathbf{k})), \qquad (104)$$

where $E_n(\mathbf{k})$ is the Bloch energy eigenvalue for the wave vector **k** and band index n. With disorder (here the local moment spin fluctuation disorder), these peaks broaden but their positions can be regarded as an effective band structure, with their width in energy interpreted as an inverse lifetime (Szotek et al., 1984). The Fermi surface of a disordered system is defined as the locus of these peaks at the constant energy $E = E_\mathrm{F}$.

Figure 34 shows the BSF of paramagnetic Gd at the Fermi energy, E_F, calculated for the sets of lattice parameters used in Figure 33. For c/a ratios of 1.597 or smaller, a webbing feature is displayed and the corresponding nesting vector is indicated by an arrow in panel (a). At a c/a ratio of 1.63 (Figure 33D), the webbing feature has started to rupture, and at a c/a ratio of 1.66 (Figure 33E), the rupturing is complete and the Fermi surface no longer has any significant regions of nesting.

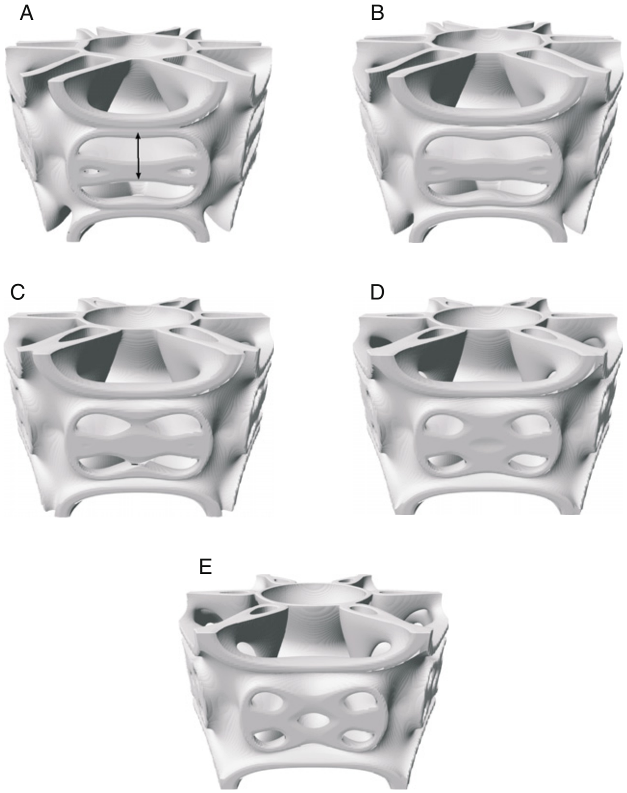

FIGURE 34 Bloch spectral function of Gd in the hexagonal BZ, calculated at the Fermi energy. Panels (A), (B), (C), (D), and (E) are for c/a ratios 1.54, 1.57, 1.597, 1.63, and 1.66, respectively, with theoretical unit cell volumes used but not for high c/a ratios.

This concurs with the results shown in Figure 33, where the susceptibility is enhanced at some incommensurate **q** vector for low c/a ratios, Figure 35A shows a cross section through the webbing structure for c/a ratio 1.54. The nesting structure is created by two bands which just cross the Fermi energy along the L–M direction. The broadening of the spectral function peaks, caused by the local moment disorder, means that the bands are smeared, which results in their merging together at the L point. The magnitude of the nesting vector, $\mathbf{Q}_0$, is $\sim$0.2 (in units of $2\pi/c$) and coincides with the size of the magnetic ordering wave vector, q_{inc}, observed in Figure 33A. Figure 35B and C show the same cross section of the BZ, with the BSF evaluated using c/a ratios 1.57 and 1.66, respectively. In panel (b), the Fermi surface has a distinctive ‘dog-bone’ shape, with two extremal vectors, one centred and the other non-centred, connecting the sheets of Fermi surface. Figure 35A and B show the length of the centred nesting vector to decrease as the c/a ratio increases. This is in keeping with the experimental results of Andrianov, where the length of the magnetic ordering vector decreases continuously as the c/a ratio is increased. This does not, however, interpret the

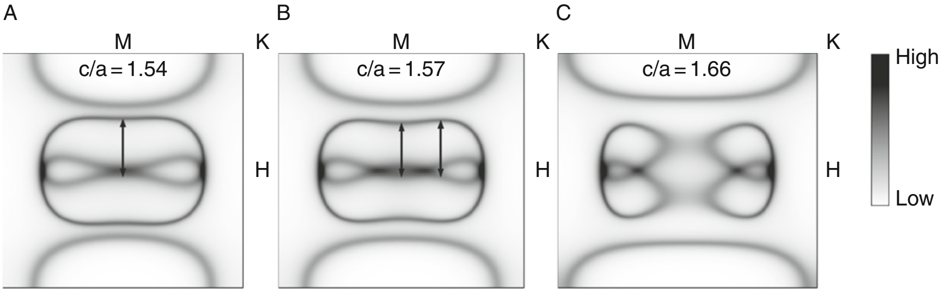

FIGURE 35 Bloch spectral function of Gd on the HLMK plane of the hexagonal BZ. Panels (A), (B), and (C) are for c/a ratios 1.54, 1.57, and 1.66, respectively, with theoretical unit cell volumes used. The centre of the plane is the L point. Nesting vectors are indicated by arrows. The colour plot can be found in Hughes et al. (2007).

susceptibility results shown in Figure 33 correctly, where the position of the incommensurate ordering peak is almost invariant to the c/a ratio used. If, instead, we look at the length of the non-centred vector, we see that it stays fairly constant as the c/a ratio is altered. It thus appears that it is the non-centred nesting vector which is responsible for the incommensurate ordering observed in our calculations. This is in agreement with recent theoretical work by Nordström and Mavromaras (2000) who found that the non-centred vector was the appropriate nesting vector.

Turning now to the magnetic ordering behaviour as a function of unit cell volume, from our susceptibility calculations, we find two distinct cases differentiated according to the c/a ratio of the lattice parameters. For high c/a ratios, corresponding to systems with no webbing feature, ferromagnetic ordering is predicted for all volumes. For low c/a ratios, corresponding to systems with webbing, a more complicated picture emerges as shown in Figure 36. The webbing produces an enhancement of the susceptibility at the nesting vector for all volumes. However, as the volume increases, the height of the incommensurate peak relative to the $\mathbf{q} = \mathbf{0}$ (ferromagnetic) peak decreases, and at a WS radius of 3.710 a.u., there is a near degeneracy between the two ordering types. For the highest WS-radii, the susceptibility obtains its maximum value at $\mathbf{q} = \mathbf{0}$ and so we predict the system to be ferromagnetic. Thus, in order for the nesting enhancement to be strong enough so that incommensurate ordering wins out over ferromagnetic ordering, the unit cell volume needs to be below a certain critical value.

The behaviour of the paramagnetic spin susceptibility, χ, is determined by the direct correlation function, $S^{(2)}$ [Eq. (100)]. This function can be fit in terms of real-space parameters:

$$S^{(2)}(\mathbf{q}) = \sum_n \sum_{i \in n} S_n^{(2)} \exp(i\mathbf{q} \cdot \mathbf{R}_i), \tag{105}$$

where $S_n^{(2)}$ is the direct pair interaction between an atom at the origin and another in the nth neighbour shell, with position vector $\mathbf{R}_i$. For the magnetic structures

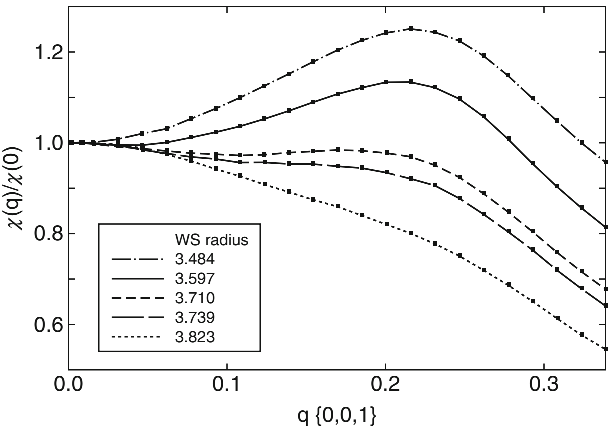

FIGURE 36 Normalized paramagnetic spin susceptibilities for Gd for various WS radii, obtained using a c/a ratio of 1.54.

considered in this section, $\mathbf{q} = (0, 0, q)$ and hence $\exp(i\mathbf{q}\cdot\mathbf{R}_i) = \exp(iqR_z)$, where R_z is the z-component of $\mathbf{R}_i$. Since the heavy lanthanides adopt hcp structures, with two atoms per unit cell, they can be considered in terms of two interpenetrating sublattices. Consequently, two distinct sets of pair correlations can be considered, one where both sites are on the same sublattice ('intra sublattice') and one where the sites are on different sublattices ('inter-sublattice'). For intra- (inter-) sublattice pairs, $R_z = l * c$ ($R_z = (l{-}1/2) * c$) where $l \in \mathbb{Z}$ and c is the 'c' lattice parameter. The 'layer' indices, l, can be used to reparametrize the real space fit of Eq. (105):

$$\begin{aligned} S^{(2)-\text{intra}}(\mathbf{q}) &= S_0^{(2)-\text{intra}} + \sum_{l\in \mathrm{N}}^{l_{\text{top}}} S_l^{(2)-\text{intra}} \cos(qlc) \\ S^{(2)-\text{inter}}(\mathbf{q}) &= \sum_{l\in \mathrm{N}}^{l_{\text{top}}} S_l^{(2)-\text{inter}} \cos[q(l-(1/2))c], \end{aligned} \tag{106}$$

where $S_l^{(2)}$ is the sum of all pairwise interactions between sites in the lth layer and the site at the origin. The $S_0^{(2)}$component corresponds to the sum of pair interactions between the atom at the origin and atoms in the layer containing the origin. For the fitting of the direct correlation function to be computationally tractable, the sum over layers, l, in Eq. (106) is truncated at some finite value, l_{top}. We find that $l_{\text{top}} = 8$ gives a good fit of $S^{(2)-intra}$ and $S^{(2)-\text{inter}}$. Figure 37 shows layer-resolved component of $S^{(2)}$ where integer (half-integer) values of R_z/c correspond to intra- (inter-) sublattice components. The biggest contribution to $S_l^{(2)}$ comes from the layers at $R_z = \pm c/2$. This is to be expected since, in hcp structures that have a c/a ratio less than the ideal value $\sqrt{8/3} \approx 1.63$, the nearest neighbours to any given atom are contained within the layers adjacent to the atom, not the layer in which the atom actually lays. The components of $S^{(2)}$ are seen to oscillate as a function of R_z, in the manner of an RKKY-type interaction.

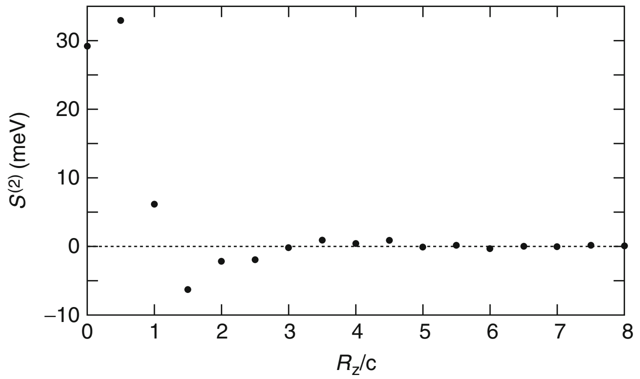

FIGURE 37 Layer-resolved components of the effective exchange interaction, $S^{(2)}$.

7.2.4 Magnetic phase diagram for the heavy lanthanide metals

The two types of magnetic ordering that we encountered during our investigation of gadolinium (ferromagnetic ordering and incommensurate ordering, modulated along the *c*-axis) correspond to the two types of ordering that are observed experimentally across the heavy lanthanide series. To investigate the competition between these two ordering types, we define a 'magnetic ordering parameter', α, which gives a measure of the relative strengths of the 'incommensurate spin fluctuations' and ferromagnetic spin fluctuations that characterize the paramagnetic state. To do this, we examine the wave vector-dependent critical temperature, $T_c(\mathbf{q})$, obtained from our susceptibility and direct correlation function calculations, that is from $\det\left[\mathbf{I}_n - 1/3\beta\mathbf{S}^{(2)}(\mathbf{q})\right] = 0$ with the 2×2 $\mathbf{S}^{(2)}$ matrix specified by

$$\begin{pmatrix} S^{(2)-\mathrm{intra}}(\mathbf{q}) & S^{(2)-\mathrm{inter}}(\mathbf{q}) \\ S^{(2)-\mathrm{inter}}(\mathbf{q}) & S^{(2)-\mathrm{intra}}(\mathbf{q}) \end{pmatrix},$$

where $S^{(2)-\mathrm{intra}}(\mathbf{q})$ and $S^{(2)-\mathrm{inter}}(\mathbf{q})$ correspond to the fit functions in Eq. (106). By using these fit functions, we mitigate the effects of computational noise, which may be important when analysing the delicate competition between the two ordering types.

If the critical temperature function $T_c(\mathbf{q})$ has only one peak, at $\mathbf{q} = \mathbf{0}$, we set $\alpha = 0$. If $T_c(\mathbf{q})$ has only one peak, but at some incommensurate q-vector, q_{inc}, we set $\alpha = 1$. Clearly, $\alpha = 0$ corresponds to the paramagnetic state being dominated by ferromagnetic spin fluctuations and $\alpha = 1$ corresponds to its domination by spin fluctuations with some finite, incommensurate wave vector. When $T_c(\mathbf{q})$ has a two peak structure, corresponding to a competition between the two ordering types, we examine the values of $T_c(\mathbf{q})$ at its turning points. We define $T_0 = T_c(\mathbf{q} = \mathbf{0})$, $T_{\mathrm{inc}} = T_c(\mathbf{q} = (0, 0, q_{\mathrm{inc}}))$ and $T_{\min} = T_c(\mathbf{q} = \mathbf{q}_{\min})$, where $\mathbf{q}_{\min}$ is the position of the minimum that occurs between the $\mathbf{q} = \mathbf{0}$ and $\mathbf{q} = (0, 0, q_{\mathrm{inc}})$ maxima. If $T_0 > T_{\mathrm{inc}}$ we set

$$\alpha = \frac{T_{\mathrm{inc}} - T_{\min}}{2(T_0 - T_{\min})} \tag{107}$$

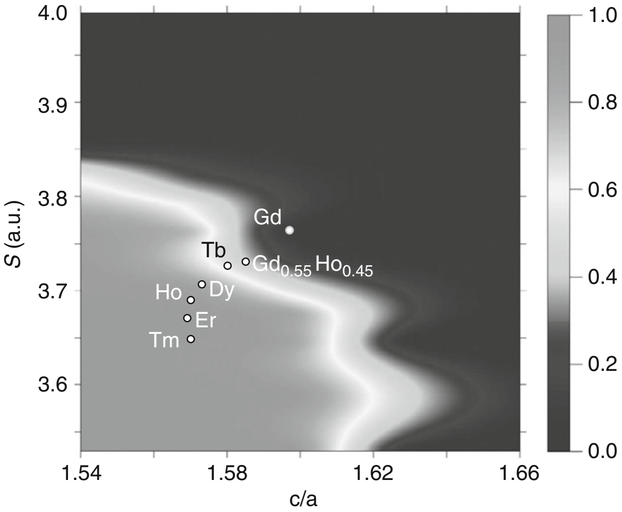

FIGURE 38 Ordering parameter, α, for gadolinium as a function of c/a ratio and WS radius. The black region corresponds to ferromagnetic and the grey region to incommensurate anti-ferromagnetic spin fluctuations. The experimental lattice parameters of all the heavy lanthanide elements are indicated by circles; a grey (black) circle indicates that experimentally the high-temperature ordered state of the element is ferromagnetic (incommensurate anti-ferromagnetic). The circle for $Gd_{0.55}Ho_{0.45}$ indicates the experimental lattice parameters of a Gd–Ho alloy at the critical concentration of Ho at which an incommensurate anti-ferromagnetic phase first appears. The colour plot can be found in Hughes et al. (2007).

and if $T_0 < T_{\text{inc}}$, we set

$$\alpha = 1 - \frac{T_0 - T_{\min}}{2(T_{\text{inc}} - T_{\min})}. \tag{108}$$

Clearly, α is defined such that $\alpha > 0.5$ indicates a stronger tendency towards incommensurate ordering and $\alpha < 0.5$ indicates a stronger tendency towards ferromagnetic ordering.

In Figure 38, we show α for gadolinium as a function of c/a ratio and unit cell volume. To account for the difference between the theoretical and experimental volumes, the WS-radii in the figure are scaled, such that data shown at the experimental WS radius of gadolinium corresponds to data calculated at the theoretical WS-radius. On this phase diagram, we also indicate where the experimental lattice parameters of all the heavy lanthanide elements lie, as well as those of a Gd–Ho alloy. Since the heavy lanthanide elements differ only in how many 4f electrons they have, and it is the sd conduction electrons that are responsible for mediating the interaction between magnetic moments, gadolinium can be considered a magnetic 'prototype' for the post-Gd heavy lanthanide elements. Thus, we propose that the behaviour of gadolinium as a function of lattice parameters is a model of all the other heavy lanthanide elements. By considering the phase diagram, Figure 38, as being universal to all heavy lanthanide systems, we predict that when going left to right in the heavy lanthanide series, there will be a trend away from ferromagnetism and towards incommensurate ordering. This is exactly what is observed experimentally, with the magnetic modulation vector starting out at zero for gadolinium (ferromagnetic ordering) and then progressively increasing through the series to give rise to various incommensurate antiferromagnetic structures. From the phase diagram, we predict that the transition between ferromagnetism and incommensurate ordering occurs very rapidly as a function of c/a ratio, particularly for the higher unit cell volumes. This is consistent with recent experimental work on terbium under uniaxial tension. Terbium exhibits helical ordering and has a WS-radius of 3.724 a.u., with a c/a ratio of 1.580. It has been shown (Andrianov et al., 2000) that by increasing the c/a ratio by as little as 0.002 the helical ordering could be completely suppressed. In the phase diagram, the elements dysprosium and terbium are positioned close to, or within, the transition region between ferromagnetic and incommensurate ordering. This is consistent with the experimental behaviour of these two systems, which exhibit incommensurate ordering at high temperatures and ferromagnetic ordering at low temperatures.

Because of their structural similarities, Gd alloys easily with all the other heavy lanthanide elements, R′. These alloys transform from ferromagnets to incommensurate magnetically structured materials once the concentration of R′ exceeds a certain critical concentration x_c. We can use the phase diagram to predict these critical alloy concentrations. These are listed in Table 11 and are in good agreement with experimental values where known.

We can also compute estimates of the magnetic ordering vectors of all the heavy lanthanides from our susceptibility calculations for gadolinium at the appropriate lattice parameters. The results are shown in Figure 39. For example, when we performed a calculation for Gd at the experimental lattice parameters of terbium (Tb), specified by a c/a ratio of 1.580 and a WS-radius of 3.724 a.u., the susceptibility peaked at a wave vector $\mathbf{q} = (0, 0, 0.13)$, which is in good agreement with the experimental ordering vector of Tb, (0, 0, 0.11). Overall, we predict a gradual increase in the ordering vector across the heavy lanthanide series, in agreement with experiment. We also find that the magnetic ordering vectors of

TABLE 11 Critical alloy concentrations of $Gd_{1-x}R_x$ systems

	Critical concentration, x_c	
System	Theoretical	Experimental
$Gd_{1-x}Tb_x$	0.78	
$Gd_{1-x}Dy_x$	0.56	0.50[a]
$Gd_{1-x}Ho_x$	0.49	0.45[b]
$Gd_{1-x}Er_x$	0.45	
$Gd_{1-x}Tm_x$	0.42	

[a] Milstein and Robinson (1967).

[b] Taken from Andrianov and Chistiakov (1997).

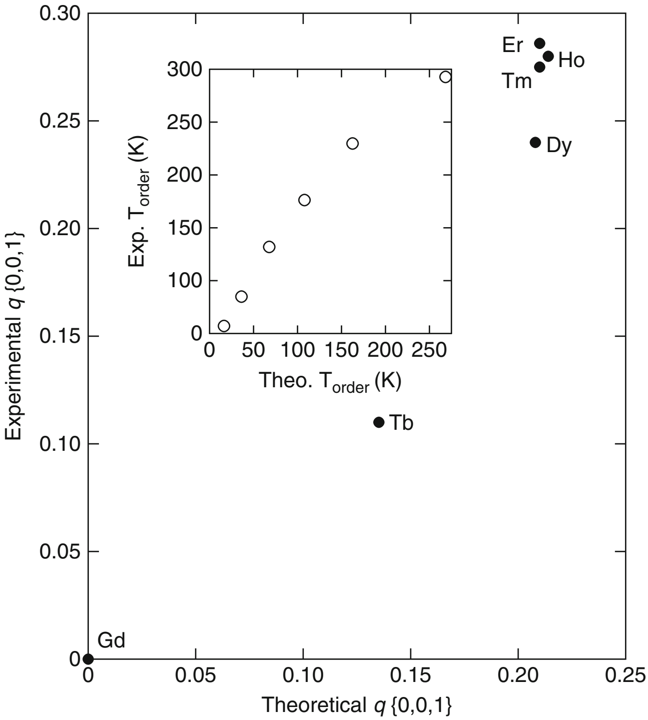

FIGURE 39 Experimental magnetic ordering vectors of the heavy lanthanides versus those predicted from *ab initio* calculations for gadolinium. The inset shows the corresponding ordering temperatures. Experimentally Gd has the highest ordering temperature, which decreases monotonically through the heavy lanthanide series.

the last three members of the series (Ho, Er and Tm) all lie close together, again in agreement with experiment.

Making Gd the prototype for magnetic order in the heavy lanthanides is justified since the Gd ion has orbital angular momentum $L = 0$ and so spin-orbit coupling effects do not need to be incorporated into our calculations. However, if we want to infer magnetic transition temperatures for the other heavy lanthanides from our Gd calculations, LS coupling has to be considered. This can be accomplished by scaling our magnetic transition temperature estimates with the de Gennes factor $(g_J\text{–}1)^2\ J(J + 1)$ (Blundell, 2001). As shown in the inset of Figure 39, the transition temperatures obtained from this approach reproduce the experimental trend, although the magnitudes of the temperatures are systematically underestimated. It is worth noting that when we computed the estimates of the magnetic ordering vectors, spin-orbit coupling was not important. This is because, as argued earlier, the type of magnetic order exhibited by the heavy lanthanides is determined by the sd conduction electrons, which are little affected by spin-orbit coupling and which all the heavy lanthanides have in common.

Overall, the physical picture that emerges from the magnetic ordering phase diagram, Figure 38, links unequivocally the lattice parameters of the heavy lanthanides with their magnetic properties. Our results have verified the critical role that the c/a ratio plays in determining the magnetic ordering types of the heavy lanthanides and how this is linked to the Fermi surface of the paramagnetic phase. However, our discovery that the atomic unit cell volume, associated with the lattice parameters, is just as important in determining the magnetic properties has enabled us to develop a much more complete understanding of heavy lanthanide magnetism. In particular, we have shown that even when the c/a ratio of a heavy lanthanide system is below the critical value needed for a webbing structure, incommensurate anti-ferromagnetic ordering is not necessarily favoured over ferromagnetic ordering; for incommensurate ordering to win out over ferromagnetic ordering, the unit cell volume needs to be below a certain value. Experimentally, the unit cell volumes of the heavy lanthanides decrease with increasing atomic number, in accord with the well-known 'lanthanide contraction' (Taylor and Darby, 1972). This contraction occurs because as the number of electrons in the poorly shielding 4f orbitals is increased, there is an increase in the effective nuclear charge and, correspondingly, a decrease in ionic radii. Our findings evidently suggest that this contraction helps promote the incommensurate ordering in the post-Gd heavy lanthanides. The roles that the different types of valence electrons play in determining the magnetic structures of the heavy lanthanides are thus clear; the itinerant sd electrons, common to all the heavy lanthanides, mediate the interaction between magnetic moments and it is the nesting of their Fermi surfaces that can lead to instabilities in the paramagnetic phase with respect to the formation of incommensurate spin density waves. The f electrons, on the other hand, are responsible for setting up the magnetic moments and, as their number increases across the heavy lanthanide series, they play an indirect role in promoting the incommensurate ordering by means of the lanthanide contraction.

7.3 Valence fluctuations

As mentioned in Section 7.1, the alloy analogy is a versatile approach that can be applied to different types of thermal fluctuations. In particular, we will now also include valence fluctuations. The theoretical framework remains largely as outlined in the previous section, but the possible configurations at a given site now include the valence state in addition to the direction of the local moment. In the following, this approach will be applied to the finite temperature phase diagram of Ce, focusing on the isostructural α–γ transition (Lüders et al., 2005). At absolute zero, the two phases can be identified as the tetravalent α-phase at low volumes, and the trivalent γ-phase at high volumes. Thus, these phases correspond to a delocalized or localized f-state, respectively. Figure 40 shows the ground state energies for different valence configurations, namely the tetravalent f^0 configuration, corresponding to an LDA calculation, and SIC-LSD calculations for trivalent f^1 configurations, where f-states with different symmetries are treated as localized, as seen in Table 12. These zero temperature calculations assume a ferromagnetic alignment of the local moments in the γ-phase. However, when discussing the finite temperature phase diagram of Ce, we will account for the

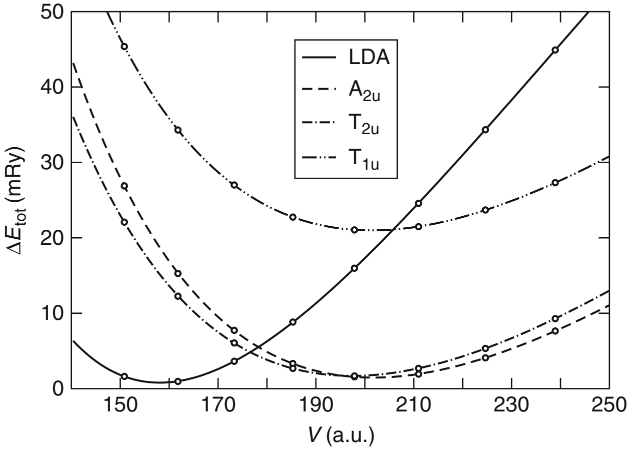

FIGURE 40 The calculated total energies for Ce from LDA and SIC-LSD, with different f-states localized, as functions of volume, given in atomic units $[(a_0)^3]$.

TABLE 12 The total energy differences as obtained from the LDA and SIC-LSD calculations, with respect to the ground state energy solution (LDA), for Ce in different f-configurations. The corresponding volumes and bulk moduli (evaluated at the theoretical lattice constants) are also given

		ΔE (mRy)	V $(a_0{}^3)$	B (kbar)
LDA		0.0	158	701
	A_{2u}	0.8	202	355
SIC	T_{1u}	20.3	201	352
	T_{2u}	1.5	197	351

paramagnetic state with its disorder of the local moments using the DLM framework of Section 7.2. The splittings of the states, shown in Table 12, are due to the crystal field since in this calculation, the spin-orbit coupling has been neglected. We will later account for spin-orbit coupling through the magnetic entropy terms. Table 12 shows that the state with the A_{2u} symmetry provides the lowest energy solution for the γ-phase. Only 0.8 mRy separate the minima of the α- and γ-phases, giving rise to the transition pressure at the absolute zero of about −2.3 kbar. This is in good agreement with the experimental value of −7 kbar, when extrapolated to zero temperature, and with other theoretical values. The bulk moduli, given in Table 12, are calculated at the theoretical equilibrium volumes. When evaluated at the experimental volumes, their values are substantially reduced to 239 kbar for the α-phase and 203 kbar for the γ-phase, which is in considerably better agreement with the experimental data. The volume collapse is obtained at 22%, which also compares well with the experimental values of 14–17%. We note that the underestimate of the volumes of both the α- and γ-phases is mainly due to the KKR l-convergence problem. Although it seems that this l-convergence problem should affect the LSD and SIC-LSD calculations in a similar manner, we observe a significantly larger error for the α-phase. This larger error for the α-phase, which is also found in the LMTO-ASA calculations, is most likely because LDA is not adequate for describing the correlated nature of the α-phase, as observed in experiments. In fact, the LDA calculations correspond to the high-pressure α'-phase, which is purely tetravalent and has a smaller lattice constant than the observed α-phase.

We now return to the description of Ce at finite temperatures. The alloy analogy for describing the thermal valence and spin fluctuations gives rise to a ternary alloy, consisting of Ce atoms with localized f-electrons, described by SIC-LSD, with a concentration of $c/2$ for each spin direction (spin up and spin down), and Ce atoms with delocalized f-electrons, described by the LDA, with the concentration (1–c). The free energy of the system is obtained by adding the relevant entropy contributions to the total energy [see Eq. (28)]. The electronic particle-hole entropy, $S_{\mathrm{el}} = -k_{\mathrm{B}} \int \mathrm{d}\varepsilon\, n(\varepsilon)[f_\beta(\varepsilon) \ln f_\beta(\varepsilon) + (1-f_\beta(\varepsilon)) \ln (1-f_\beta(\varepsilon))]$, is obtained from the underlying band structure calculations (Nicholson et al., 1994). Here $n(\varepsilon)$ is the DOS and $f_\beta(\varepsilon)$ denotes the Fermi distribution. The magnetic entropy $S_{\mathrm{mag}}(c) = k_B c \ln 6$, which corresponds to a spin-orbit coupled state with $J = 5/2$, accounting for the magnetic disorder, while the mixing entropy, $S_{\mathrm{mix}}(c) = -k_{\mathrm{B}}(c \ln c + (1-c) \ln (1-c))$, stems from the disorder among the localized and delocalized Ce atoms. The vibrational entropy, S_{vib}, is assumed to be the same in both phases and therefore is neglected here. In order to determine the full p–T phase diagram, it is necessary to calculate the Gibbs free energy:

$$G(T, c, p) = F(T, c, V(T, c, p)) + p(T, c, p). \tag{109}$$

From this, at each given pressure and temperature, we can determine the concentration of the trivalent Ce, by minimizing the Gibbs free energy with respect to c.

Our calculations go beyond all the earlier work because SIC-LSDA treats all the f-states on equal footing and the KKR-CPA allows for a consistent description of spin and valence disorder. Johansson et al. (1995) used a binary pseudo-alloy concept, but needed one adjustable parameter to put on a common energy scale both the γ-phase, described by LSDA with one f-state included into the core, and the α-phase, described by the standard LSD approximation, with all the f-states treated as valence bands. Svane (1996) performed SIC-LSD calculations using a supercell geometry which limited him to the study of a few concentrations only.

We can obtain the free energy of the physical system at a given volume by evaluating the concentration-dependent free energy at the minimizing concentration c_{min}:

$$F(T, V) = F(T, c_{\mathrm{min}}, V). \tag{110}$$

This free energy, as a function of volume and temperature, is displayed in Figure 41, clearly showing a double-well behaviour for low temperatures, which gets gradually smoothed out into a single minimum as the temperature is increased. In addition, it is found that at elevated temperatures the free energy is lowered mainly at large lattice volumes, which is due to the greater entropy of the γ-phase.

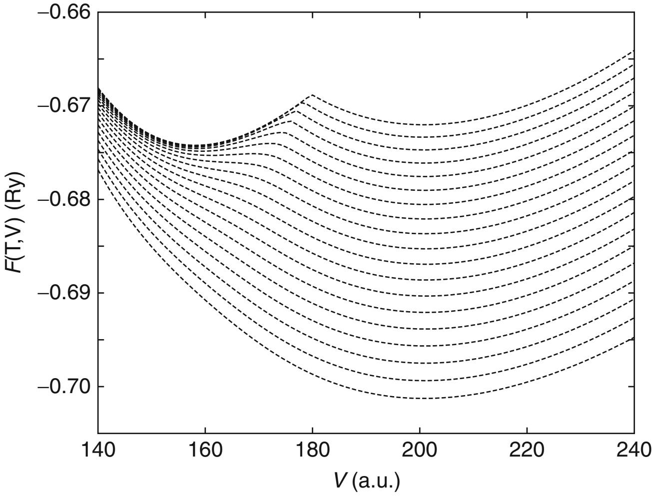

FIGURE 41 The free energies as function of the volume for the temperatures 0 (highest curve) and 1800 K (lowest curve) in steps of 100 K.

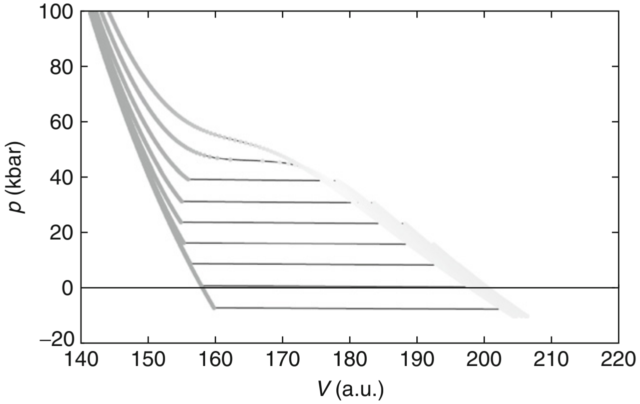

FIGURE 42 Calculated equation of state of Ce for the temperatures $T = 0$ (lowest curve), 200, 400, 600, 800, 1000, 1200, 1400, and 1600 K (highest curve). The shading indicates the fraction of localized electrons: light is all localized (γ-phase) and dark is all delocalized (α-phase).

Inserting the minimizing concentration $c_{\min}$ into the pressure–volume relation

$$p(T, V) = p(T, c_{\min}, V) = -\frac{\partial}{\partial V} F(T, c_{\min}, V) \tag{111}$$

allows one to calculate the isothermal pV-relations of Ce, which are displayed in Figure 42, where it can be seen that the average valence, close to the coexistence line, gradually changes with increasing temperature. Above the critical temperature, the valence changes continuously with increasing pressure from trivalent to tetravalent.

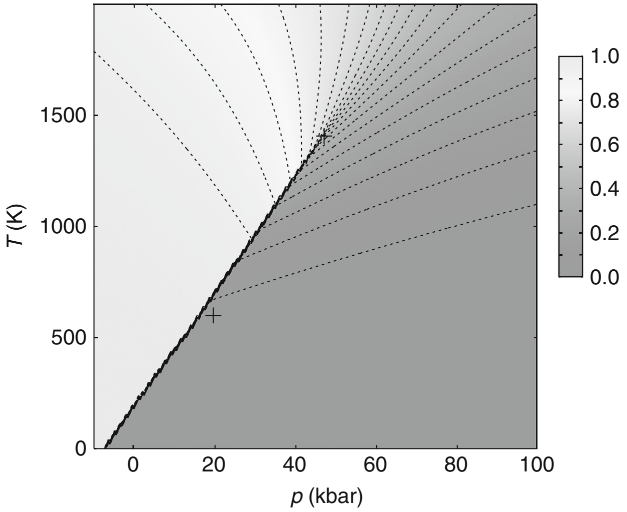

FIGURE 43 Phase diagram obtained for the pseudo-alloy, composed of α-Ce (light grey area) and γ-Ce (dark grey area). The grey shades display the fraction of localized electrons. The crosses indicate the calculated (upper cross) and experimental (lower cross) critical points.

In Figure 43, we present the phase diagram, obtained from the free energies of the α–γ pseudo-alloy, with the γ-phase described by the DLM state. Here, it can be easily followed how the transition becomes continuous above the critical point. The calculated critical temperature overestimates the experimental value by about a factor of 2. It is still reasonable considering that the critical temperature is very sensitive to various small details of the calculations and in particular the theoretical lattice parameters of both the α- and γ-Ce phases. Also, the calculated slope of the phase separation line is slightly too steep, compared to the experimental phase diagram. The likely reason being the overestimate of the volume collapse that enters the definition of the slope, given by the ratio $(V_\gamma - V_\alpha)/(S_\gamma - S_\alpha)$, where $S_{\alpha(\gamma)}$ and $V_{\alpha(\gamma)}$ are, respectively, values of the entropy and volume of the $\alpha(\gamma)$-phase at $T = 0$ K.

Examining in more detail the discontinuity across the phase separation line displayed in Figure 44, we find the magnitude of the discontinuities for the various contributions to the Gibbs free energy. As expected, all contributions vanish at the critical temperature, above which there is a continuous cross-over between the α- and the γ-phase. It can be seen that it is the entropy discontinuity which is by far the largest contribution. The phase transition is therefore driven by entropy, rather than by energetics. The entropy discontinuity itself is mainly determined by the magnetic entropy.

Summarising this section, we have demonstrated that the alloy analogy of fluctuations can be very useful, giving rise to a simple picture of the underlying physics, relating the magnetic phase diagram of the late lanthanides to the lanthanide contraction, and identifying the entropy as the driving force behind the α–γ phase transition in Ce. In Section 8, we will outline how this approach can be

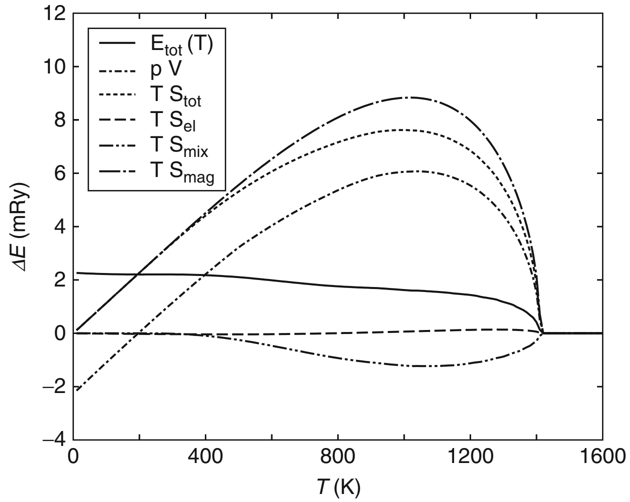

FIGURE 44 Discontinuities of the total energy, the total entropy TS, and the pV term over the phase separation line as function of the temperature. The entropy term is further decomposed into the electronic, the mixing, and the magnetic contribution.

generalized to describe also dynamical, namely quantum, fluctuations, which up to now have been ignored.

8. DYNAMICAL FLUCTUATIONS: THE 'ALLOY ANALOGY' AND THE LANDAU THEORY OF PHASE TRANSITIONS

Having made use of the 'alloy analogy' approach to describe fluctuations in density functional theories, a number of comments concerning its status in the general theory of condensed-matter are in order. First, it should be stressed that while in the context of phase transitions, such methodology yields an accurate description of the high temperature, homogeneous disordered state, and a reliable account of its instability at some critical transition temperature T_c, it is seriously incomplete for $T < T_c$ as the ground state is approached. Second, one should not fail to mention that there is now a fairly well-developed conceptual framework, a dynamical version of the 'alloy analogy', in terms of which the shortcomings of the above static version near $T \rightarrow 0$ can be understood, and even remedied.

As is well known, there are two ways of approaching the problem of phase transitions. One of these starts with a study of the ground state and seeks to determine the critical temperature T_c, at which thermal fluctuations destroy the equilibrium state smoothly connected to it. Usually, at this point either some symmetry breaking order of the ground state is lost, as in a continuous phase transitions, or the system becomes an inhomogeneous mixture of coexisting phases as in the cases of the Ce α–γ, liquid-gas or other first-order transitions. The alternative to this approach is to start with the high temperature, $T > T_c$, high symmetry, disordered phase, and investigate its stability as the temperature is lowered. This is the strategy adopted in a phenomenological Landau Theory (Landau and Lifschitz, 1980). From the point of view of first-principles calculations, the former seems easier as it involves ground state calculations. However, the 'alloy analogy' calculations highlighted in this review correspond to the latter. Evidently, in these the role of the CPA is to describe thermal fluctuations of various local electronic configurations and hence the KKR-CPA procedure is an appropriate tool for the study of the high-temperature, high-symmetry equilibrium states. In fact, when suitably generalized, it can be used for calculating the coefficients in the Landau expansion of the free energy (Gyorffy et al., 1989) and thereby turning the phenomenological theory into a material specific, quantitative first-principles theory.

Examining the accuracy and reliability of the calculations reviewed in Sections 7.2 and 7.3 in the light of the above remarks prompts the following observation: the electronic structure relevant to these calculations is a smeared out version of that at $T = 0$. Namely, any coherent fluctuation lasting longer than $\hbar/k_B T$ can be assumed to have been averaged to zero and hence such calculations are more forgiving than those near $T = 0$ where timescales much longer than $\hbar/k_B T_c$ need to be accounted for. Thus, the first-principles Landau Theory alluded to above can be considered a robust and efficient theory of the phase diagrams. By contrast for $T < T_c$, as T tends to 0, longer and longer timescales make their presence felt and a more accurate description of the many-electron problem becomes necessary.

A particular general shortcoming of the 'alloy analogy' approximation is that it cannot describe quantum fluctuations such as the zero point fluctuations of spin waves. Evidently, these can be important at and near $T = 0$. Moreover, an ensemble average of static fluctuations depicted by the 'alloy' configurations will, within the CPA, inevitably lead to quasi-particles with finite lifetime even at $T = 0$. Namely, the ground state is generically not that of a Fermi liquid as it mostly should be. In what follows we shall summarize briefly the current state of conceptual framework that needs to be invoked to deal with these issues.

In condensed matter at a site, an electron scatters from both the atomic nuclei and the other electrons in its vicinity. Such 'target' is not, in general, a static, spin-dependent electrostatic, c-number potential but a time-dependent quantum mechanical object which recoils during the scattering process. Clearly, the full complexity of scattering events produced by such 'targets' are not described by the static mean field theory language of the 'alloy analogy'. However, it turns out that their essence is adequately captured by a dynamical generalization of this well tried methodology, namely the DMFT (Georges et al., 1996). Like the 'alloy analogy', this elegant procedure focuses on the single site nature of the many-electron problem in solids and it can be viewed as a time-dependent CPA in which the potential seen by an electron at a site changes with time during the scattering process and the averaging over configurations becomes average over all histories of such variations (Kakehashi, 2002).

A remarkable consequence of introducing time-dependent one-electron potentials into the calculation is that the well-known instability of a degenerate Fermi system to sudden local perturbations (Anderson, 1967) comes into play. This effect, which is well understood in the context of the X-ray edge-singularity (Nozieres and DeDominicis, 1969) and the Kondo (Anderson et al., 1970) problems, leads to qualitatively new features in the one-electron spectra predicted by the DMFT compared with the consequences of the static CPA-based theories. The most spectacular of these is the central peak, arising from the Kondo resonance at the Fermi energy, between the upper and lower Hubbard bands, which are already evident in the static alloy analogy calculations. As physical consequences of this peak, one might mention its role in the explanation of the metal-insulator Mott transition (Georges et al., 1996) and the spin-polarization Kondo cloud that screens magnetic impurities in dilute alloys (Anderson et al., 1970). Indeed, it may very well be relevant to the Ce α–γ transition discussed in Section 7.3 (Held et al., 2001).

Since their invention in the early 1990s, the DMFT technique (Georges et al., 1996) and its cluster generalization DCA (Hettler et al., 1998) have been studied intensively and have been successfully applied to many different problems in metal physics. But, while its virtues and limitations are well documented for simple tight binding model Hamiltonians, its implementation within the context of a fully first-principles theory remains an aspiration only. What has been done, repeatedly and with considerable success, is what may be called the LDA $+ U +$ DMFT method (Georges et al., 1996). In these calculations, the LDA $+ U$ part is a method for generating an effective, usually a multi-band Hubbard, Hamiltonian which serves as input into a DMFT procedure, but there is rarely an effort to recalculate the LDA bands (site energies and hopping integrals) or the electron–electron interaction parameter U with the view of iterating to self-consistency. Strangely, although technically the problem appears to be difficult conceptually, thanks to the numerous analytical and numerical results mentioned above, it is relatively simple. The fluctuations to be captured by the putative theoretical framework are tunnelling between atomic-like local electronic configurations, and of these, there are only few that are degenerate in energy and hence can be the source of a Kondo-like resonance. In other words, at an atomic centre, an electron scatters from a quantum mechanical two or few level systems instead of a classical effective electrostatic potential. Scaling arguments suggest that the occurrences of such resonances are general consequences of degenerate Fermi systems being perturbed by sudden, local, quantum perturbations and their width is a new, emergent, low-energy scale $k_B T_K$ where T_K is usually referred as the 'Kondo' temperature (Cox and Zawadowski, 1999). From the point of view of our present concern, the importance of these results are twofold. First, this low-energy scale, which governs the behaviour of low-temperature fluctuations, has no counterpart in the static mean field theory. Second, $k_B T_K$ varies dramatically from material to material from 1 to 1000 K. Thus, there is need for a sophisticated first-principles theory which can make quantitative material specific predictions of $k_B T_K$. Clearly, if $T_K \ll T_c$ for some particular order, the high-temperature phase is well described by the ensemble of static fluctuations depicted in the 'alloy analogy' calculation. On the other hand, if $T_K \gg T_c$, the static calculations miss out important aspects of the physics. To highlight the burden of this remark, we note that the Curie temperatures of ferromagnets and the critical temperatures of the conventional superconductors can be calculated fairly reliably for the majority of materials. Evidently, the challenge here is to do the same for $k_B T_K$.

9. CONCLUSIONS

This chapter has given an *ab initio* justification for the dual, localized and band-like, character of the 4f-states in the lanthanides. The SIC-LSD provided the first-principles band theory scheme allowing for this differentiation between band-like, where the gain in band formation energy dominates, and localized 4f electrons, where the gain in localization energy dominates. From this, the notion of nominal valence was developed defining the number of remaining band-like states as the valence of the lanthanide ion. These band-like states determine the bonding properties. This definition of valence turned out to be extremely useful and in Section 4, we gave numerous examples how this notion of valence contributed to a better understanding of the physical properties of the lanthanides and their compounds. In particular, the bonding properties of the lanthanides, such as the lattice constants, and their pressure behaviour could be studied without using adjustable parameters. Local magnetic moments and spectroscopic investigations provided a study of some of the properties of the localized f-states. Specifically, we found the degree of 4f localization to be similar in the light and heavy lanthanides. The one-electron SIC-LSD is shown to be an *ab initio* computational scheme consistent with all three Hund's rules.

A finite temperature generalization based on the LSIC-LSD method led to the first-principles study of the phase diagrams of the lanthanides. The study of a magnetic phase diagram for the heavy lanthanides led to the discovery of the role played by the lanthanide contraction in determining the magnetic structure of heavy lanthanides. Also, the importance of the Fermi surface webbing features in driving the magnetic order was explained. Calculating the phase diagram of the α–γ phase transition in elemental Ce allowed us to identify the entropy as the driving force in this transition. These finite temperature studies incorporated thermal fluctuations only. Finally, an outline was given on how to include dynamical, quantum, fluctuations in the present methodology.

REFERENCES

Aerts, C.M., Strange, P., Horne, M., Temmerman, W.M., Szotek, Z., Svane, A. Phys. Rev. B 2004, **69,** 045115.

Ahuja, R., Auluck, S., Johansson, B., Brooks, M.S.S. Phys. Rev. B 1994, **50**(8), 5147–5154.

Alameda, J.M., Givord, D., Lemaire, R., Lu, Q., Palmer, S.B., Tasset, F. J. Phys. 1982, **43,** 133.

Amadon, B., Biermann, S., Georges, A., Aryasetiawan, F. Phys. Rev. Lett. 2006, **96,** 066402.

Anderson, P.W. Phys. Rev. Lett. 1967, **18,** 1049.

Andersen, O.K. Phys. Rev. B 1975, **12,** 3060.

Andersen, O.K., Jepsen, O., Glötzel, D. in: Bassani, F., Fumi, F., Tosi, M.P., editors. Highlights of Condensed Matter Theory, International School of Physics Enrico Fermi, Course 89, Amsterdam: North Holland; 1989, p. 59.

Anderson, P.W., Yuval, G., Haman, D.R. Phys. Rev. B 1970, **1,** 4464.

Andrianov, A.V. J. Magn. Magn. Mater. 1995, **140–144,** 749.

Andrianov, A.V., Chistiakov, O.D. Phys. Rev. B 1997, **55,** 14107.

Andrianov, A.V., Kosarev, D.I., Beskrovnyi, A.I. Phys. Rev. B 2000, **62,** 13844.

Anisimov, V.I., Gunnarsson, O. Phys. Rev. B 1991, **43,** 7570.

Anisimov, V.I., Aryasetiawan, F., Lichtenstein, A.I. J. Phys.: Condens. Matter 1997, **9,** 767.

Anisimov, V.I., Zaanen, J., Andersen, O.K. Phys. Rev. B 1991, **44,** 943.

Anisimov, V.I., Solovyev, I.V., Korotin, M.A., Czyzyk, M.T., Sawatzky, G.A. Phys. Rev. B 1993, **48,** 16929.

Antonov, V.N., Yaresko, A.N., Perlov, A.Y., Thalmeier, A., Fulde, P., Oppeneer, P.M., Eschrig, H. Phys. Rev. B 1998, **58,** 9752–9762.

Arola, E., Strange, P. Appl. Phys. A 2001, **73,** 667.

Arola, E., Strange, P., Gyorffy, B.L. Phys. Rev. B 1997, **55,** 472.

Arola, E., Horne, M., Strange, P., Winter, H., Szotek, Z., Temmerman, W.M. Phys. Rev. B 2004, **70,** 235127.

Aryasetiawan, F., Gunnarsson, O. Phys. Rev. B 1994, **49,** 16214.

Aryasetiawan, F., Gunnarsson, O. Rep. Prog. Phys. 1998, **61,** 237.

Banister, J.R., Legvold, S., Spedding, F.H. Phys. Rev. 1954, **94,** 1140.

Becke, A.D. J. Chem. Phys. 1993, **98,** 5648.

Beiden, S.V., Temmerman, W.M., Szotek, Z., Gehring, G.A. Phys. Rev. Lett. 1997, **79,** 3970.

Benedict, U., Holzapfel, W.B. in: Gschneidner, K.A., Eyring, L., Lander, G.H., Choppin, G.R., editors. Handbook on the Physics and Chemistry of Rare Earths. vol. 17, Amsterdam: North-Holland; 1993, chap. 113.

Bianconi, A., Kotani, A., Okada, K., Giorgi, R., Gargano, A., Marcelli, A., Miyahara, K. Phys. Rev. B 1988, **38,** 3433.

Bihan, T.L., Darracq, S., Heathman, S., Benedict, U., Mattenberger, K., Vogt, O. J. Alloys Compd. 1995, **226,** 143.

Blanter, Y.M., Kaganov, M.I., Pantsulaya, A.V., Varlamov, A.A. Phys. Rep. 1994, **245,** 159.

Blume, M. J. Appl. Phys. 1985, **57,** 3615.

Blume, M., Gibbs, D. Phys. Rev. B 1988, **37,** 1779.

Blundell, S. 2001. Magnetism in Condensed Matter, Oxford: Oxford University Press.

Bonville, P., Hammann, J., Hodges, J.A., Imbert, P., Jéhanno, G.J. Phys. Rev. Lett. 1986, **57,** 2733.

Boothroyd, A.T., Gardiner, C.H., Lister, S.J.S., Santini, P., Noailles, B.D.R.L.D., Currie, D.B., Eccleston, R.S., Bewleya, R.I. Phys. Rev. Lett. 2001, **86,** 2082.

Bouhemadou, A., Khenata, R., Sahnoun, M., Baltache, H., Kharoubi, M. Physica B 2005, **363,** 255.

Brown, S.D., Strange, P., Bouchenoire, L., Zarychta, B., Thompson, P., Mannix, D., Stockton, S., Horne, M., Arola, E., Ebert, H., Szotek, Z., Temmerman, W.M., Fort, D. Phys. Rev. Lett 2007, **99,** 247401.

Butorin, S.M., Duda, L.-C., Guo, J.-H., Wassdahl, N., Nordgren, J., Nakazawa, M., Kotani, A. J. Phys.: Condens. Matter. 1997, **9,** 8155.

Campagna, M., Bucher, E., Wertheim, G.K., Buchanan, D.N.E., Longinotti, L.D. Phys. Rev. Lett. 1974a, **32,** 885.

Campagna, M., Bucher, E., Wertheim, G.K., Longinotti, L.D. Phys. Rev. Lett. 1974b, **33,** 165.

Campagna, M., Wertheim, G.K., Baer, Y. in: Ley, L., Cardona, M., editors. Photoemission in Solids. vol. II. Berlin: Springer; 1979, chap. 4.

Ceperley, D.M., Alder, B.J. Phys. Rev. Lett. 1980, **45,** 566–569.

Chainani, A., Kumigashira, H., Ito, T., Sato, T., Takahashi, T., Yokoya, T., Higuchi, T., Takeuchi, T., Shin, S., Sato, N.K. Phys. Rev. B 2002, **65,** 155201.

Chantis, A.N., van Schilfgaarde, M., Kotani, T. Phys. Rev. B 2007, **76,** 165126.

Cho, E.-J., Chung, J.-S., Oh, S.-J., Suga, S., Taniguchi, M., Kakizaki, A., Fujimori, A., Kato, H., Miyahara, T., Suzuki, T., Kasuya, T. Phys. Rev. B 1993, **47,** 3933.

Cowan, R.D. Phys. Rev. 1967, **163,** 54.

Cox, D.I., Zawadowski, A. Exotic Kondo Effects in Metals, London: Taylor and Francis; 1999.

Cracknell, A.P., Wong, K.C. The Fermi Surface, Oxford: Clarendon; 1973.

Crisan, V., Entel, P., Ebert, H., Akai, H., Johnson, D.D., Staunton, J.B. Phys. Rev. B 2002, **66**(1), 014416.

Croft, M., Jayaraman, A. Solid State Commun. 1980, **35,** 203.

Crowe, S.J., Dugdale, S.B., Major, Z., Alam, M.A., Duffy, J.A., Palmer, S.B. Europhys. Lett. 2004, **65,** 235.

Debray, D., Werner, A., Decker, D.L., Loewenhaupt, M., Holland-Moritz, E. Phys. Rev. B 1982, **25,** 3841.

Degiorgi, L., Bacsa, W., Wachter, P. Phys. Rev. B 1990, **42,** 530.

Degiorgi, L., Teraoka, S., Compagnini, G., Wachter, P. Phys. Rev. B 1993, **47,** 5715.

Delin, A., Fast, L., Johansson, B., Wills, J.M., Eriksson, O. Phys. Rev. Lett. 1997, **79**(23), 4637–4640.

Delin, A., Fast, L., Johansson, B., Eriksson, O., Wills, J.M. Phys. Rev. B 1998, **58,** 4345–4351.

Dimmock, J.O., Freeman, A.J. Phys. Rev. Lett. 1964, **13**(25), 750–752.

Diviš, M., Rusz, J. J. Magn. Magn. Mater. 2005, **290–291,** 1015.

Döbrich, K.M., Bihlmayer, G., Starke, K., Prieto, J.E., Rossnagel, K., Koh, H., Rotenberg, E., Blügel, S., Kaindl, G. Phys. Rev. B 2007, **76,** 035123.

Dreizler, R.M., Gross, E.K.U. Density Functional Theory, Berlin: Springer-Verlag; 1990.

Duan, C.-G., Sabirianov, R.F., Mei, W.N., Dowben, P.A., Jaswal, S.S., Tsymbal, E.Y. J. Phys.: Condens. Matter 2007, **19,** 315220.

Dugdale, S.B., Fretwell, H.M., Alam, M.A., Kontrym-Sznajd, G., West, R.N., Badrzadeh, S. Phys. Rev. Lett. 1997, **79**(5), 941–944.

Duthie, J.C., Pettifor, D.G. Phys. Rev. Lett. 1977, **38**(10), 564–567.

Eriksson, O., Brooks, M.S.S., Johansson, B. J. Less Common. Met. 1990a, **158,** 207.

Eriksson, O., Brooks, M.S.S., Johansson, B. Phys. Rev. B. 1990b, **41,** 7311–7314.

Eriksson, O., Brooks, M.S.S., Johansson, B., Albers, R.C., Boring, A.M. J. Appl. Phys. 1991, **69,** 5897–5902.

Eriksson, O., Ahuja, R., Ormeci, A., Trygg, J., Hjortstam, O., Söderlind, P., Johansson, B., Wills, J.M. Phys. Rev. B 1995, **52,** 4420.

Eschrig, H., Sargolzaei, M., Koepernik, K., Richter, M. Europhys. Lett. 2005, **72,** 611–617.

Eyring, L. in: Gschneidner Jr., K.A., Eyring, L., editors. Handbook on the Physics and Chemistry of Rare Earths. vol. 3. Amsterdam: North-Holland; 1978, chap. 9.

Faulkner, J.S. Prog. Mater. Sci 1982, **27,** 1.

Faulkner, J.S., Stocks, G.M. Phys. Rev. B 1981, **23,** R5628.

Feynman, R.P. Phys. Rev. 1955, **97,** 660.

Filip, A.T., LeClair, P., Smitts, C.J.P., Kohlhepp, J.T., Swagten, J.M., Koopmans, B., de Jonge, W.J.M. Appl. Phys. Lett. 2002, **81,** 1815.

Freeman, A.J., Min, B.I., Norman, M.R. in: Eyring Jr., K.A.L., Hüfner, S., editors. Handbook on the Physics and Chemistry of Rare Earths. vol. 10, pp. 165–229. Amsterdam Elsevier; 1987.

Fretwell, H.M., Dugdale, S.B., Alam, M.A., Hedley, D.C.R., Rodriguez-Gonzalez, A., Palmer, S.B. Phys. Rev. Lett. 1999, **82**(19), 3867–3870.

Fujimori, A. Phys. Rev. B 1983, **28,** 4489.

Gardiner, C.H., Boothroyd, A.T., Pattison, P., McKelvy, M.J., McIntyre, G.J., Lister, S.J.S. Phys. Rev. B 2004, **70,** 024415.

Gasiorowicz, S. Quantum Physics, New York: John Wiley and Sons; 1974.

Georges, A., Kotliar, G., Krauth, W., Rozenberg, M.J. Rev. Mod. Phys. 1996, **68,** 13.

Gerward, L., Olsen, J.S., Petit, L., Vaitheeswaran, G., Kanchana, V., Svane, A. J. Alloys Compd. 2005, **400,** 56.

Ghosh, D.B., De, M., De, S.K. Phys. Rev. B 2003, **67,** 035118.

Godby, R.W., Schlüter, M., Sham, L.J. Phys. Rev. B 1988, **37,** 10159.

Gotsis, H.J., Mazin, I.I. Phys. Rev. B 2003, **68,** 224427.

Gschneidner Jr., K.A. J. Less-Common Met. 1969, **17,** 13.

Gschneidner Jr., K.A. J. Less-Common. Met. 1971, **25,** 405.

Gschneidner Jr., K.A. J. Alloys Compds. 1993, **192,** 1.

Gyorffy, B.L., Stott, M.J. in: Fabian, D.J., Watson, L.M., editors. Band Structure Spectroscopy of Metals and Alloys, New York: Academic Press; 1973.

Gyorffy, B.L., Stocks, G.M. in: Phariseau, P., Gyorffy, B.L., Scheire, L., editors. Electrons in Disordered Metals and at Metallic Surfaces, vol. 42 of NATO 'ASI Series Physics B', NewYork: Plenum Press; 1978.

Gyorffy, B.L., Pindor, A.J., Staunton, J., Stocks, G.M., Winter, H. J. Phys. F-Met. Phys. 1985, **15**(6), 1337–1386.

Gyorffy, B.L., Johnson, D.D., Pinski, F.J., Nicholson, D.M., Stocks, G.M. in: Stocks, G.M., Gonis, A., editors. Alloy Phase Stability, pp. 421–468. Dordrecht, Kluwer Academic Publisher; 1989.

Hanyu, T., Ishii, H., Yanagihara, M., Kamada, T., Miyahara, T., Kato, H., Naito, K., Suzuki, S., Ishii, T. Solid State Commun. 1985, **56,** 381.

Harmon, B.N., Antropov, V.P., Lichtenstein, A.I., Solovyev, I.V., Anisimov, V.I. J. Phys. Chem. Solids 1995, **56,** 1521–1524.

Hassan, A.K., Levy, L.P., Darie, C., Strobel, P. Phys. Rev. B 2003, **67,** 214432.

Haule, K., Oudovenko, V., Savrasov, S.Y., Kotliar, G. Phys. Rev. Lett. 2005, **94,** 036401.

Havinga, E.E., Buschow, K.H.J., van Daal, H.J. Solid State Commun. 1973, **13,** 621.

Hedin, L. Phys. Rev. A 1965, **139,** 796.

Heinemann, M., Temmerman, W.M. Phys. Rev. B 1994, **49**(6), 4348–4351.

Held, K. Adv. Phys. 2007, **56,** 829.

Held, K., McMahan, A.K., Scalettar, R.T. Phys. Rev. Lett. 2001, **87,** 276404.

Hettler, M.H., Tahvildar-Zadeh, A.N., Jarrell, M., Pruschke, T., Krishnamurthy, H.R. Phys. Rev. B 1998, **58,** 7475.

Hill, J.P., McMorrow, D.F. Acta Crystallogr. A 1996, **52,** 236.

Hirosaki, N., Ogata, S., Kocer, C. J. Alloys Compd. 2003, **351,** 31.

Hoekstra, H.R., Gingerich, K.A. Science 1964, **146,** 1163.

Hohenberg, P., Kohn, W. Phys. Rev. 1964, **136,** B864–B871.

Holland-Moritz, N. Z. Phys. B: Condens. Matter 1992, **89,** 285.

Horne, M., Strange, P., Temmerman, W.M., Szotek, Z., Svane, A., Winter, H. J. Phys.: Condens. Matter 2004, **16,** 5061.

Hubbard, J. Proc. R. Soc. London, Ser. A 1963, **276,** 238.

Hubbard, J. Proc. R. Soc. London, Ser. A 1964a, **277,** 237.

Hubbard, J. Proc. R. Soc. London, Ser. A 1964b, **281,** 401.

Hughes, I.D., Däne, M., Ernst, A., Hergert, W., Lüders, M., Poulter, J., Staunton, J.B., Svane, A., Szotek, Z., Temmerman, W.M. Nature 2007, **446**(7136), 650–653.

Hulliger, F. in: Gschneidner Jr., K.A., Eyring, L., editors. Handbook on the Physics and Chemistry of Rare Earths. vol. 4. Amsterdam: North-Holland; 1979, chap. 33.

Hybertsen, M.S., Louie, S.G. Phys. Rev. B 1986, **34,** 5390.

Iandelli, A., Franceschi, E. J. Less-Common. Met. 1973, **30,** 211.

Iandelli, A., Olcese, G.L., Palenzona, A. J. Less-Common. Met. 1980, **76,** 317.

Ito, T., Chainani, A., Takahashi, H.K.T., Sato, N.K. Phys. Rev. B 2002, **65,** 155202.

Jackson, C. Phys. Rev. 1969, **178,** 949.

Jayaraman, A. in: Gschneidner Jr., K.A., Eyring, L., editors. Handbook on the Physics and Chemistry of Rare Earths. vol. 1. Amsterdam: North-Holland; 1978, chap. 9.

Jayaraman, A., Singh, A.K., Chatterjee, A., Devi, S.U. Phys. Rev. B 1974, **9,** 2513.

Jayaraman, A. in: Gschneidner Jr., K.A., Eyring, L., editors. Handbook on the Physics and Chemistry of Rare Earths. vol. 2. Amsterdam: North-Holland; 1979, chap. 20.

Jensen, J., Mackintosh, A.K. Rare Earth Magnetism, Oxford: Clarendon; 1991.

Johansson, B., Rosengren, A. Phys. Rev. B. 1975, **11,** 2836–2857.

Johnson, D.D., Nicholson, D.M., Pinski, F.J., Gyorffy, B.L., Stocks, G.M. Phys. Rev. Lett. 1986, **56**(19), 2088–2091.

Johansson, B., Abrikosov, I.A., Aldén, M., Ruban, A.V., Skriver, H.L. Phys. Rev. Lett. 1995, **74,** 2335.

Jones, R.O., Gunnarsson, O. Rev. Mod. Phys. 1989, **61,** 689.

Joyce, J.J., Andrews, A.B., Arko, A.J., Bartlett, R.J., Blythe, R.I.R., Olson, C.G., Benning, P.J., Canfield, P. C., Poirier, D.M. Phys. Rev. B 1996, **54,** 17515.

Kakehashi, Y. Phys. Rev. B. 2002, **66,** 104428.

Karnatak, R.C., Esteva, J.-M., Dexpert, H., Gasgnier, M., Caro, P.E., Albert, L. Phys. Rev. B 1987, **36,** 1745.

Kasuya, T. Prog. Theor. Phys. 1956, **16**.

Kasuya, T. J. Phys. Soc. Japan 1994, **63,** 843.

Keeton, S.C., Loucks, T.L. Phys. Rev. 1968, **168,** 672.

Kern, S., Loong, C.-K., Faber Jr, J.Jr, Lander, G.H. Solid State Commun. 1984, **49,** 295.

Kittel, C. Introduction to Solid State Physics 6th edition New York: John Wiley and Sons; 1986.

Koelling, D.D., Boring, A.M., Wood, J.H. Solid State Commun. 1983, **47,** 227.

Kohn, W., Rostoker, N. Phys. Rev. 1954, **94,** 1111.

Kohn, W., Sham, L.J. Phys. Rev. 1965, **140,** A1133–A1138.
Korringa, J. Physica 1947, **13,** 392.
Kotliar, G., Savrasov, S.Y., Haule, K., Oudovenko, V.S., Parcollet, O., Marianetti, C.A. Rev. Mod. Phys. 2006, **78,** 865.
Krill, G., Ravet, M.F., Kappler, J.P., Abadli, L., Leger, J.M., Yacoubi, N., Loriers, C. Solid State Commun. 1980, **33,** 351.
Krutzen, B.C.H., Springelkamp, F. J. Phys.: Condens. Matter 1989, **1,** 8369.
Kübler, J. International Series of Monographs on Physics, vol. 106 Oxford University Press; 2000.
Kübler, J., Eyert, V. in: Cahn, R.W., Haasen, P., Kramer, E.J., editors. Materials Science and Technology. vol. 3a, p. 1. New York: Weinheim; 1993.
Kumar, R.S., Cornelius, A.L., Svane, A., Vaitheeswaran, G., Kanchana, V., Bauer, E.D., Hu, M., Nicol, F. Phys. Rev. B. 2008, 78, 075117.
Kurz, P., Bihlmayer, G., Blügel, S. J. Phys. Condens. Matter 2002, **14,** 6353.
Lægsgaard, J., Svane, A. Phys. Rev. B 1998, **58,** 12817.
Lal, H.B., Gaur, K. J. Mater. Sci. 1988, **23,** 919.
Landau, L.D., Lifschitz, E.M. Course of Theoretical Physics, vol. 5, 3rd edition. Oxford: Pergamon; 1980.
Lang, J.K., Baer, Y., Cox, P.A. J. Phys. F 1981, **11,** 121.
Langford, H.D., Temmerman, W.M., Gehring, G.A. J. Phys.: Condens. Matter 1990, **2,** 559.
Larson, P., Lambrecht, W.R.L., Chantis, A.N., van Schilfgaarde, M. Phys. Rev. B 2007, **75,** 045114.
Lebegue, S., Santi, G., Svane, A., Bengone, O., Katsnelson, M.I., Lichtenstein, A.I., Eriksson, O. Phys. Rev. B 2005, **72,** 245102.
Lebegue, S., Svane, A., Katsnelson, M.I., Lichtenstein, A.I., Eriksson, O. Phys. Rev. B 2006a, **74,** 045114.
Lebegue, S., Svane, A., Katsnelson, M.I., Lichtenstein, A.I., Eriksson, O. J. Phys.: Condens. Matter 2006b, **18,** 6329.
LeClair, P., Ha, J.K., Swagten, H.J.M., van de Vin, C.H., Kohlhepp, J.T., de Jonge, W.J.M. J. Appl. Phys. 2002, **80,** 625.
Léger, J.M. Physica B 1993, **190,** 84.
Leger, J.M., Aimonino, P., Loriers, J., Dordor, P., Coqblin, B. Phys. Lett. 1980, **80A,** 325.
Léger, J.M., Epain, R., Loriers, J., Ravot, D., Rossat-Mignod, J Phys. Rev. B 1983, **28,** 7125.
Léger, J.M., Ravot, D., Rossat-Mignod, J. J. Phys. C 1984, **17,** 4935.
Léger, J.M., Oki, K., Rossat-Mignod, J., Vogt, O. J. Phys. 1985, **46,** 889.
Léger, J.M., Redon, A.M. J. Less-Common. Met. 1989, **156,** 137.
Lehner, C., Richter, M., Eschrig, H. Phys. Rev. B 1998, **58,** 6807.
Li, D.X., Oyamada, A., Hashi, K., Haga, Y., Matsumara, T., Shida, H., Suzuki, T., Kasuya, T., Dönni, A., Hulliger, F. J. Magn. Magn. Mater 1995, **140–144,** 1169.
Lichtenstein, A.I., Anisimov, V.I., Zaanen, J. Phys. Rev. B 1995, **52,** R5467–5470.
Lichtenstein, A.I., Katsnelson, M.I. Phys. Rev. B 1998, **57,** 6884.
Lifshitz, I.M. Sov. Phys. JETP 1960, **11,** 1130.
Lindgren, I. Int. J. Quantum Chem. 1971, **5,** 411.
Ling, M.F., Staunton, J.B., Johnson, D.D. Europhys. Lett. 1994, **25**(8), 631–636.
Lloyd, P., Best, P.R. J. Phys. C-Solid State Phys. 1975, **8,** 3752.
Loschen, C., Carrasco, J., Neyman, K.M., Illas, F. Phys. Rev. B 2007, **75,** 035115.
Lovesey, S.W., Collins, S.P. X-ray Scattering and Absorption by Magnetic Materials, Oxford: Clarendon; 1996.
Lüders, M., Ernst, A., Däne, M., Szotek, Z., Svane, A., Ködderitzsch, D., Hergert, W., Györffy, B.L., Temmerman, W. Phys. Rev. B 2005, **71**(20), 205109.
Mahan, G.D. Many-Particle Physics, New York: Plenum Press; 1990.
Marabelli, F., Wachter, P. Phys. Rev. B 1987, **36,** 1238.
Martin, R.M. Electronic Structure: Basic Theory and Practical Methods, Cambridge: Cambridge Universtiy Press 2004.
Mattocks, P.G., Young, R.C. J. Phys. F 1977, **7,** 1219.
McMahan, A.K., Held, K., Scalettar, R.T. Phys. Rev. B 2003, **67,** 075108.
Mermin, N.D. Phys. Rev. 1965, **137,** A1441.
Messiah, A. Quantum Mechanics, Amsterdam North Holland; 1965.
Milstein, F., Robinson, L.B. Phys. Rev. 1967, **159,** 466.

Mirone, A. Eur. J. Phys. B: Condens. Matter Complex Syst. 2005, **47,** 509.
Moewes, A., Ederer, D.L., Grush, M.M., Callcott, T.A. Phys. Rev. B 1999, **59,** 5452.
Mohn, P., Persson, C., Blaha, P., Schwarz, K., Novak, P., Eschrig, H. Phys. Rev. Lett. 2001, **87,** 196401.
Moodera, J.S., Meservey, R., Hao, X. Phys. Rev. Lett. 1993, **70,** 853.
Mori, N., Okayama, Y., Takahashi, H., Haga, Y., Suzuki, T. Physica B 1993, **186–188,** 444.
Moriya, T. Solid State Sciences, vol. 29, Springer Series Berlin and New York: Springer; 1981.
Nicholson, D.M.C., Stocks, G.M., Wang, Y., Szotek, Z., Temmerman, W.M. Phys. Rev. B 1994, **50,** 14686.
Nordström, L., Mavromaras, A. Europhys. Lett. 2000, **49,** 775.
Nozieres, P., DeDominicis, C. Phys. Rev. 1969, **178,** 1097.
Ogasawara, H., Kotani, A., Okada, K., Thole, B.T. Phys. Rev. B 1991, **43,** 854.
Oh, S.-J., Allen, J.W. Phys. Rev. B 1984, **29,** 589.
Ono, S., Hui, F.L., Despault, J.G., Calvert, L.D., Taylor, J.B. J. Less-Common. Met. 1971, **25,** 287.
Oppeneer, P.M., Antonov, V.N., Yaresko, A.N., Perlov, A.Y., Eschrig, H. Phys. Rev. Lett. 1997, **78,** 4079.
Ott, H.R., Rudigier, H., Hulliger, F. Solid State Commun. 1985, **55,** 113.
Oyamada, A., Hashi, K., Maegawa, S., Goto, T., Li, D.X., Suzuki, T., Dönni, A., Hulliger, F. Physica B 1994, **199 & 200,** 42.
Pederson, M.R., Heaton, R.A., Lin, C.C. J. Chem. Phys. 1984, **80,** 1972.
Pederson, M.R., Heaton, R.A., Lin, C.C. J. Chem. Phys. 1985, **82,** 2688.
Perdew, J.P., Zunger, A. Phys. Rev. B 1981, **23,** 5048.
Perdew, J.P., Wang, Y. Phys. Rev. B 1992, **45,** 13244–13249.
Petit, L., Svane, A., Szotek, Z., Temmerman, W.M. Phys. Rev. B 2005, **72,** 205118.
Petit, L., Svane, A., Szotek, Z., Temmerman, W.M. in: Fanciulli, M., Scarel, G., editors. Topics in Applied Physics, vol. 106, p. 331. Berlin Heidelberg: Springer-Verlag; 2007.
Petukhov, A.G., Mazin, I.I., Chioncel, L., Lichtenstein, A.I. Phys. Rev. B 2003, **67,** 153106.
Pickett, W.E., Koelling, D.D., Freeman, A.J. Phys. Rev. B 1981, **23,** 1266.
Pollak, R.A., Holtzberg, F., Freeouf, J.L., Eastman, D.E. Phys. Rev. Lett. 1974, **33,** 820.
Prokofiev, A.V., Shelyakh, A.I., Melekh, B.T. J. Alloys Compd. 1996, **242,** 41.
Razee, S.S.A., Staunton, J.B., Szunyogh, L., Gyorffy, B.L. Phys. Rev. Lett. 2002, **88**(14), 147201.
Rhyne, J.J., McGuire, T. IEEE Trans. Magn. 1972, **MAG-8,** 105.
Richter, M., Eschrig, H. Solid State Commun. 1989, **72,** 263.
Rinke, P., Scheffler, M., Qteish, A., Winkelnkemper, M., Bimberg, D., Neugebauer, J. Appl. Phys. Lett. 2006, **89,** 161919.
Robinson, R.A., Purwanto, A., Kohgi, M., Canfield, P.C., Kamiyami, T., Ishigaki, T., Lynn, J.W., Erwin, R., Peterson, E., Movshovich, R. Phys. Rev. B 1994, **50,** 9595.
Ruderman, M.A., Kittel, C. Phys. Rev. 1954, **96,** 99.
Sakai, O., Shimuzi, Y., Kaneta, Y. J. Phys. Soc. Jpn. 2005, **74,** 2517.
Sakai, O., Shimuzi, Y. J. Phys. Soc. Jpn. 2007, **76,** 044707.
Sakon, T., Sato, N., Oyamada, A., Takeda, N., Suzuki, T., Komatsubara, T. J. Phys. Soc. Jpn. 1992, **61,** 2209.
Sandratsakii, L.M., Kübler, J. Europhys. Lett 1993, **23,** 661.
Scarel, G., Svane, A., Fanciulli, M. in: Fanciulli, M., Scarel, G., editors. Topics in Applied Physics, vol. 106, p. 1. Berlin Heidelberg: Springer-Verlag; 2007.
Schirber, J.E., Schmidt, F.A., Harmon, B.N., Koelling, D.D. Phys. Rev. Lett. 1976, **36**(8), 448–450.
Schüßler-Langeheine, C., Weschke, E., Mazumdar, C., Meier, R., Grigoriev, A.Y., Kaindl, G., Sutter, C., Abernathy, D., Grübel, G., Richter, M. Phys. Rev. Lett. 2000, **84**(24), 5624–5627.
Shirotani, I., Hayashi, J., Yamanashi, K., Hirano, K., Adachi, T., Ishimatsu, N., Shimomura, O., Kikegawa, T. Physica B 2003, **334,** 167.
Sidorov, V.A., Stepanov, N.N., Khvostantsev, L.G., Tsiok, O.B., Golubkov, A.V., Oskotski, V.S., Smirnov, I.A. Semicond. Sci. Technol. 1989, **4,** 286.
Silva, J.L.F.D., Ganduglia-Pirovano, M.V., Sauer, J., Bayer, V., Kresse, G. Phys. Rev. B 2007, **75,** 045121.
Singh, D.J. Phys. Rev. B 1991, **44**(14), 7451–7454.
Sinha, S.K. in: Gschneidner Jr., K.A., Eyring, L., editors. Handbook on the Physics and Chemistry of Rare Earths. vol. 1. Amsterdam, New York, Oxford: North-Holland; 1978, chap. 7.
Skorodumova, N.V., Ahuja, R., Simak, S.I., Abrikosov, I.A., Johansson, B., Lundqvist, B.I. Phys. Rev. B 2001, **64,** 115108.

Skriver, H.L. Solid-State Sciences, vol. 41, Springer Series Berlin: Springer; 1983a.

Skriver, H.L. in: Sinha, S.P., editor. Systematics and Properties of the Lanthanides, p. 213. Dordrecht: Reidel; 1983b.

Slater, J.C. Phys. Rev. 1951, **81,** 385.

Sondhelm, S.A., Young, R.C. J. Phys. F 1977, **15,** L261.

Soven, P. Phys. Rev. 1967, **156,** 809.

Staunton, J.B. Rep. Prog. Phys. 1994, **57,** 1289.

Staunton, J.B., Gyorffy, B.L. Phys. Rev. Lett. 1992, **69,** 371.

Staunton, J., Gyorffy, B.L., Pindor, A.J., Stocks, G.M., Winter, H. J. Phys. F-Met. Phys. 1985, **15**(6), 1387–1404.

Staunton, J., Gyorffy, B.L., Stocks, G.M., Wadsworth, J. J. Phys. F-Met. Phys. 1986, **16**(11), 1761–1788.

Staunton, J.B., Ling, M.F., Johnson, D.D. J. Phys.-Condens. Matter 1997, **9**(6), 1281–1300.

Staunton, J.B., Ostanin, S., Razee, S.S.A., Gyorffy, B.L., Szunyogh, L., Ginatempo, B., Bruno, E. Phys. Rev. Lett. 2004, **93**(25), 257204.

Staunton, J.B., Szunyogh, L., Buruzs, A., Gyorffy, B.L., Ostanin, S., Udvardi, L. Phys. Rev. B 2006, **74**(14), 144411.

Sticht, J., Kübler, J. Solid State Commun. 1985, **53,** 529.

Stocks, G.M., Winter, H. Zeitschrift für Physik B-Condens. Matter 1982, **46**(2), 95–98.

Stocks, G.M., Winter, H. in: Phariseau, P., Temmerman, W.M., editors. The Electronic Structure of Complex Systems. Vol. NATO ASI Series Physics B113, New York: Plenum Press; 1984.

Stocks, G.M., Temmerman, W.M., Gyorffy, B.L. Phys. Rev. Lett. 1978, **41**(5), 339–343.

Strange, P. Relativistic Quantum Physics, Cambridge: Cambridge University Press; 1998.

Strange, P., Staunton, J., Gyorffy, B.L. J. Phys. C-Solid State Phys. 1984, **17**(19), 3355–3371.

Strange, P., Svane, A., Temmerman, W.M., Szotek, Z., Winter, H. Nature 1999, **399,** 756–758.

Svane, A. Phys. Rev. B 1995, **51**(12), 7924–7926.

Svane, A. Phys. Rev. B 1996, **53,** 4275.

Svane, A., Szotek, Z., Temmerman, W.M., Winter, H. Solid State Commun. 1996, **102,** 473.

Svane, A., Trygg, J., Johansson, B., Eriksson, O. Phys. Rev. B 1997, **56,** 7143–7148.

Svane, A., Szotek, Z., Temmerman, W.M., Lægsgaard, J., Winter, H. J. Phys.: Condens. Matter 1998, **10,** 5309.

Svane, A., Temmerman, W.M., Szotek, Z. Phys. Rev. B 1999, **59,** 7888.

Svane, A., Temmerman, W.M., Szotek, Z., Petit, L., Strange, P., Winter, H. Phys. Rev. B 2000, **62,** 13394.

Svane, A., Strange, P., Temmerman, W.M., Szotek, Z., Winter, H., Petit, L. Phys. Stat. Sol. (b) 2001, **223,** 105.

Svane, A., Santi, G., Szotek, Z., Temmerman, W.M., Strange, P., Horne, M., Vaitheeswaran, G., Kanchana, V., Petit, L. Phys. Stat. Sol. (b) 2004, **241,** 3185.

Svane, A., Kanchana, V., Vaitheeswaran, G., Santi, G., Temmerman, W.M., Szotek, Z., Strange, P., Petit, L. Phys. Rev. B 2005, **71,** 045119.

Syassen, K. Physica B 1986, **139,** 277.

Szotek, Z., Gyorffy, B.L., Stocks, G.M., Temmerman, W.M. J. Phys. F-Met. Phys. 1984, **14**(11), 2571–2599.

Takeda, N., Tanaka, K., Kagawa, M., Oyamada, A., Sato, N., Sakatsumi, S., Aoki, H., Suzuki, T., Komatsubara, T. J. Phys. Soc. Jpn. 1993, **62,** 2098.

Tanaka, S., Ogasawara, H., Okada, K., Kotani, A. J. Phys. Soc. Jpn. 1995, **64,** 2225.

Taylor, J. Scattering Theory, New York: Wiley; 1972.

Taylor, K.N.R., Darby, M.I. Physics of Rare Earth Solids, London: Chapman and Hall; 1972.

Temmerman, W.M., Sterne, P.A. J. Phys.: Condens. Matter 1990, **2,** 5529.

Temmerman, W.M., Szotek, Z., Winter, H. Phys. Rev. B 1993, **47,** 1184–1189.

Temmerman, W.M., Svane, A., Szotek, Z., Winter, H. in: Dobson, J.F., Vignale, G., Das, M.P., editors. Electronic Density Functional Theory: Recent Progress and New Directions, p. 327. New York: Plenum; 1998.

Temmerman, W.M., Szotek, Z., Svane, A., Strange, P., Winter, H., Delin, A., Johansson, B., Eriksson, O., Fast, L., Wills, J.M. Phys. Rev. Lett. 1999, **83,** 3900.

Torumba, D., Vanhoof, V., Rots, M., Cottenier, S. Phys. Rev. B 2006, **74,** 014409.

Trygg, J., Johansson, B., Eriksson, O., Wills, J.M. Phys. Rev. Lett. 1995, **75,** 2871–2874.

Tsiok, O.B., Sidorov, V.A., Bredikhin, V.V., Khvostantsev, L.G., Golubkov, A.V., Smirnov, I.A. Solid State Commun. 1991, **79,** 227.
Turek, I., Kudrnovský, J., Bihlmayer, G., Blügel, S. J. Phys. Condens. Matter 2003, **15,** 2771.
Ufuktepe, Y., Kimura, S., Kinoshita, T., Nath, K.G., Kumigashira, H., Takahashi, T., Matsumura, T., Suzuki, T., Ogasawara, H., Kotani, A. J. Phys. Soc. Jpn. 1998, **67**(6), 2018–2026.
Vaitheeswaran, G., Petit, L., Svane, A., Kanchana, V., Rajagopalan, M. J. Phys.: Condens. Matter 2004, **16,** 4429.
van Schilfgaarde, M., Kotani, T., Faleev, S. Phys. Rev. B 2006a, **74,** 245125.
van Schilfgaarde, M., Kotani, T., Faleev, S. Phys. Rev. Lett. 2006b, **96,** 226402.
Vedel, I., Redon, A.M., Rossat-Mignod, J., Vogt, O., Léger, J.M. J. Phys. C 1986, **19,** 6297.
Vedel, I., Redon, A.M., Rossat-Mignod, J., Vogt, O., Léger, J.M. J. Phys. C 1987, **20,** 3439.
Villars, P., Calvert, L.D. in: Pearson's Handbook of Cystallographic Data for Intermetallic Phases 2nd edition. Ohio: ASM International; 1991.
von Barth, U., Hedin, L. J. Phys. C: Sol. State Phys. 1972, **5,** 1629–1642.
Vosko, S.H., Wilk, L., Nusair, M. Can. J. Phys. 1980, **58,** 1200–1211.
Wachter, P. in: Gschneidner Jr., K.A., Eyring, L., editors. Handbook on the Physics and Chemistry of Rare Earths. vol. 19. Amsterdam, New York, Oxford: North-Holland; 1993, chap. 132.
Wang, B.Y., Gabe, E.J., Calvert, L.D., Taylor, J.B. Acta Crystallogr. B 1977, **33,** 131.
Werner, A., Hochheimer, H.D., Jayaraman, A. Solid State Commun. 1981, **38,** 325.
Werner, A., Hochheimer, H.D., Meng, R.L., Bucher, E. Phys. Lett. 1983, **97A,** 207.
Worledge, D.C., Geballe, T.H. J. Appl. Phys. 2000, **88,** 5277.
Wuilloud, E., Delley, B., Schneider, W.-D., Baer, Y. Phys. Rev. Lett. 1984, **53,** 202.
Wulff, M., Lonzarich, G.G., Fort, D., Skriver, H.L. Europhys. Lett. 1988, **7,** 629.
Wyckoff, R.W.G. CrystalStructures 1968, vol. 1. New York: Interscience; 1968.
Yosida, K. Phys. Rev. 1957, **106,** 893.
Young, R.C., Jordan, R.G., Jones, D.W. Phys. Rev. Lett. 1973, **31,** 1473.
Zimmer, H.G., Takemura, K., Syassen, K., Fischer, K. Phys. Rev. B 1984, **29,** 2350.
Zölfl, M.B., Nekrasov, I.A., Pruschke, T., Anisimov, V.I., Keller, J. Phys. Rev. Lett. 2001, **87,** 276403.
Zunger, A., Perdew, J.P., Oliver, G.L. Sol. State Commun. 1980, **34,** 933.
Zwicknagl, G. Adv. Phys. 1992, **41,** 203–302.